6-25-2014

Novel Pattern Reconfigurable Antenna Arrays Using Engineered Metamaterials and Microfluidic Principles

Ahmad Gheethan
University of South Florida, aagheethan@mail.usf.edu

Novel Pattern Reconfigurable Antenna Arrays Using Engineered Metamaterials and Microfluidic Principles

by

Ahmad A. Gheethan

A dissertation submitted in partial fulfillment
of the requirements for the degree of
Doctor of Philosophy
Department of Electrical Engineering
College of Engineering
University of South Florida

Major Professor: Gokhan Mumcu, Ph.D.
Thomas Weller, Ph.D.
Richard Gitlin, Ph.D.
Rasim Guldiken, Ph.D.
Paul Herzig, B.S.E.E.

Date of Approval:
June 25, 2014

Keywords: Beam Scanning, Feed Networks, GPS, High Gain, MM-Wave

DEDICATION

To my parents: Suad and Adel, my lovely sisters: Maysa'a and Nour, and my brother Mohammad

ACKNOWLEDGMENTS

I would like to thank my advisor Prof. Gokhan Mumcu for his consistent support, guidance, help and patience through my doctoral studies since I have joined the WAMI group at USF. His knowledge and expertise in the areas of electromagnetics, antenna and microwave engineering have aided me to get to this point and provided me with the clear path in my research. I'm grateful to him for improving my skills in many aspects especially in technical writing, programming, and working under a fast pace research environment. It is my pleasure to be his student and I'm honored to be a graduate of his research group.

I'm sincerely thankful to Prof. Thomas Weller, Prof. Richard Gitlin, Prof. Rasim Guldiken and Paul Herzig for their acceptance to join the presentation of my defense and spending their valuable time to read my dissertation. I'm also very grateful to Prof. Weller for having me on the phone in Spring/2010, and passing my resume to Dr. Mumcu. That phone call and his support greatly helped me to join the USF later on.

I want to express my deepest and thankful feelings to Saurabh Gupta and Abhishek Dey for their help in the GPS and microfluidic focal plane array projects. Saurabh showed me how to use the milling machine that I've used to fabricate the GPS array later on. The amazing skills of Abhishek Dey at the clean room provided our group with important solutions for many problems we had in fabricating the microchannels. It will not be an exaggeration to mention that his fabrication technique is a benchmark for our group.

Meeting up with the WAMI student members was a great experience and I'm really glad to have this chance. It was also my pleasure to meet up with the students of the WCSP research group especially Ali Gorcin who became my older brother with his kind advices. I also want to thank my close friends Anas Tom and Amar Amouri for all the good times we had together. Away from Tampa, I want to say thanks to my close friend Mohammad Almalkawi for his friendship and the discussions we had.

I want to thank all of my teachers for their efforts through my elementary and high school years. Many thanks to Abdulla Aljetawi and Adel Ratrout who taught me, respectively, Math and English in very creative and attracting ways. The teachers' effort helped me to join JUST where I obtained my undergrad degree, and had the chance to meet up with Prof. Nihad Dib. A genius person, yet humble, who helped me in many aspects and kept his door always open for me and my classmates. I'm really thankful to him and I can't find the words to express my appreciation toward him. My graduate journey started by joining the group of Prof. Dimitris Anagnostou who supervised me through my master's degree in SDSM&T. His supervision was helpful and supportive, and he provided me with great chances that are not usually offered for students at the master's level. I'm thankful to him and for his guidance.

My family has been supportive and patient through my years of study. I want to thank every member of my family especially my parents, sisters, and brother. I'm also grateful to my family members in Chicago and Tampa who greatly helped me especially in my first days here in the US.

Most importantly, I'm thankful to Allah for his blessing that helped me in my achievements.

TABLE OF CONTENTS

LIST OF TABLES

LIST OF FIGURES

ABSTRACT

This dissertation proposes novel solutions for important drawbacks of antenna arrays. One of the main contributions of the presented work is size reduction and nulling performance improvement of traditionally large anti-jam global positioning system (GPS) arrays using miniature antennas and electrically small resonators emulating an engineered metamaterial. Specifically, a miniaturized coupled double loop (CDL) dual band antenna is first introduced as a small antenna element of the compact GPS array. The loops that are capacitively coupled using lumped element capacitor, and employ metallic pins around their perimeter to improve the radiation efficiency by achieving a volumetric current distribution. This design is employed for the implementation of a compact 2×2 GPS array by reducing the inter-element spacing between the adjacent elements. However, having the antenna elements in close proximity of each other yields to a high mutual coupling and potentially degrades the nulling performance. The mutual coupling is performed by observing the magnetic field distribution within the array. It is noticed that the mutual coupling can be reduced by using metamaterial resonators. The right hand circular polarization (RHCP) radiation nature of the array complicates the mutual coupling suppression as compared to linear arrays. It is determined that split ring resonator (SRRs) are effective to mitigate the mutual coupling problem if placed strategically around the antenna elements. The study is verified experimentally where the mutual coupling is reduced by more than 10 dB. Lowering the mutual coupling improved the array's nulling capability by increasing the nulls' depth by 8 dB as well as enhancing the accuracy of the nulls' locations.

The second major contribution of the presented work is to introduce a novel microfluidic based beam-scanning technique for the implementation of low cost mm-wave antenna arrays. Traditionally, beam scanning capability is obtained using mechanical steering of the entire antenna structure or electronic components such as switches or phase shifters. The former is bulky, whereas the latter technique requires integrating substantial and expensive hardware in the array's feed network. For instance, a beam-scanning 1×8 focal plane array (FPA) would employ 7 single pole double through (SPDT) switches in its feed network. If an 8×8 FPA is desired, then 8×7+8 switches are required that results in an efficient design in terms of power loss and cost. In this dissertation, the microfluidic principles are introduced for designing and implementing affordable beam scanning antenna array with high gain radiation. Specifically, a microfluidic-based focal plane array 1×8 (MFPA) is designed and implemented at 30 GHz. The proposed MFPA consists of microfluidic channels connecting reservoirs. Both of the channels and reservoirs are filled with a low loss dielectric solution, and the antenna is formed by using a small volume of liquid metal. The beam scanning capability is obtained by placing the array at the focal point of a microwave lens and moving the antenna among the reservoirs using a micropump. Therefore, the feed network is extremely simplified by avoiding using SPDT switches. In addition, a strategic design methodology for a completely passive resonant corporate feed network is discussed. The array is characterized numerically and verified experimentally. The simulated and measured performances are in a very good agreement with $\pm 30^0$ FoV and > 21 dB realized gain. However, the array's radiation pattern exhibits high side lobe level (SLL) due to the resonant nature of the introduced corporate feed network. Consequently, new resonant and non-resonant straight feed networks are introduced to alleviate the high SLL issue. Moreover, they are modeled with appropriate equivalent circuits in order to analyze the array's performance analytically in terms of -10 dB $|S_{11}|$ bandwidth

and power loss. The analytical solution is based on the transmission line theory and two ports network analysis. It is verified with the full wave simulations and a very good agreement is observed. Using the straight feed network reduces the SLL to more than 20 dB relative the pattern's peak. This enhancement in the performance is verified experimentally as well by designing, fabricating and testing a 30 GHz MFPA fed using a resonant straight network. A $\pm 25^0$ FoV is obtained with a SLL < -20 dB and 4% -10 dB $|S_{11}|$ bandwidth.

CHAPTER 1: INTRODUCTION

The continuous growth of wireless communication systems is associated with many problems such as limited channel bandwidth, interference and restricted coverage range [1]. The utilization of antenna arrays was suggested to overcome some of the challenges as they can provide many favorable characteristics like directive patterns, beam scanning and nullifying the jamming signals [2]. However, the conventional antenna arrays suffer in terms of physical size, mutual coupling, high cost, and design complexity. For instance, available commercial GPS antenna arrays exhibit large dimensions. Figure 1.1(a) shows the 14.1" diameter array that was introduced by the PMW/A -170's Air Navigation Warfare (NAVWAR) program [3]. The array consists of 7 elements and exhibits the anti-jamming capability. Another example of an available commercial GPS array (DM N79-1-1) is depicted in Figure 1.1(b) [4]. As shown in the figure, the array is comprised of 6 antenna elements that operate at the L_1 (1.575 GHz) and L_2 (1.227 GHz) frequency

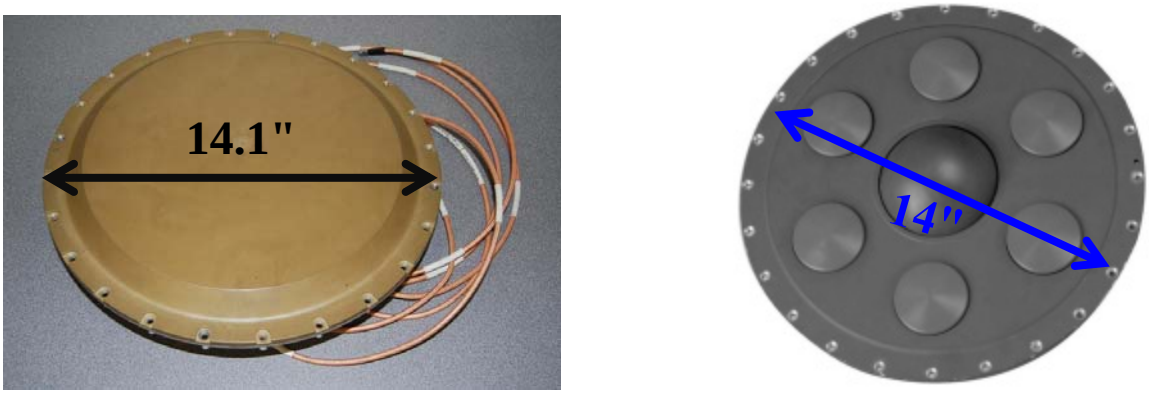

(a) (b)

Figure 1.1: Examples of commercial GPS arrays.

bands. Similar to the aforementioned array, the array is a Controlled Radiation Pattern Antenna (CRPA) that includes a processing unit for cancelling the interference signals and places nulls towards them in the array's radiation pattern. The array exhibits a diameter of 14" and the radial separation between the elements is 4.71". Therefore, it is expected to have low mutual coupling (>10 dB) among the antennas. This anticipation is actually supported by the array's nulling performance that is claimed to have > 20 dB null depth.

Although the previously mentioned arrays provide anti-jamming functionalities, they exhibit large dimensions. Therefore, these designs are not suitable with the current stringent requirements that demand compact arrays [5, 6]. Having antenna elements in close proximity to reduce the size results in higher mutual coupling that becomes a serious problem degrading the array nulling and beam steering functionality [7]. As a result, new design techniques should be investigated to achieve miniature antenna arrays exhibiting low mutual coupling among their elements.

Recently, electromagnetic band gap (EBG) structures [8] and metamaterial insulators based on split ring resonators (SRRs) [9, 10] have been introduced as alternative and effective methods for suppressing the mutual coupling among the antenna elements of compact arrays. Due to their small electrical size, SRRs have been particularly found attractive when the antenna elements of the array were placed in close proximity ($<< \lambda_0/2$). Specifically, stacked SRRs were shown to prevent wave propagation and suppress mutual coupling by emulating an effective medium that can be characterized via a homogenized negative permeability property. Although SRR based coupling reduction has been already investigated, these studies are limited to linearly polarized patch [9] and high profile monopole [10] antennas. Our technique extends the approach to a 2×2 circularly polarized compact GPS array that is constructed from electrically small coupled double

loop (CDL) antennas [11]. Specifically, chapter 2 introduces the design and nulling capability of a compact 2×2 dual-band coupled double loop (CDL) GPS antenna array loaded with broadside coupled split ring resonators (BC-SRR). The high level of L_2 band mutual coupling is reduced by utilizing μ-negative (MNG) BC-SRR metamaterial within the array volume. This metamaterial loading is possible due to the small L_2 band electrical size ($\lambda_0/8.5\times\lambda_0/8.5$) of the CDL antenna elements. Different than the existing work on coupling reduction of linearly polarized antenna arrays, mutual coupling mechanism within the circularly polarized GPS array is considered and MNG metamaterials are shown to reduce the mutual coupling if they are placed between the antennas in a particular alignment. A 2×2 array with $\lambda_0/3.7$ inter-element spacing is designed to be loaded with BC-SRRs and experimentally verified to exhibit a 10 dB L_2 band mutual coupling reduction. Through simulations and experiments, it is also demonstrated that the reduction in L_2 band mutual coupling improves the L_2 band array nulling capability in terms of accuracy and null depth without affecting the already well-behaved L_1 band performance. The presented array has an overall footprint size of 4.3″×4.3″ and can be potentially miniaturized further for different inter-element spacing.

In addition to the need for compact arrays, cost reduction is highly desired for antenna arrays that exhibit high gain and beam scanning capabilities. At the mm-wave band (30 GHz-300 GHz), these functionalities are desired for many applications such as improving the capacity of 60 GHz wireless channels by increasing the signal to noise (S/N) ratio [12]. Moreover, the 77 GHz automotive radar systems will be soon integrated with most of the commercial automobile brands for collision warning and adaptive cruise control applications [13]. In addition, the 94 GHz radar arrays are being utilized for mm-wave imaging, security and military applications [14]. In order to obtain the high gain and beam scanning capabilities, the state of art of phased arrays [15], focal

plane arrays (FPAs) [16], and reflectarrays [17] are used. Phased arrays can be implemented using architectures such as "*All RF*" [18-21], IF phase shifting approach [22], and mixer-based designs [23, 24]. The "*All RF*" designs demand employing extensive hardware components such as phase shifters, power amplifiers and power dividers in their feed networks. Therefore, they are complicated and expensive. On the other hand, the IF phase shifting and mixer-based designs require a phase shifter and mixer per antenna element. Such designs result in challenges in routing the local oscillator's signal to the mixing elements especially for large apertures (i.e., large number of elements).

Similar to "*All RF*" phased arrays, FPAs utilizes RF components for the beam scanning functionality. Specifically, an $M \times N$ FPA requires $M \times (N\text{-}1) + (M\text{-}1)$ SP2T switches integrated with its feed network. At the mm-wave band, these switches suffer from high insertion loss (~ 1 dB at 30 GHz) and high cost that result in very expensive and inefficient arrays in terms of power consumption. To reduce the feed network complexity, in this dissertation, a novel beam scanning FPA that relies on microfluidic principles is investigated. As will be discussed in chapters 3, the antenna elements of the microfluidic-based FPA (MFPA) are formed from microfluidic reservoirs and channels. The reservoirs exhibit the shape of a patch antenna and only one of them is activated when filled with liquid metal. A low loss dielectric solution is utilized to move the liquid metal among the adjacent reservoirs using micropumps. Although liquid metal based RF reconfigurability has been recently proposed for realizing frequency tunable RF components such as antennas [25] and frequency selective surfaces [26], this work extends the use of liquid metals into a fundamentally different beam scanning array technology. Specifically, we demonstrate the operational principles and experimentally verify the technique by considering a 1×8 30 GHz FPA that would traditionally require 7 SP2T RF switches. The MFPA is designed to operate behind an

8 cm diameter extended hemispherical Rexolite lens with an extension length of 4.32 cm [27]. It will be shown that the feed network of the MFPA can be successfully operated without resorting to any RF switches when the microfluidic enabled beam scanning is utilized. The proximity coupled feed network of the array is passive and designed strategically to accommodate the position variation of the liquid metal antenna element. Specifically, the network is a resonant based corporate one that consists of 8 $\lambda_g/2$ open stub resonators separated by λ_g microstrip transmission lines. Using the proposed design, the array operates with measured 7^0 half power beamwidth (HPBW), > 21 dB realized gain, 3.3% |S11 | < -10 dB bandwidth and provides $\pm 30^0$ beam scanning range. The presented microfluidic based beam scanning technique operates without resorting to RF switches. Consequently, it is promising for high power handling and low cost realization of mm-wave high gain beam scanning antenna arrays.

Chapter 4, for the first time, considers the design details and performance evaluation of three different passive network layouts that can potentially be utilized to excite MFPAs. Specifically, resonant corporate, resonant straight, and non-resonant straight microstrip line feed networks are introduced and their loss/bandwidth performances are investigated using transmission line theory. In addition, a ray tracing and diffraction radiation integrals hybrid analysis [28] is utilized to demonstrate the impact of the proposed feed networks on the radiation properties of the MFPA in terms of realized gain and side lobe levels (SLLs). It is shown that the resonant and non-resonant straight microstrip line feed networks reduce the SLL by more than 10 dB relative to the resonant corporate feed network utilized in chapter 3. The performance improvements are experimentally verified through an 8 element extended hemispherical dielectric lens based MFPA prototype. Different than the work that relied on liquid metal, the antenna element of this MFPA is implemented from a metalized plate by carrying out flow

characterizations on various microfluidic channel geometries. This metalized plate approach paves the way for reliable liquid metal free microfluidic reconfigurable devices with possibly higher efficiency and power handling capabilities.

Finally, chapter 5 summarizes the work discussed in this dissertation and discusses the possible future work of the GPS array as well as the MFPAs.

CHAPTER 2: COMPACT 2×2 COUPLED DOUBLE LOOP GPS ANTENNA ARRAY LOADED WITH BROADSIDE COUPLED SPLIT RING RESONATORS

2.1. Introduction

Global Positioning System (GPS) receivers are susceptible to jamming due to the relatively weak signal levels [2]. To alleviate this issue, two dimensional (2D) anti-jam GPS antenna arrays are generally employed to adaptively place radiation pattern nulls towards the directions of undesired interfering signals. In addition to being able to generate deep nulls, the anti-jam GPS arrays are also required to exhibit a compact size for applications involving small unmanned vehicles [6]. Recently, several miniaturized GPS array designs have been introduced by employing tightly packed electrically small antennas [5, 6]. A consequence of placing antenna elements in close proximity is higher mutual coupling that results in a degraded nulling capability of an array [7, 29]. However, to the best of our knowledge, previous studies have not considered any methods for reducing the mutual coupling within compact circularly polarized (CP) GPS arrays, and discussed their effects on the array nulling.

Reducing mutual coupling within linearly polarized antenna arrays have been actively pursued in literature by making use of various techniques. For example, integrating matching networks within printed monopole antennas has been shown to be an effective technique [30, 31]. Slotted ground planes acting as electromagnetic band-gap (EBG) structures have been used to decouple different types of linearly polarized antennas such as patches, monopoles and planar inverted F antennas [32, 33]. Similarly, mushroom like EBG structures have been used to suppress

mutual coupling between patch antennas [8, 34] . For tightly packed monopole and patch antenna arrays, periodic arrangements of spiral resonators (SRs) and broadside coupled split ring resonators (BC-SRRs) have been demonstrated to be effective in reducing mutual coupling as they effectively act as an artificial media with negative permeability (i.e. μ-negative (MNG) metamaterial) within the vicinity of their resonance frequency [10, 35]. These types of resonators have also been proposed to be utilized in compact RF systems such as small radio repeaters [9].

A key aspect of reducing mutual coupling via employing spiral or split-ring resonators relies on aligning the resonators' axes with the magnetic field component of the electromagnetic field responsible for mutual coupling. Since the electromagnetic field distribution around the antenna elements of a tightly packed array is strongly dependent on the antenna type and its excitation, a judicious choice must be made for aligning the resonators. These concepts have been already shown to work effectively in reducing mutual coupling within various types of linearly polarized antenna arrays [10, 35]. However, the coupling mechanism observed within compact GPS arrays is more complicated. This is due to the fact that in CP antennas two orthogonal resonant modes are simultaneously excited and these modes exhibit different coupling field distributions [36]. In addition, for compact GPS arrays, the number of resonators and their physical area must be minimal to maintain the small array size. Another concern is associated with the impedance mismatch issues that may occur by placing the resonators in close proximity of the antenna elements.

This chapter investigates the design and performance of a compact 2×2 GPS array loaded by BC-SRR based μ-negative metamaterial (see Figure 2.1). Different than previous work [8-10, 30-35], a small circularly polarized array is designed with reduced mutual coupling and shown to exhibit improved nulling capability. The design principles are characterized computationally and

validated experimentally. Additionally, the elements of the array are dual-band coupled double loop (CDL) antennas and distinguish it from previously published compact GPS arrays [5, 6, 37]. The work is organized as follows: The impedance matching and gain performances of the stand-alone dual-band CDL GPS antenna element are briefly described in section 2.2. Section 2.3 analyzes the mutual coupling level within the array through the simulated *S*-parameters and determines that L_2 band coupling level is significantly higher (7 dB) than the L_1 band. Hence, the L_2 band magnetic field distribution within the array is subsequently investigated to identify the possible locations for introducing the BC-SRRs to suppress the mutual coupling. Section 2.4 carries out the BC-SRR loaded CDL GPS array design. The number and exact locations of the BC-SRRs are determined through simulations in order to maintain the good impedance matching performance of the antenna elements and the compactness of the array. Section 2.5 investigates the nulling capability of the BC-SRR loaded array through simulations and experiments. Specifically, the mutual coupling within the designed BC-SRR loaded GPS array is shown to be reduced by more than 10 dB in the L_2 band. The presented results also demonstrate that the BC-SRR loaded array potentially exhibits a better nulling capability in terms of accuracy and depth as compared to the unloaded array. Specifically, the nulls are measured to be 8 dB deeper when the array is loaded with BC-SRRs.

2.2. CDL GPS Antenna Element

Figure 2.1(a) depicts the computational model of the 2×2 BC-SRR loaded GPS array consisting of dual-band (L_2: 1.227 GHz, L_1: 1.575 GHz) CDL antenna elements. The CDL antenna uses a readily available Rogers® TMM10i printed circuit board as its substrate (ε_r=10.2, tan(δ)=0.002) and exhibits an overall size of 1.1"×1.1"×0.5" (i.e. $\lambda_0/8.5\times\lambda_0/8.5$ at L_2). This electrically small element size enables construction of a compact GPS array. For the presented

study, the separation between element edges is 1.5". This implies a $\lambda_0/3.7$ center to center separation at L_2 band. The overall array footprint is 4.3"×4.3" and comparable to the recently available 2×2 GPS arrays (e.g. [38]).

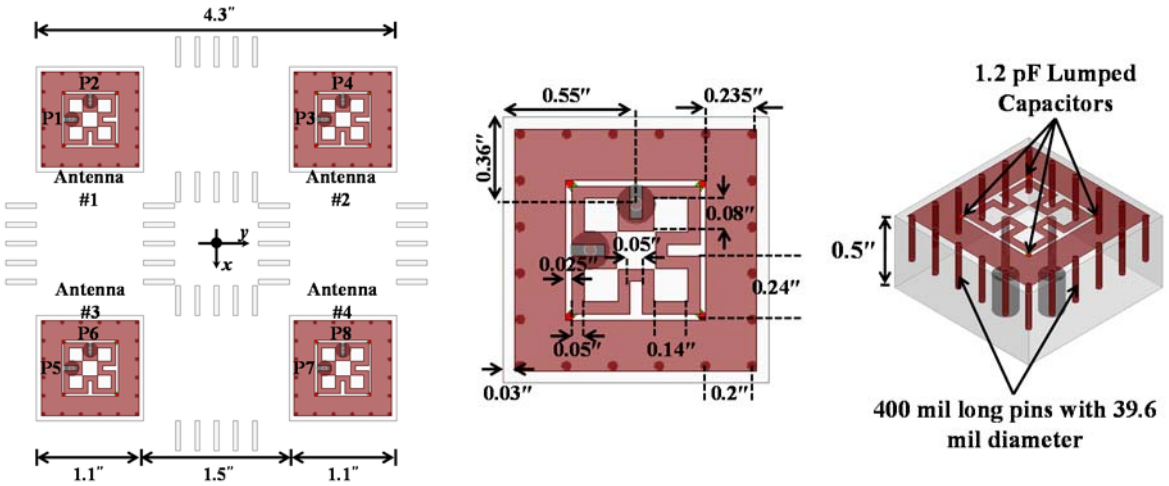

Figure 2.1: HFSS Computational models of the 2D GPS array. a) BC-SRR loaded 2×2 CDL GPS antenna array and CDL GPS antenna: b) top view and c) 3D view.

As shown in Figure 2.1(b), the CDL antenna footprint consists of two printed loops that are capacitively coupled through the lumped coupling capacitors. The 1.2 pF capacitors are primarily utilized for adjusting the frequency spacing between the lower and higher-end resonance frequencies of the CDL GPS antenna [11]. To maintain a compact antenna size without degrading its radiation efficiency, the outer loop is loaded with 400 mil long conductive pins with 39.6 mil diameters as shown in Figure 2.1(c). The antenna is fed by two coaxial probes that are 90^0 out of phase with respect to each other to generate the right hand circularly polarized (RHCP) radiation. Throughout the paper, an infinite ground plane was used in simulation models, whereas a 24"×24" square ground plane was employed to take the measurements. Figure 2.2(a) presents the simulated and measured $|S_{11}|$ performance of the stand-alone antenna element and a good agreement with

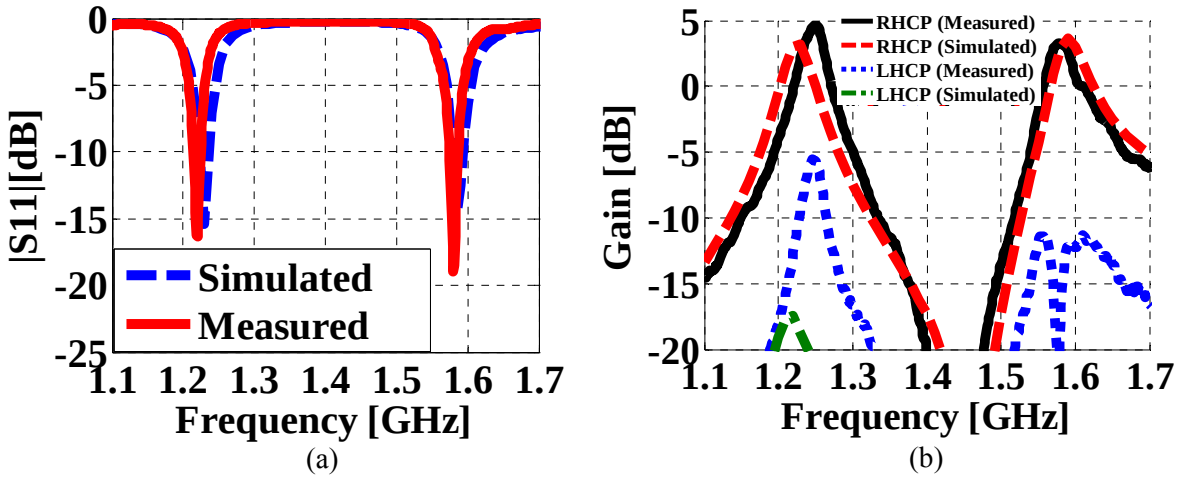

Figure 2.2: Simulated and measured performance of the CDL GPS antenna. a) $|S_{11}|$ and b) Broadside RHCP and LHCP gain.

simulations is observed at both L_2 and L_1 bands. The measured and simulated realized broadside gains are presented in Figure 2.2(b). It is observed that the measured L_2 and L_1 band 3dB realized RHCP gain bandwidths are 26 MHz and 35 MHz, respectively. The measured left hand circularly polarized (LHCP) gain is 10 dB lower than the RHCP gain over the both GPS bands. Further details about the antenna element (such as the design principles and trade-off studies regarding pin dimensions) are beyond the scope of this work [39].

2.3. Mutual Coupling within the 2×2 CDL GPS Array

To characterize the mutual coupling level and associated field distributions, full wave simulations were carried out. Since the coupling among the ports of the diagonally positioned antenna elements (e.g. antenna #1 and #4 in Figure 2.1(a)) were found to be significantly (i.e. 13 dB) lower than that of the adjacent elements; the coupling mechanism between the adjacent elements (i.e. a 2×1 array composed of antenna #1 and #2) was investigated further in detail. This choice allowed avoiding computationally expensive and time consuming simulations when array study was later on generalized to the 2×2 array by employing the 90^0 rotational symmetry of

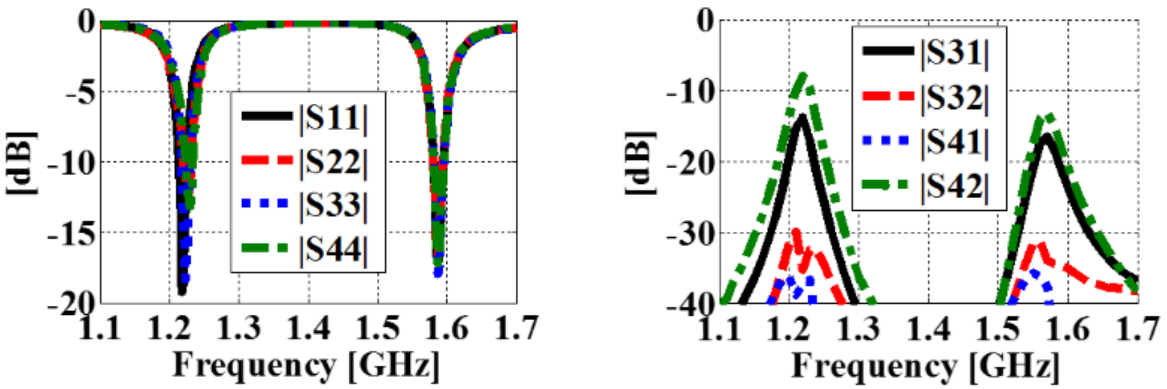

Figure 2.3: Simulated performance of the 2×1 CDL GPS antenna array. The geometrical configuration is identical to the first row of the 2×2 array shown in Fig. 1 without the BC-SRRs: a) Impedance match of antennas # 1 and # 2; b) Mutual coupling among the antenna ports.

the array layout. Simulation and experimental studies performed on the BC-SRR loaded 2×2 array also demonstrated the validity of this design approach. Figure 2.3 depicts the simulated impedance matching and mutual coupling performance of the 2×1 CDL array (modeled from the top row of the 2×2 array) when BC-SRRs are not located between the antennas. All of the antenna ports (see Figure 1(a) for port numbering) within the 2×1 array continue to exhibit a good impedance match ($|S_{ii}|$<-15 dB, i = 1, 2, 3, 4) at the center frequency of both GPS bands. The mutual coupling levels presented in Figure 2.3(b) indicate that coupling between the modes excited by ports 1-3 (i.e. $|S_{31}|$) and ports 2-4 (i.e. $|S_{42}|$) are significantly higher (> -15 dB) than that exhibited by ports 2-3 (i.e. $|S_{32}|$) and ports 1-4 (i.e. $|S_{41}|$). It is also important to note that the maximum value of the L_2 band mutual coupling is -9 dB and this is 6 dB higher than that of the L_1 band due to the relatively smaller electrical separation between the antennas at the L_2 band frequencies. Therefore, the particular focus of this work is to maintain the L_1 band performance and utilize the BC-SRRs to reduce L_2 band critical mutual coupling responses (i.e. $|S_{31}|$ and $|S_{42}|$). To utilize the BC-SRRs for suppressing the mutual coupling [40], the L_2 band magnetic field (H) distribution within the array was subsequently investigated. Figure 2.4(a) depicts the H-field distribution at z=250 mil when

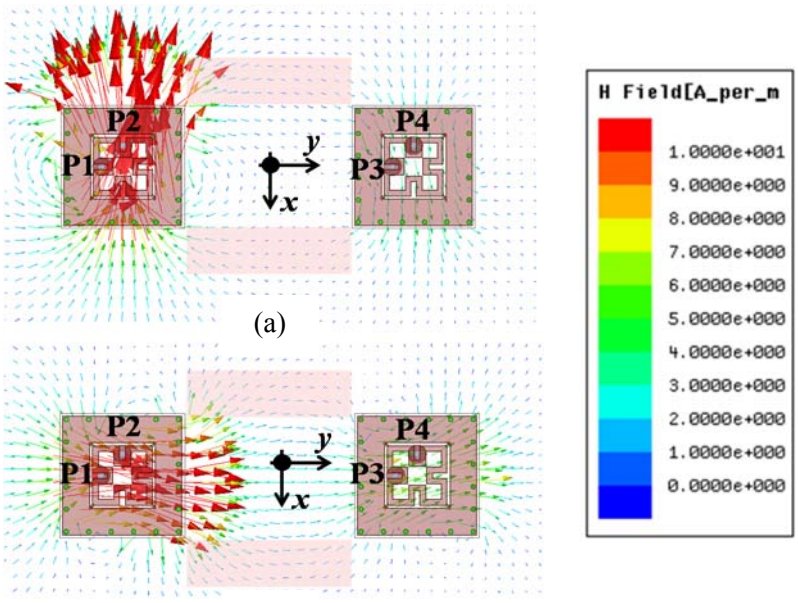

Figure 2.4: Simulated magnetic field distribution within the 2×1 CDL GPS array. z=250 mil when: a) port#1 and b) port#2 are excited. All the remaining ports are terminated with 50 Ω.

port #1 is excited and other ports are terminated with 50 Ω matched loads. A volumetric field plot also reveals that a similar field distribution exists within the majority of the volume between the planes formed by the ground (i.e. z=0) and the antenna top surface (i.e. z=500 mil). As seen, the strongest H-field concentration nearby the antenna is on the side surfaces parallel to the y-z plane. Further analysis shows that the strongest electric (E) field concentration is on the side surfaces parallel to the x-z plane. Consequently, port #1 excitation gives a field distribution that resembles the E-plane coupling of patch antennas. The H-field distribution when port #2 is excited and other ports are terminated with matched loads is shown in Figure 2.4(b). This field distribution is similar to the one observed in H-plane coupling of patch antennas. Hence, the metamaterial resonator arrangements used in previous publications for decoupling linear arrays [10, 35] cannot readily provide mutual coupling suppression for the presented array. More specifically, the BC-SRRs should be strategically located and oriented to simultaneously interact with the fields associated

with the *E* and *H*-plane couplings. The *H*-field distribution within the highlighted dashed regions depicted in Figure 2.4(a) and (b) exhibits components that are oriented along the *y*-axis for both port excitations. Therefore, in these regions, periodically arranged BC-SRR stacks can potentially provide concurrent *E* and *H* plane mutual coupling suppression if their loop axes are also oriented along the *y*-axis. It is important to note that other types of MNG metamaterials such as the ones based on spiral resonators or edge coupled split ring resonators can also be utilized for the mutual coupling reduction. Since BC-SRRs were shown to provide the smallest size with comparable or less absorption loss [41], they were selected for implementation of the presented GPS array.

2.4. Mutual Coupling within the 2×2 CDL GPS Array

2.4.1. BC-SRR Design

The design of the L_2 band BC-SRR unit cell follows the well-established procedure described in [42]. Figure 2.5(a) and (b) depict the side and 3D views of the unit cell designed for L_2 band operation. The key parameters of the unit cell are the relative dielectric constant of the substrate, the dimensions of the substrate, length and width of the oppositely oriented metallic open loops, and their gap size. For obtaining a small unit cell size, a 50 mil thick high permittivity Rogers 3010® (ε_r=10.2, tan(δ)=0.0022) substrate was selected for the design. The length of the unit cells along the z-axis was constrained to 0.5" in order to be identical with the antenna substrate thickness. The remaining dimensions were determined through parametric studies by modeling the unit cell with periodic boundary conditions and extracting the equivalent material properties from the transmission and reflection coefficients [43, 44]. Specifically, the unit cell dimensions shown in Figure 2.5 resulted in the desired L_2 band operation with 196.8 mil periodicity (p) ($<< \lambda_0$ at L_2) along the y-axis. As seen from the simulated S-parameters in Figure 2.5(c), the $|S_{21}|$ response of this unit cell exhibits a transmission zero about 1.227 GHz. The extracted effective permeability

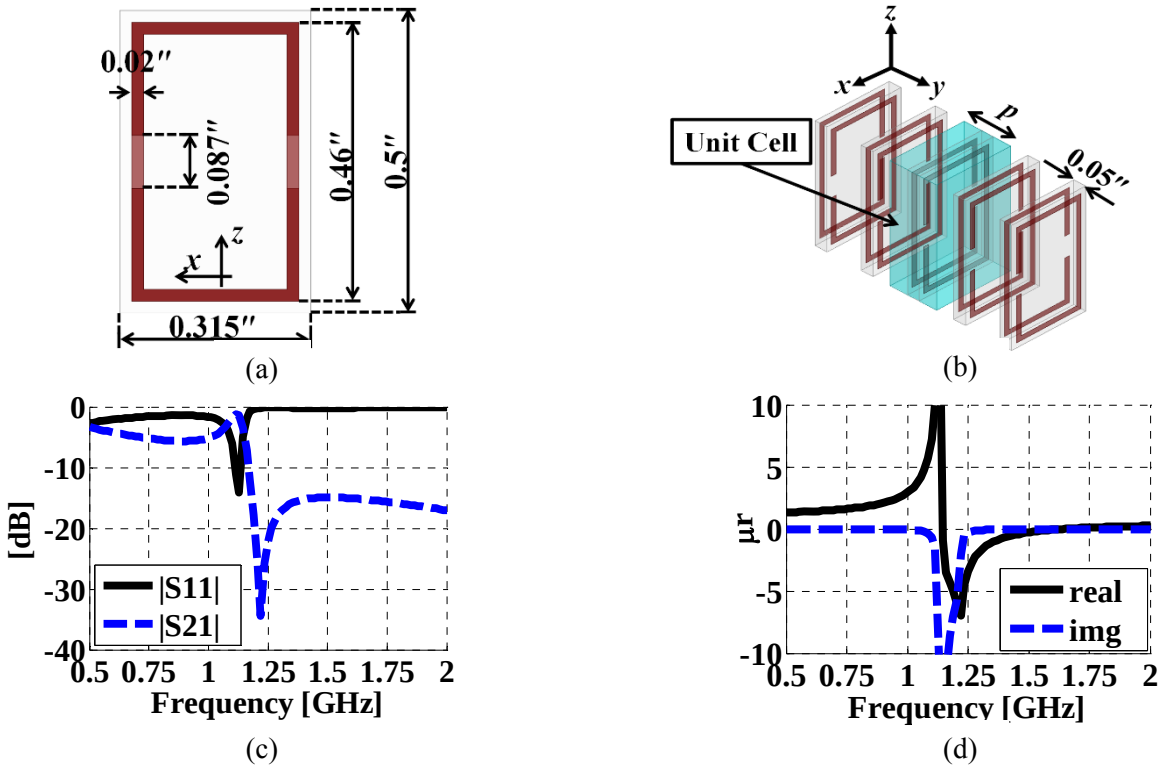

Figure 2.5: The details of the BC-SRR unit cell. a) BC-SRR side view, b) 3D view of a periodic arrangement of BC-SRRs with one cell highlighted, c) simulated $|S_{11}|$ and $|S_{21}|$ response, and d) extracted effective permeability of the designed BC-SRR cell.

[43] in Figure 2.5(d) demonstrates that an MNG medium is clearly realized over the entire L_2 band with a resonance frequency of 1.227 GHz.

2.4.2. 2×1 CDL GPS Array Loaded with BC-SRRs

Figure 2.6(a) depicts the 2×1 CDL GPS array when the BC-SRRs are placed at the locations identified in the previous section. A particular goal is to keep the number of the BC-SRR stacks to a minimum for low cost implementation and compactness. In addition, the good impedance matching of the antenna ports (i.e. $|S_{ii}|$<-10 dB) must be maintained after the inclusion of the BC-SRRs. Therefore, several parametric studies were performed with two periodic stacks of BC-SRRs and this configuration was found to be adequate for mutual coupling suppression. The first set of parametric studies was carried out to determine the best position of the BC-SRRs

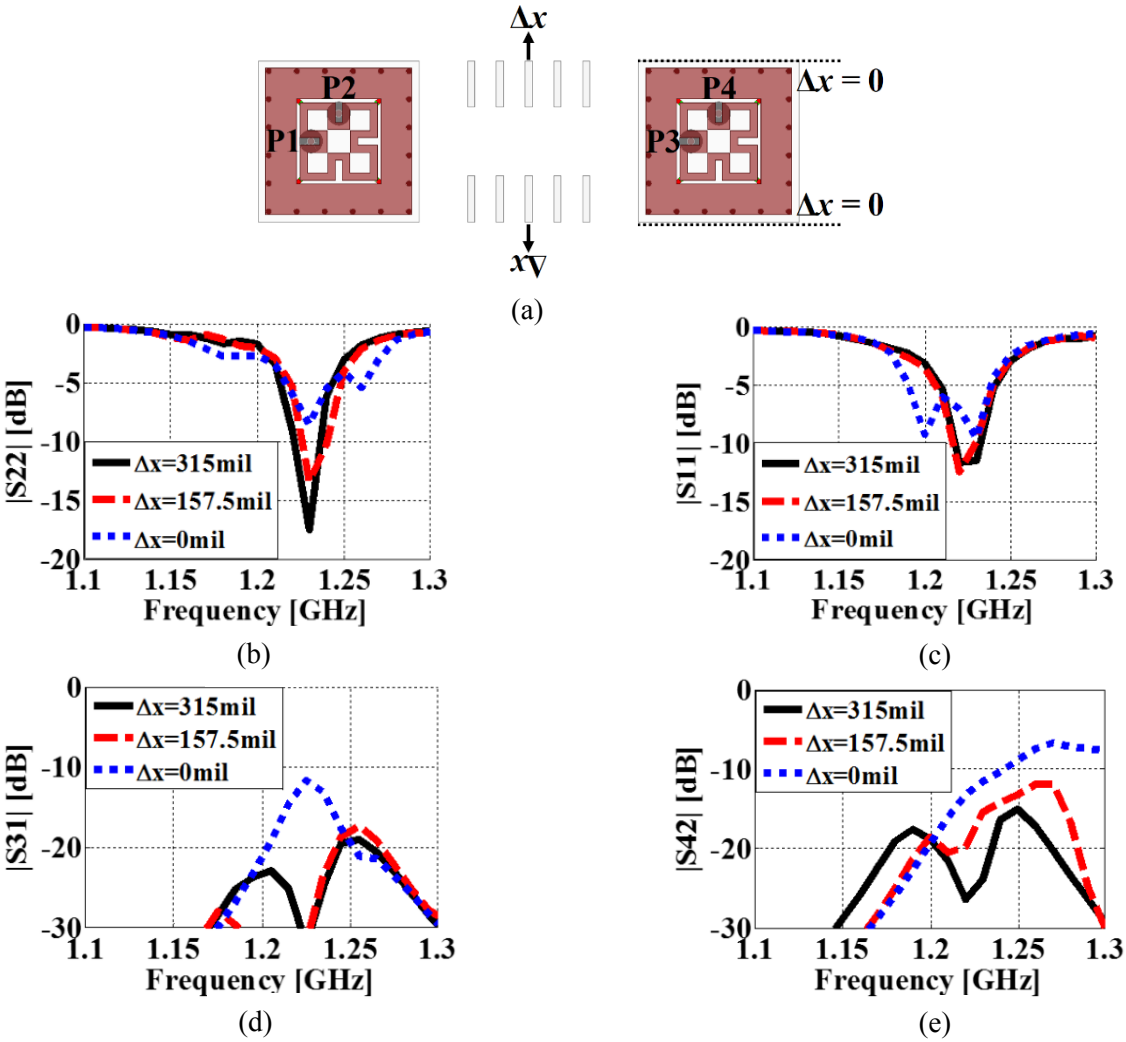

Figure 2.6: Parametric study for the 2×1 GPS array. a) 2×1 GPS array loaded with two stacks of BC-SRR unit cells and simulated L_2 band S-parameters for different values of Δx: b) $|S_{11}|$, c) $|S_{22}|$ d) $|S_{31}|$ and e) $|S_{42}|$.

by using stacks consisting of 5 unit cells. As shown in Figure 2.6(a), the top and bottom BC-SRR rows were moved along the ± x-axis with Δx=157.5 mil increments (i.e. half of the unit cell width) until good impedance matching performance and mutual coupling suppression were concurrently achieved. The simulated S-parameters in Figure 2.6(b)-(e) demonstrate that Δx=0 results in a deteriorated response in the impedance matching (i.e. $|S_{11}|$ and $|S_{22}|$). Good impedance matching can be accomplished for both Δx=157.5 mil and Δx=315 mil. However, the latter provides a >5dB

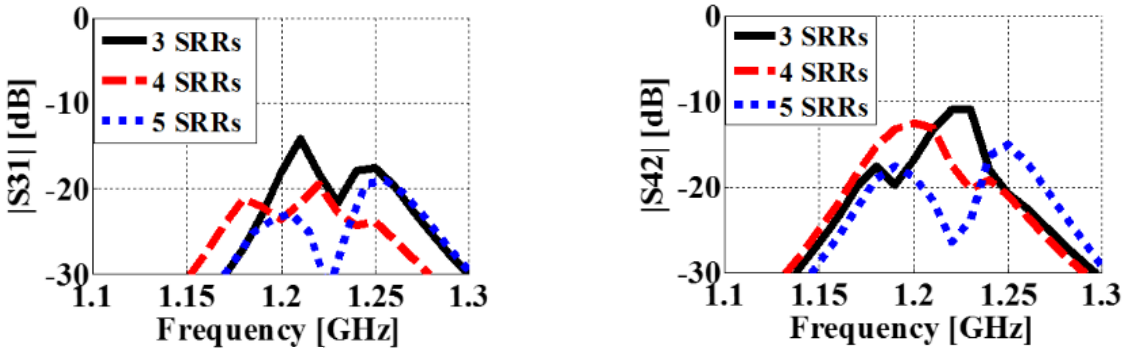

Figure 2.7: Simulated L_2 band mutual coupling within the 2×1 GPS array. For Δx=315 mil and when different numbers of unit cells are employed within the BC-SRR stacks: a) $|S_{31}|$ and b) $|S_{42}|$.

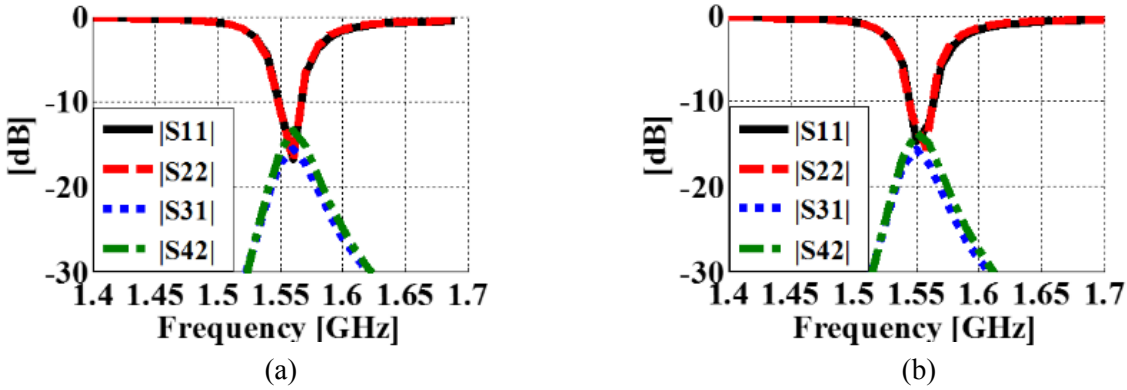

Figure 2.8: Simulated L_1 band impedance matching and coupling of the 2×1 array. a) absent and b) present.

better $|S_{42}|$ suppression at the center of the L_2 band frequency. Figure 2.7 demonstrates the mutual coupling performance as the number of unit cells employed within the BC-SRR varied from 3 to 5. It is clearly observed that the coupling suppression is better with larger numbers of unit cells. Specifically, $|S_{31}|$ and $|S_{42}|$ are concurrently below -25dB at center frequency of the L_2 band for N=5. Increasing the number of unit cells beyond N=5 results in an overlap in BC-SRRs when the 2×1 array is generalized to the 2×2 configuration by employing the 90^0 rotational symmetry (e.g. see Figure 2.1(a)). It is also important to characterize the potential effects of the L_2 band BC-SRR stacks on the L_1 band performance of the dual-band array. As shown in Figure 2.8, both L_1 band

impedance matching and mutual coupling performances are not affected by the presence of the BC-SRRs and therefore, their effect is negligible in L_1 band operation.

To experimentally verify the mutual coupling performance, a 2×1 CDL GPS antenna array was fabricated and tested with and without the BC-SRRs. As expected, the impedance matching was not significantly affected due to the presence of the BC-SRR stacks (see Figure 2.9(a)). Moreover, the resonance frequencies of the antennas were almost maintained at 1226 MHz for the

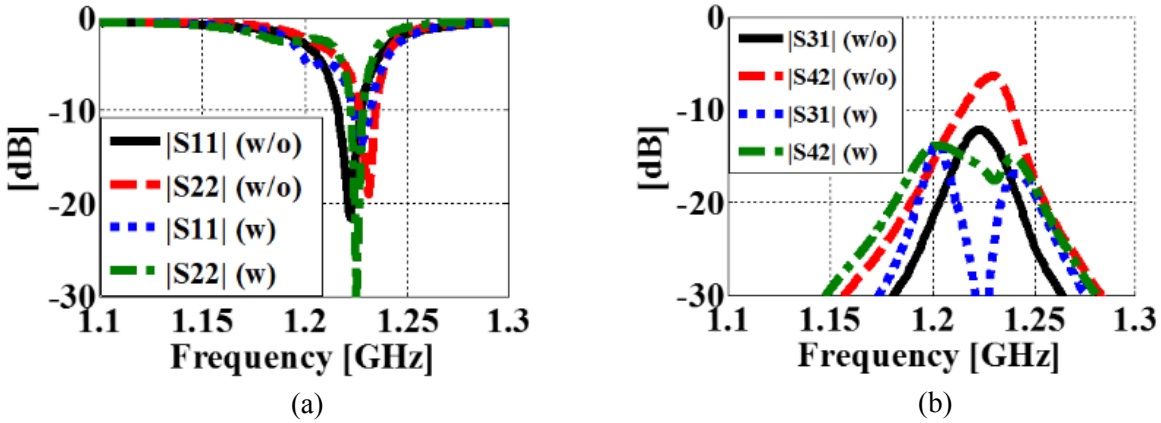

Figure 2.9: Measured L_2 band S-parameters of the conventional and BC-SRR loaded 2×1 GPS array. a) Impedance matching, and b) mutual coupling performances.

array within the presence of the BC-SRRs. Figure 2.9(b) presents the measured $|S_{31}|$ and $|S_{42}|$ of the array. The $|S_{31}|$ and $|S_{42}|$ are simultaneously suppressed by 10 dB and 15 dB, respectively. These results agree well with the simulated data in Figure 2.7.

2.4.3. 2×2 CDL GPS Array Loaded with BC-SRRs

The final design step is to employ the 90^0 rotational symmetry of the structure to construct the BC-SRR loaded 2×2 CDL GPS array (see Figure 2.1(a)). Differently than the 2×1 array, in the 2×2 configuration, each antenna element is within the close proximity of the BC-SRRs from two sides. Nevertheless, the simulated mutual coupling between the antenna #1 and #2 in the absence and presence of the BC-SRRs demonstrates that $|S_{31}|$ and $|S_{42}|$ are still simultaneously reduced by

more than 9 dB around the center frequency of the L_2 band as depicted in Figure 2.10. Moreover, both antennas continue to be well matched to their feed lines. As already noted, the design procedure was carried out by assuming that the mutual coupling between the adjacent antennas of the 2×2 array is identical. This can be verified from Figure 2.11(a) and (b) by observing that the *E*-plane ($|S_{31}|$, $|S_{62}|$, $|S_{84}|$ and $|S_{75}|$) and *H*-plane ($|S_{51}|$, $|S_{42}|$, $|S_{73}|$ and $|S_{86}|$) couplings of the adjacent antennas are almost identical. In addition, Figure 2.11(c) and (d) show simultaneous reduction of the *E* and *H*-plane couplings when BC-SRRs are present.

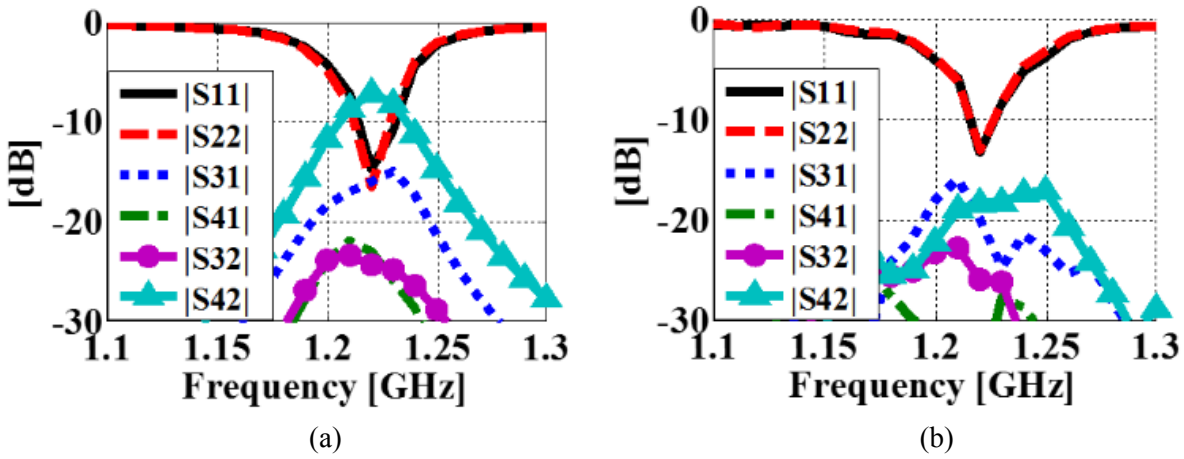

Figure 2.10: Simulated *S*-parameters between antenna #1 and #2 within the 2×2 CDL GPS array. a) conventional, and b) BC-SRR loaded.

Although the design procedure was carried out by considering that the ports of the CDL GPS antennas can be individually excited, this is not the case in practical applications. In general, the antenna elements of GPS arrays are excited from a single feed that is connected to an internal quadrature hybrid [45]. Therefore, the mutual coupling performance for this specific case is of interest. This configuration will also be utilized in the following section for characterizing the nulling capability of the BC-SRR loaded obtained from a full wave electromagnetic solver were imported into Agilent Advanced Design System (ADS® [46]) and utilized in conjunction with an

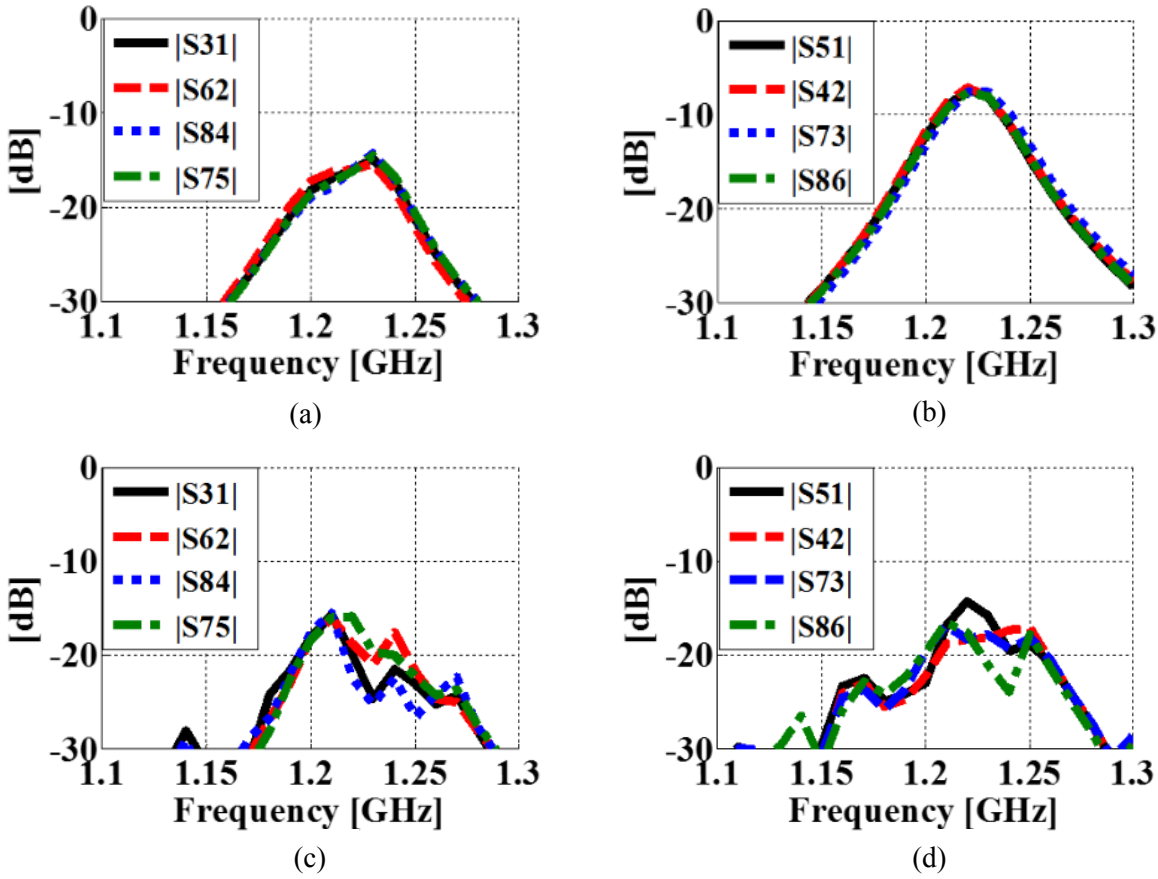

Figure 2.11: Simulated coupling between the adjacent antennas within the 2×2 array. a) *E*-plane coupling without BC-SRRs, b) *H*-plane coupling without BC-SRRs, c) *E*-plane coupling with BC-SRRs and d) *H*-plane coupling with BC-SRRs.

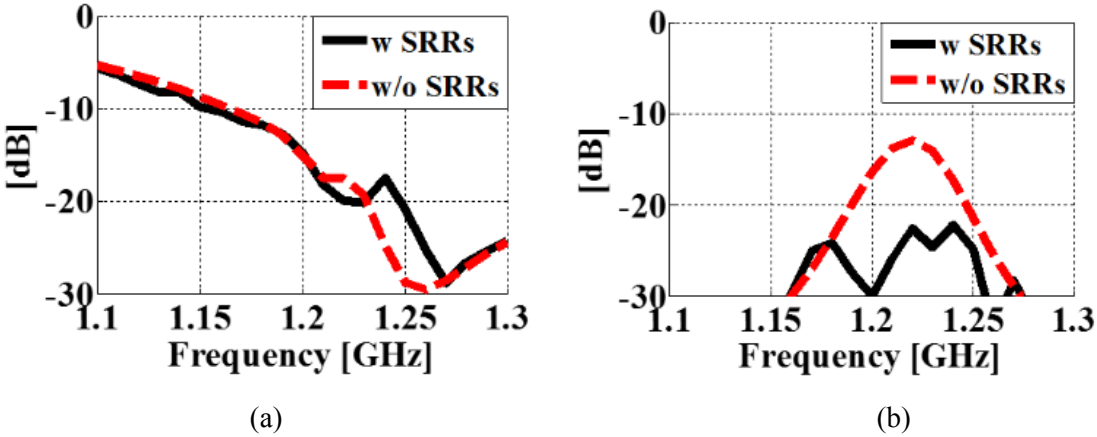

Figure 2.12: Simulated L_2 band *S*-parameters between antennas #1 and #2 of the conventional and BC-SRR loaded GPS array. Each antenna is fed with an ideal quadrature hybrid: a) Impedance matching and; b) mutual coupling performance.

ideal hybrid model. Figure 2.12 presents the impedance matching and mutual coupling between the antennas #1 and #2 of the 2×2 CDL GPS array. Due to the quadrature hybrid [47], a broadband impedance matching is observed for both array configurations (see Figure 2.12(a)). On the other hand, the mutual coupling between the antenna ports is reduced by 10 dB at 1.227 GHz as shown in Figure 2.12(b) when the CDL GPS array is loaded with the BC-SRRs. The simulated impedance matching and mutual coupling results obtained among the ports of the adjacent antenna elements are very similar and not shown. Figure 2.13(a) demonstrates the fabricated prototype of the 2×2 CDL GPS array loaded with the BC-SRRs. Each antenna element is fed using a quadrature coupler feed network [48] from the back side of the array as depicted in Figure 2.13(b). The fabricated BC-SRRs were manually glued to the ground plane. The simulated and measured mutual coupling between the antenna #1 and #2 are compared in Figure 2.14 and a good agreement is observed. The measured mutual coupling at 1.227 GHz with the absence and presence of BC-SRRs is -13 dB and -25 dB, respectively.

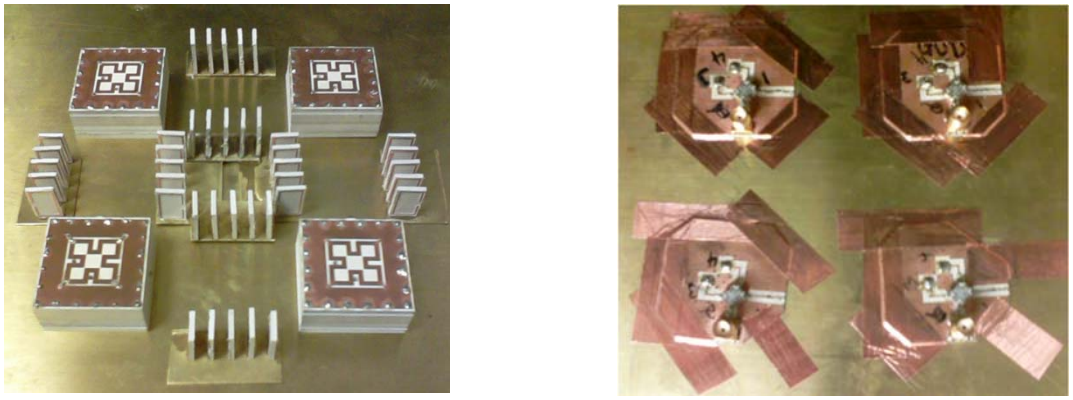

(a) (b)

Figure 2.13: a) Fabricated 2×2 CDL GPS array loaded with the BC-SRRs. The BC-SRRs are glued to the ground plane, and b) the quadrature coupler feed networks were positioned at the backside of the array and attached to the 24"×24" brass ground plane using copper tapes.

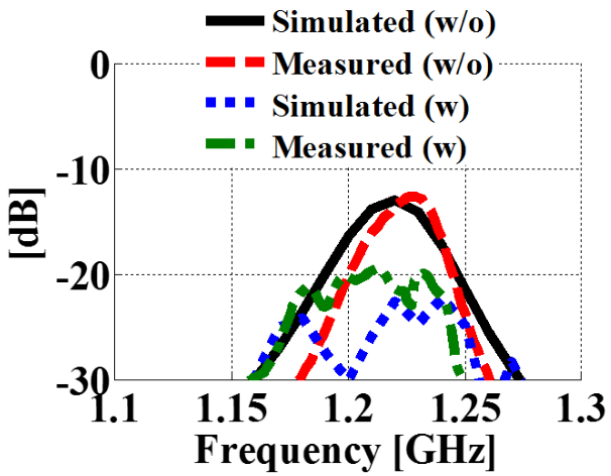

Figure 2.14: Comparison of the measured and simulated L_2 band mutual coupling. The shown data is for the coupling between antennas #1 and #2 of the conventional and BC-SRR loaded 2×2 CDL GPS array.

2.5. Nulling Capability

Mutual coupling has been shown to negatively impact the performance of adaptive antenna arrays. For example, references [49, 50] demonstrated that mutual coupling reduces the signal-to-interference-plus-noise ratio (SINR) of adaptive algorithms. It was also shown to degrade the accuracy of direction of arrival (DOA) algorithms [51, 52] and affect nulling performance of linear dipole arrays in terms of null accuracy and depth [53]. In this section, we investigate the change in the nulling capability of the CDL GPS array when it is loaded with the BC-SRRs to exhibit a reduced amount of mutual coupling. As detailed in the following section, the embedded element patterns (i.e. radiation pattern of an antenna element when the other antennas of the array are terminated with 50 Ω matched loads) were utilized to determine the antenna weighting coefficients for generating nulls towards desired directions. It is important to note that calculating the antenna weights using this method is not feasible for practical applications as it requires the pre-knowledge of the embedded field patterns and the location of the interfering signals. In realistic scenarios, adaptive nulling algorithms are used to determine the antenna weights [49]. Nevertheless, the

method utilized below can be considered to be suitable for characterizing the nulling capability that can be accomplished by the adaptive algorithm as it makes use of the pre-knowledge of the realized embedded element gains and determines the weights using the least square method. Specifically, with this approach, we investigate the nulling capability of the 2×1 and 2×2 CDL GPS arrays. Through simulations and measurements, we demonstrate that the BC-SRR loaded CDL GPS arrays with reduced mutual coupling generate deeper nulls in the total array pattern with better angular accuracy as compared to the conventional CDL GPS array.

2.5.1. Nulling Capability of the BC-SRR Loaded 2×1 GPS Array

Generally speaking, an *N* element antenna array can produce a total of *N-1* distinct nulls in its radiation pattern if the elements are excited with proper excitation coefficients (i.e. weights). Specifically, these weights need to satisfy the relation [54]:

$$\overrightarrow{E_1}(\theta_i, \phi_i) + \sum_{n=2}^{N} w_n \overrightarrow{E_n}(\theta_i, \phi_i) = 0 \tag{2.1}$$

to generate the nulls along the desired directions (θ_i, ϕ_i) (i = 1, 2,.., N-1), where $\overrightarrow{E_n}(\theta_i, \phi_i)$ and w_n denote the embedded electric field pattern and weight of the n^{th} element, respectively. In the above equation, the weight of the first element is selected as 1, since the weights are complex quantities that are defined relative to each other and can be normalized with respect to the first element without loss of generality. For a circularly polarized antenna array, each electric field quantity in (2.1) can be written as a superposition of its corresponding RHCP and LHCP components. Therefore, (2.1) can be split into two distinct equations:

$$E_{1RHCP}(\theta_i, \phi_i) + \sum_{n=2}^{N} w_n E_{nRHCP}(\theta_i, \phi_i) = 0 \tag{2.2}$$

$$E_{1RHCP}(\theta_i, \phi_i) + \sum_{n=2}^{N} w_n E_{nRHCP}(\theta_i, \phi_i) = 0 \tag{2.3}$$

Equations (2.2) and (2.3) form an over-determined system:

$$[\bar{\bar{A}}]_{2(N-1)\times(N-1)}[\bar{w}]_{(N-1)\times 1} = [\bar{b}]_{2(N-1)\times 1}. \tag{2.4}$$

If the cross polarization (i.e. LHCP patterns) of the antenna elements are not negligible and nulls are desired to be formed in the total field pattern (e.g. the jamming signals have different polarizations with respect to each other). The over-determined system of (2.4) can be solved for the weights using the least square method [55]. It is important to note that if the embedded antenna patterns of the array exhibit zero cross-polarization, the solution for the weights will be dominated by equation (2.2). Consequently, (2.4) would reduce to a square system and lead to weights that would ideally generate perfect nulls within the total field pattern. Hence, in this situation, the nulling capability of the array can be considered to be maximized. This ideal case, however, may not exist in a practical circularly polarized array. In addition, high levels of mutual coupling may imply that the embedded element patterns are distorted with respect to that generated by the stand-alone element and exhibit radiation with increased cross polarization. Therefore, reducing the mutual coupling within the array can improve the nulling capability. Figure 2.15 depicts the simulated and measured L2 band RHCP and LHCP elevation plane gain patterns of the 2×1 CDL GPS array at the ϕ=90^0 azimuth cut when both elements are excited equally in-phase (i.e. $w1$=$w2$=1). An in-house MATLAB [56] code was developed to construct the embedded RHCP and LHCP element patterns from the measurements taken by a linearly polarized reference horn. The same code was also extended to implement the equation system given in (2.4) and generate the array pattern subject to the particular weight choices. As seen, the simulated and measured gain patterns both demonstrate that the BC-SRR loaded arrays with the reduced mutual coupling exhibit

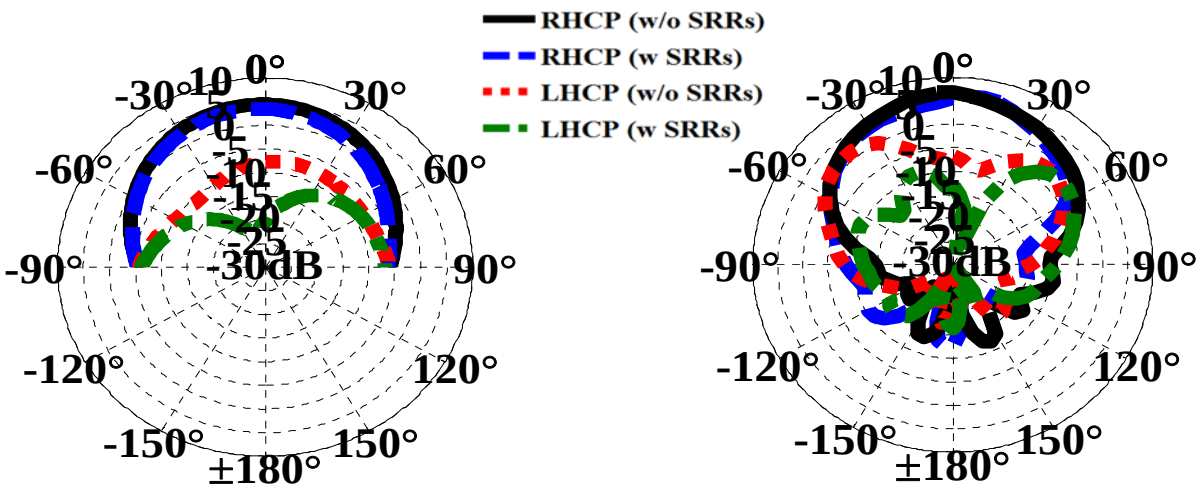

(a) (b)

Figure 2.15: Elevation plane ($\phi = 90^0$) L_2 band gain patterns of the 2×1 GPS array. The presence and absence of BC-SRRs are considered: a) Simulated patterns over an infinite ground plane, b) Measured patterns over the 24"×24" brass ground plane.

lower levels of LHCP gain. This is due to the lower cross-polarization gains observed in the embedded element patterns. Specifically, the measured LHCP gain of the array is 7 dB lower within the presence of the BC-SRRs at the broadside. It is important to note that the presented infinite ground plane simulations represent an ideal scenario. On the other hand, the measurements were taken and BC-SRRs over the large ground plane. Therefore, demonstrating the nulling capability through simulations and experiments are equally important to understand the performance and limitations of the presented BC-SRR loaded arrays. It should also be noted that the presence of the BC-SRRs does not significantly affect the RHCP gain as was also expected from the extracted permeability values (see Figure 2.15). More specifically, the simulated results show a radiation efficiency of 81% for the BC-SRR loaded array and this is only 6% lower than the efficiency of the unloaded array. Having verified that the cross-polarization gain of the BC-SRR loaded array is reduced, we proceeded by utilizing equation (2.4) to calculate the weights for achieving a pattern null. As an example, Figure 2.16 presents the simulated gain patterns of the

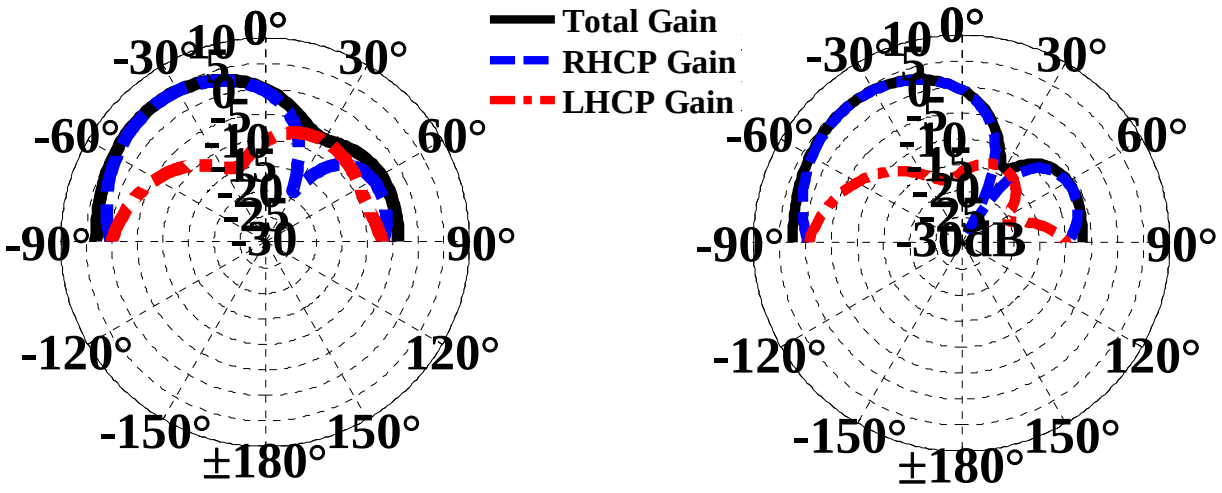

(a) (b)

Figure 2.16: Simulated elevation plane ($\phi = 90^0$) L_2 band gain patterns of the 2×1 GPS array. The absence [(a)] and presence [(b)] of BC-SRRs cases are studied when a total field pattern null is desired along the θ=30^0 direction.

conventional and BC-SRR loaded 2×1 CDL GPS arrays when the desired pattern null is located at(θ, ϕ)= (30^0, 90^0). Specifically, the null depth in the total gain pattern is enhanced by 8 dB with the BC-SRR loaded array. It is evident from Figure 2.16(a) that the relatively high LHCP gain of the conventional array deteriorates its nulling capability. These results were also verified experimentally as shown in Figure 2.17. The total measured gain pattern of the BC-SRR loaded array exhibits a 9 dB deeper null and agrees well with the simulation based expectations. In general, we have observed similar null depth enhancements for various interferer directions with the BC-SRR loaded 2×1 CDL GPS array. As a second example, in Figure 2.17(c) and (d), we present the measured gain patterns for the conventional and BC-SRR loaded arrays when they are configured to generate a null towards (θ, ϕ) = (0^0, 90^0). In this scenario, it is observed that the conventional array generates a -8 dB null, whereas the BC-SRR loaded array produces a -20 dB deep null towards the desired direction.

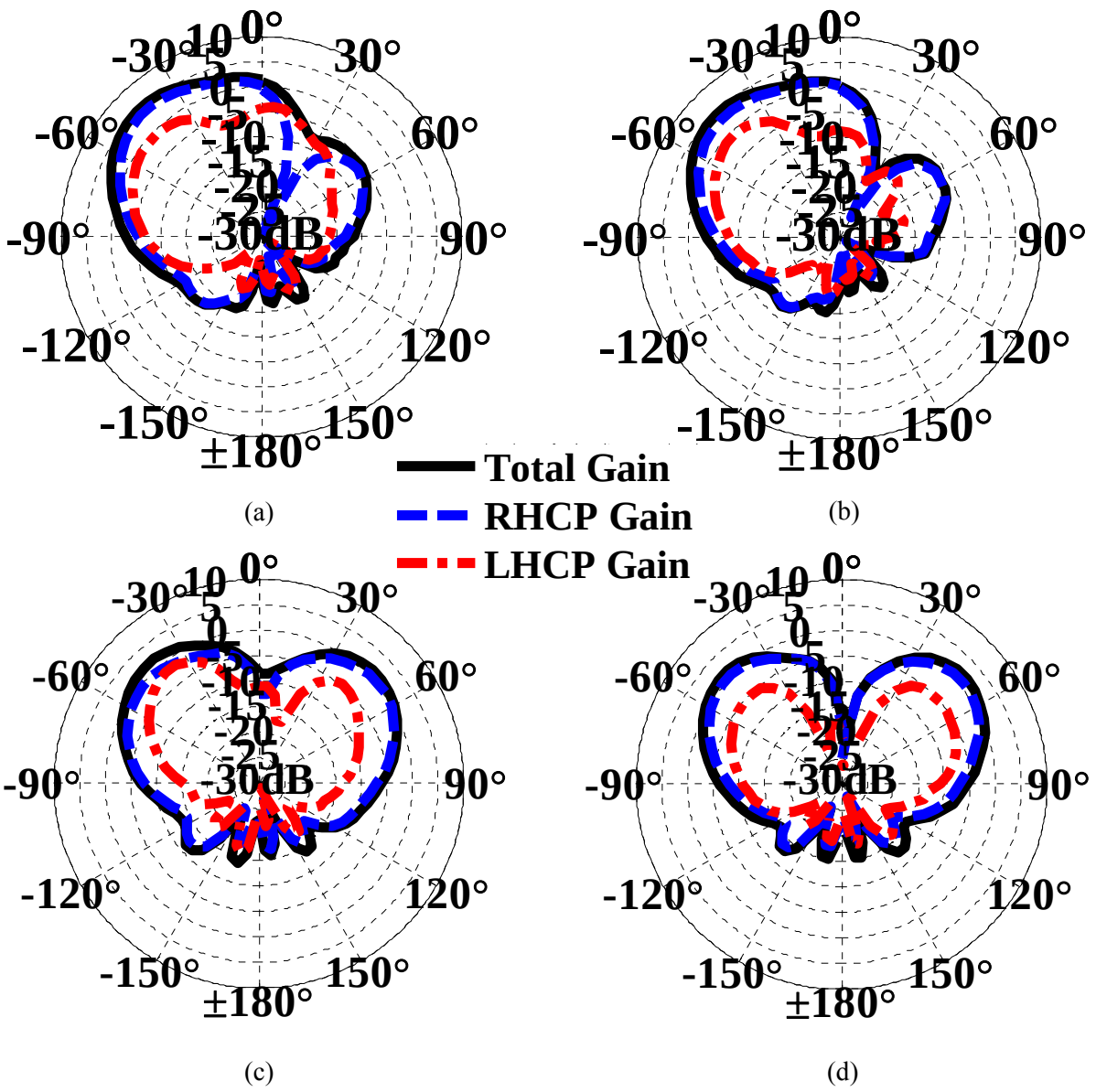

Figure 2.17: Measured elevation plane (ϕ=90^0) L_2 band gain patterns of the 2×1 GPS array. The absence [(a)&(c)] and presence[(b)&(d)] of BC-SRRs cases are studied when a total field pattern null is desired along the θ=30^0 [(a)&(b)] and θ=0^0 [(c)&(d)] directions.

2.5.2. Nulling Capability of the BC-SRR Loaded 2×2 GPS Array

The simulations and measurements carried out by the BC-SRR loaded 2×2 CDL GPS array have demonstrated an improved nulling capability in terms of null depths and accuracy as compared to the conventional array. Specifically, the null depth is improved by more than 10 dB

when BC-SRRs are used. As an example, in Figure 2.18(a) we demonstrate a scenario in which three distinct nulls are desired at the θ=75^0 azimuth plane along the ϕ=45^0, 150^0 and 250^0 directions. The simulated normalized patterns show that both the conventional and BC-SRR loaded arrays can generate a null with similar depth along the ϕ=250^0 direction. However, the conventional array clearly fails to produce a null along ϕ=45^0 direction due to its high cross polarization level. In addition, the pattern null desired along the ϕ=150^0 direction is miss-

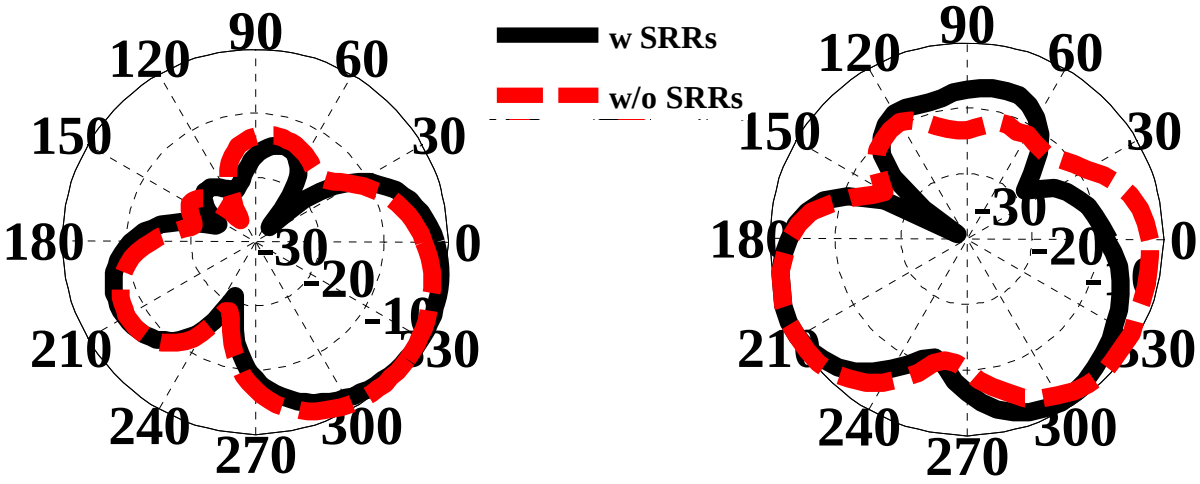

(a) (b)

Figure 2.18: Simulated [(a)] and measured [(b)] normalized azimuth plane (θ=75^0) L_2 band total gain patterns of the 2×2 CDL GPS array within the presence and absence of BC-SRRs. The total field pattern nulls are desired along the ϕ=45^0, 150^0 and 250^0 directions.

positioned by 15^0. On the other hand, the BC-SRR loaded array generates all three nulls along the desired directions. Moreover, the nulls are associated with < -20 dB lower realized gain as compared to the maximum realized gain. The measured total normalized patterns presented in Figure 2.18(b) are in good agreement with the performance predicted by the simulations. Specifically, the BC-SRR loaded array can generate the pattern nulls more accurately along the desired directions. Additionally, the nulls are associated with <-11dB lower measured realized gain as compared to the maximum realized gain by the array.

2.6. Concluding Remarks

The design and nulling capability of a compact 2×2 CDL GPS antenna array loaded with BC-SRRs were presented. By carefully choosing the location and orientation of the BC-SRRs within the array layout, a 10 dB L_2 band mutual coupling reduction was realized without degrading the dual-band impedance matching performance of the antenna elements in the case of $\lambda_0/3.7$ inter-element spacing. Through simulations and experiments, it was demonstrated that the reduced L_2 band mutual coupling leads to a better nulling capability in terms of accuracy and null depth. Specifically, the measured null depths were improved by more than 8 dB due to the presence of the BC-SRR loading. The presented array fits within an overall footprint size of 4.3"×4.3" and can be potentially miniaturized further for different inter-element spacing. To the best of our knowledge, previous studies have not considered any methods for reducing the mutual coupling within compact circularly polarized GPS arrays and discussed their effects on the array nulling. Therefore, the presented results can motivate further design considerations and improvements.

CHAPTER 3: MICROFLUIDIC BASED KA-BAND BEAM SCANNING FOCAL PLANE ARRAY

3.1. Introduction

Microfluidic enabled reconfigurability has been recently proposed for implementing a variety of novel microwave components. For example, dynamically moving the liquid metal slugs formed inside the microfluidic tubes was utilized in [57] as variable capacitors to develop a frequency tunable frequency selective surface (FSS). Likewise, a frequency-agile bandpass filter was realized in [58] by constructing the filter partially from liquid metal to dynamically reshape its resonators. In [59], the movement of liquid metal slug inside the microfluidic tubes was utilized to parasitically load a circular loop antenna to generate beam steering functionality. Microfluidic channels filled by liquid metal have been used in [60] and [61] to develop a novel class of flexible/stretchable dipole and patch antennas, respectively. Furthermore, a flexible patch antenna constructed by filling meandered microfluidic channels with liquid metal was introduced in [62] and a frequency reconfigurable annular slot antenna based on digital microfluidics was shown in [63]. Different from the aforementioned existing designs, this paper for the first time explores the use of microfluidic based reconfigurability for the realization of beam scanning focal plane arrays (FPAs). Specifically, a 1D 8 element FPA is designed to operate at Ka-band (30 GHz) and consists of interconnected microfluidic reservoirs and channels constructed by bonding Polydimethylsiloxane (PDMS) (ε_r=2.8, tanδ=0.02) and liquid crystal polymer (LCP) (ε_r=2.9, tanδ=0.0025) substrates. The antenna element of the FPA is a small volume (2.5 µl) of liquid metal

mercury residing inside a low loss Fluorinert™ FC-77 (ε_r=1.9, tanδ=0.0005) solution. The FPA is placed behind an 8 cm diameter extended hemispherical Rexolite (ε_r=2.56, tanδ=0.0026) lens. Beam scanning is accomplished by moving the liquid metal antenna among the reservoirs by using an external pump. The proximity coupled feed network of the array is passive (i.e. no RF switches) and designed strategically to accommodate the position variation of the liquid metal antenna

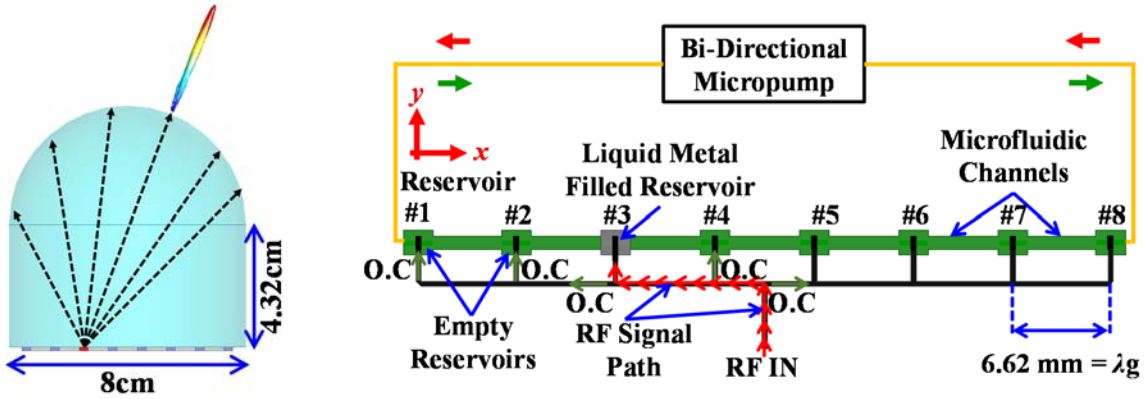

(a) (b)

Figure 3.1: a) Conceptual illustration of a FPA located behind an extended hemispherical dielectric lens, and b) the proposed microfluidic enabled FPA consisting of reservoirs connected using micro channels. One reservoir acts as a patch antenna when is filled with liquid metal. A bi-directional pump is used to move the liquid metal among the reservoirs to scan the beam.

element. This is in contrast to the conventional mm-wave high gain beam scanning array realizations that demand substantial hardware integration in their feed networks in terms of RF switches and phase shifters [21, 64-66]. Therefore, the technique is promising for high-power handling and the low-cost realization of millimeter-wave high gain beam scanning antenna arrays. The presented FPA is shown to operate with measured 7^0 half power beamwidth (HPBW), >21 dB realized gain, 3.3% $|S_{11}|$<-10 dB bandwidth and provide $\pm 30^0$ beam scanning range in its elevation plane.

3.2. Microfluidic Based Beam Scanning FPA Design

Figure 3.1 demonstrates the lens, microfluidic reservoir and feed network parts of the 8 element beam scanning FPA. The 8 cm diameter hemispherical Rexolite lens is designed to exhibit an extension length of 4.32 cm based on the guidelines provided in [27]. As shown in Figure 3.1(b), the FPA consists of 8 microfluidic reservoirs that are interconnected with channels. A reservoir is filled up with liquid metal Mercury (σ=1×10^6 S/m) to realize a patch antenna. The remaining volume of microfluidic reservoir and channel assembly is filled out with the Fluorinert™ FC-77

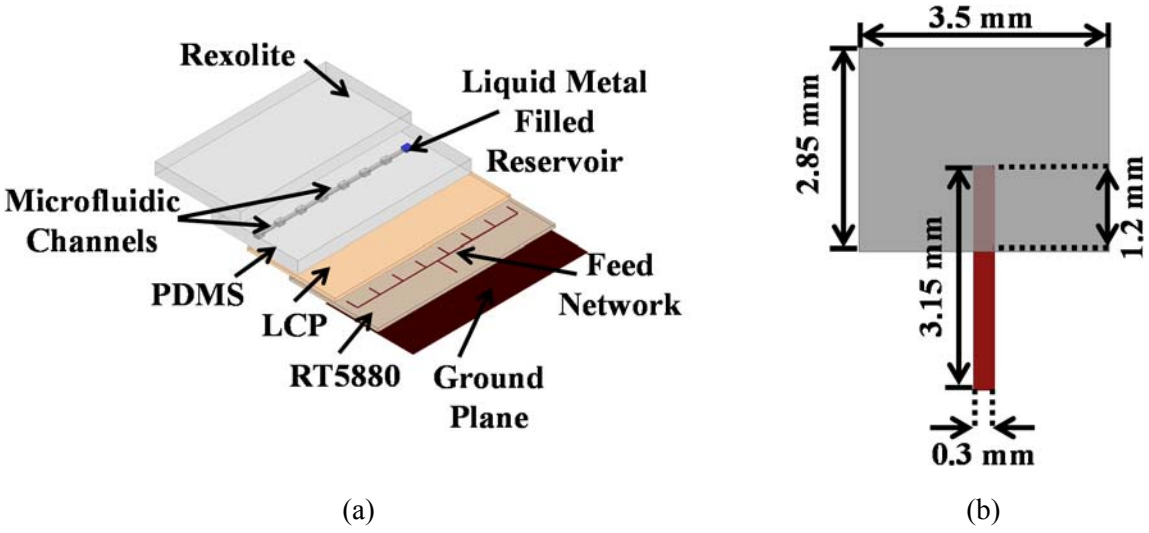

(a) (b)

Figure 3.2: a) 3D view of the metal and substrate stack up of the designed array, and b) Top view of the 30 GHz proximity fed patch antenna.

solution acquired from Sigma Aldrich®. The antenna can be repositioned to the adjacent reservoirs with the aid of a single external pump mechanism that is capable to circulate the solution. The microfluidic reservoirs are placed over proximity coupled microstrip line feed network. The length of the feed stubs residing below the reservoirs were designed to be $\lambda_g/2$ (λ_g = 6.62 mm at 30 GHz) to present open circuit (O.C.) condition to the feed line when the reservoirs are empty of liquid metal. In addition, the separation between the stubs were designed to be λ_g to provide the necessary

O.C. conditions in order to direct the RF power to the liquid metal filled reservoir without needing any active RF switches. The substrate stack-up of the FPA is depicted in Figure 3.2(a). For prototyping purposes, the 250 μm thick microfluidic reservoir and channels are modeled inside 2 mm thick PDMS substrate. The channel molds are sealed by bonding them to a 50 μm thick LCP layer. The PDMS-LCP assembly is placed over a 127 μm thick Rogers RT5880 (ε_r=2.2, tanδ=0.0007) substrate that supports the passive proximity coupled microstrip line feed network. Figure 3.2(b) presents the dimensions of the proximity fed patch antenna designed by using the Momentum suite of the Agilent's Advanced Design System (ADS®). In these simulations, a semi-

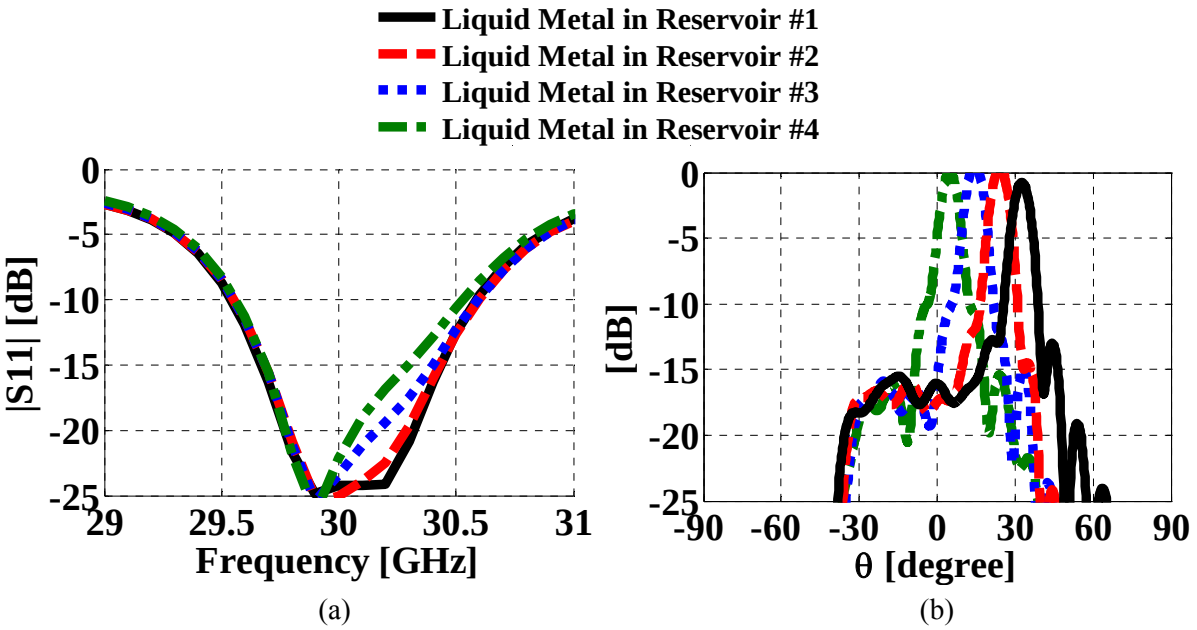

Figure 3.3: Simulated performance of the microfluidic based FPA array: a) $|S_{11}|$ performance and b) array normalized radiation pattern. The patterns are normalized with respect to pattern #4 maxima (ϕ=0^0).

infinite half-space is assumed over the PDMS layer to model the presence of the electrically large Rexolite lens [67, 68]. The simulated $|S_{11}|$ performance as the liquid metal patch is moved from reservoir #1 to #4 over the passive proximity coupled feed network is depicted in Figure 3.3(a) (due to the array symmetry, throughout the manuscript, only the performance of the liquid metal

antenna in reservoirs #1 to #4 are presented). As seen, resonance frequencies of 30 GHz and similar $|S_{11}|$ performances are accomplished when any of the reservoirs individually is filled with liquid metal. This implies that the designed passive feed network is successful in routing the RF power to the liquid metal patch element. An in-house ray tracing MATLAB code [28] that utilizes the ADS® simulated patterns is employed for computing the far field patterns generated by the extended hemispherical lens. As demonstrated in Figure 3.3(b), moving the liquid metal patch among the reservoirs provides different excitation locations at the back surface of the extended hemispherical lens which in turn provides beam scanning capability. The FPA exhibits a half power beamwidth of 7^0 in both of the ϕ=0^0 and 90^0 elevation planes, implying 29dB directivity according to Krauss' approximation [69]. A $\pm 30^0$ field of view (FoV) is accomplished with individual element patterns overlapping at their half power beamwidths.

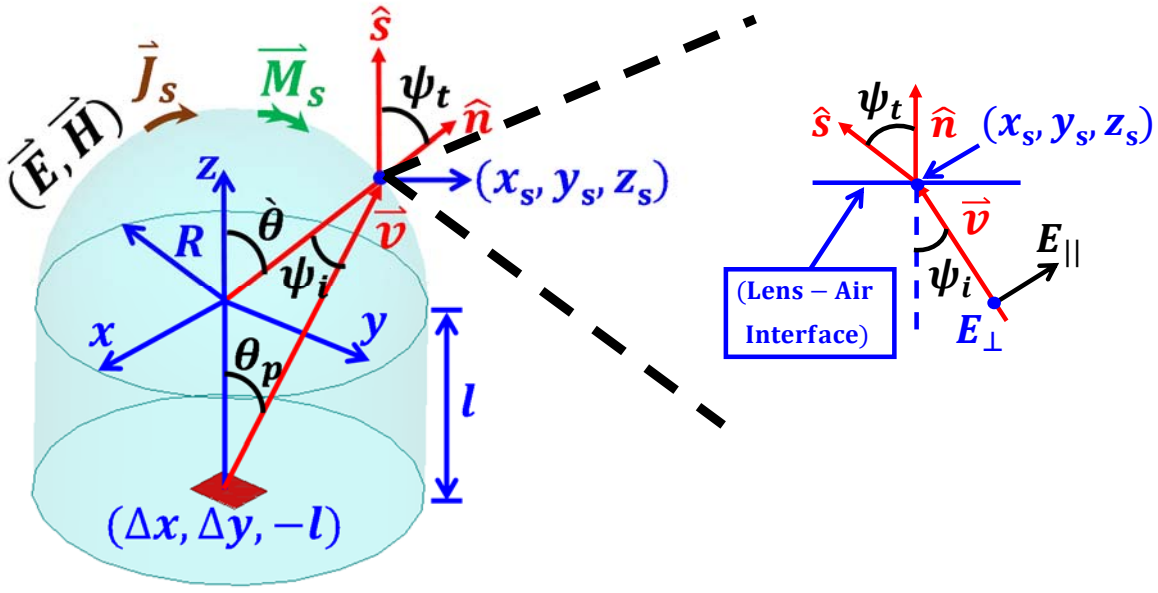

Figure 3.4: The ray diagram along with the lens geometry.

As it was mentioned earlier, the far field radiation patterns radiated by the lens are calculated using a ray tracing code that employs the ADS® simulated radiation pattern of the patch antenna. As shown in Figure 3.4, the patch antenna is located at (Δx, Δy, z = -l) relative to the used coordinate system. In order to calculate the radiated fields in the far-field, it is necessary to know the patch's incident electric $\overrightarrow{E_p}$ at the lens-air interface (i.e., at $r = R, \theta = \grave{\theta},\ \phi = \grave{\phi}$, or $(x, y, z) = (x_s, y_s, z_s)$). It can be written as [70]:

$$\overrightarrow{E_p} = \hat{\theta}_p E_{\theta p}(R, \grave{\theta}, \grave{\phi}) + \hat{\phi}_p E_{\phi p}(R, \grave{\theta}, \grave{\phi}), \tag{3.1}$$

where $E_{\theta p}$ and $E_{\phi p}$ are the patch's radiated electric field in the $\hat{\theta}_p$ and $\hat{\phi}_p$ directions, respectively. $\overrightarrow{E_p}$ is either simulated using ADS® or calculated using the patch cavity model [69]. In addition to $\overrightarrow{E_p}$, the surface normal unit vector ($\hat{n}$) and ray vector ($\vec{v}$) are calculated as [71]:

$$\hat{n} = \hat{r} = \hat{x}\sin\grave{\theta}\cos\grave{\phi} + \hat{y}\sin\grave{\theta}\sin\grave{\phi} + \hat{z}\cos\grave{\theta} \tag{3.2}$$

$$\vec{v} = \hat{x}(x_s - \Delta x) + \hat{y}(y_s - \Delta y) + \hat{z}(z_s - l) = \hat{x}v_x + \hat{y}v_y + \hat{z}v_z \tag{3.3}$$

with its unit vector found as $\hat{v} = \frac{\vec{v}}{|\vec{v}|}$. Since $\vec{v}$ is defined, the patch antenna's location in terms of the spherical coordinates is given as: $\theta_p = \frac{\pi}{2} - \tan^{-1}\left(\frac{v_z}{\sqrt{v_x^2+v_y^2}}\right)$ and $\phi_p = \cos^{-1}\left(\frac{v_x}{\sqrt{v_x^2+v_y^2}}\right)$. At each point over the lens surface, a plane of incidence entirely including the vectors $\bar{v}$ and $\hat{n}$ can be defined. On the plane of incidence, $\overrightarrow{E_p}$ can be decomposed into its parallel and perpendicular polarizations as shown in Figure 3.4. To decompose $\overrightarrow{E_p}$ into its parallel and perpendicular components, polarization unit vectors are first generated as follows [72]:

$$\vec{P}_\perp = \hat{n} \times \hat{v} \tag{3.4}$$

$$\hat{p}_{\perp} = \frac{\vec{P}_{\perp}}{|\vec{P}_{\perp}|} \tag{3.5}$$

$$\vec{p}_{\parallel} = \hat{p}_{\perp} \times \hat{v}. \tag{3.6}$$

Then, the parallel ($E_{\theta p}$) and perpendicular($E_{\phi p}$) components are calculated as:

$$E_{\theta p} = \overrightarrow{E_p} \cdot \hat{p}_{\parallel} \tag{3.7}$$

$$E_{\phi p} = \overrightarrow{E_p} \cdot \hat{p}_{\perp} \tag{3.8}$$

Since both of the components are known, the component of the electric field outside $\left(\vec{E} = \hat{x}E_x + \hat{y}E_y + \hat{z}E_z\right)$ the lens can be given as [72]:

$$E_x = \left(E_{\phi p}\right)\tau_{\perp}(\hat{x} \cdot \hat{p}_{\perp}) + \left(E_{\theta p}\right)\tau_{\parallel}[(\hat{x} \cdot \hat{p}_{\parallel})\cos(\psi_t - \psi_i) - (\hat{x} \cdot \hat{v})\sin(\psi_t - \psi_i)] \tag{3.9}$$

$$E_y = \left(E_{\phi p}\right)\tau_{\perp}(\hat{y} \cdot \hat{p}_{\perp}) + \left(E_{\theta p}\right)\tau_{\parallel}[(\hat{y} \cdot \hat{p}_{\parallel})\cos(\psi_t - \psi_i) - (\hat{y} \cdot \hat{v})\sin(\psi_t - \psi_i)] \tag{3.10}$$

$$E_z = \left(E_{\phi p}\right)\tau_{\perp}(\hat{z} \cdot \hat{p}_{\perp}) + \left(E_{\theta p}\right)\tau_{\parallel}[(\hat{z} \cdot \hat{p}_{\parallel})\cos(\psi_t - \psi_i) - (\hat{z} \cdot \hat{v})\sin(\psi_t - \psi_i)] \tag{3.11}$$

where ($\tau_{\parallel}$) and ($\tau_{\perp}$) are, respectively, the Fresnel's parallel and perpendicular transmission coefficients that are given by [73]:

$$\tau_{\parallel} = \frac{2\sqrt{\varepsilon_r}cos\psi_i}{\varepsilon_r cos\psi_i + \sqrt{\varepsilon_r - (\sin\psi_i)^2}} \tag{3.12}$$

$$\tau_{\perp} = \frac{2cos\psi_i}{cos\psi_i + \sqrt{\varepsilon_r - (\sin\psi_i)^2}}. \tag{3.13}$$

In (3.9) - (3.13), ε_r, ψ_i, ψ_t are the dielectric constant of the lens, angles of incidence and transmission, respectively. The incident angle, ψ_i, can be calculated as $\psi_i = \cos^{-1}(\hat{n}.\hat{v})$, and thus, ψ_t is found using the Snell's law as $\psi_t = \sin^{-1}(\sqrt{\varepsilon_r}\sin\psi_i)$.

Having $(\vec{E})$ calculated, the magnetic field outside the lens $(\vec{H})$ is given as $\vec{H} = \frac{1}{120\pi}(\hat{s} \times \vec{E})$, where $\hat{s}$ is the ray unit vector outside the lens and its components are given by [72]:

$$s_x = v_x \cos(\psi_t - \psi_i) + (\hat{x} \cdot \hat{p}_{\parallel}) \sin(\psi_t - \psi_i) \tag{3.14}$$

$$s_y = v_y \cos(\psi_t - \psi_i) + (\hat{y} \cdot \hat{p}_{\parallel}) \sin(\psi_t - \psi_i) \tag{3.15}$$

$$s_z = v_z \cos(\psi_t - \psi_i) + (\hat{z} \cdot \hat{p}_{\parallel}) \sin(\psi_t - \psi_i). \tag{3.16}$$

Once $(\vec{E})$ and $(\vec{H})$ are obtained just outside the lens's surface, the equivalent surface electric $(\vec{J}_s)$ and magnetic $(\vec{M}_s)$ current densities on the lens's surface can be calculated using the Huygens's principle [71]:

$$\vec{J}_s = \hat{n} \times \vec{H} \tag{3.17}$$

$$\vec{M}_s = -\hat{n} \times \vec{E}. \tag{3.18}$$

Hence, the electric field at the far-field radiated by the lens's aperture is found by using the far-field radiation integrals [71]:

$$E_\theta = -\frac{jke^{-jkr}}{4\pi r}(L_\phi + \eta_0 N_\theta) \tag{3.19}$$

$$E_\phi = \frac{jke^{-jkr}}{4\pi r}(L_\theta - \eta_0 N_\phi), \tag{3.20}$$

and the radiation integrals are defined as [71]:

$$N = \iint_S J_s e^{jkr'cos\psi}\, ds' \tag{3.21}$$

$$L = \iint_S M_s e^{jkr'cos\psi}\, ds', \tag{3.22}$$

where k is the propagation constant, S is the hemispherical surface, η_0 is the free space intrinsic impedance and equals to $120\pi\ \Omega$, r is the distance to the observation point measured the origin of the coordinate system, r' is the distance to the current sources from the origin of the coordinate system, ψ is the angle between r and r', and $ds' = R^2 \sin\theta'\, d\theta' d\phi'$.

3.3. FPA Radiation and Switching Performance

It is important to note that the resonant nature of the utilized passive feed mechanism will result in performance degradation due to radiation leakage as realization of perfect open circuit stub terminations is not practically possible. In addition, a long microstrip line was used to feed the antenna from the side of the lens (see Figure 3.7(a)) which increases the network loss. Therefore, to quantify the loss associated with the feed network, computational studies were performed by comparing radiation pattern performance of the microfluidic based FPA to that of a stand-alone patch antenna excitation (i.e. without any feed line) located at the lens back surface. Figure 3.5(a)-(d) presents these radiation pattern comparisons for all FPA elements. It is observed that the feed network loss accounts for 4.06 dB, 3.88 dB, 3.90 dB, and 3.82 dB reductions in realized gain for the patch antenna locations #1, #2, #3, and #4, respectively. The average feed network loss is therefore 3.92 dB. This is comparable to the performance of a conventional 8 element FPA implementation that would utilize a total of 7 SP2T switches and activate a patch element through the series connection of 3 SP2T switches. Commercially available Ka-band SP2T switches [74] exhibit ~1 dB insertion loss and the conventional feed network will potentially

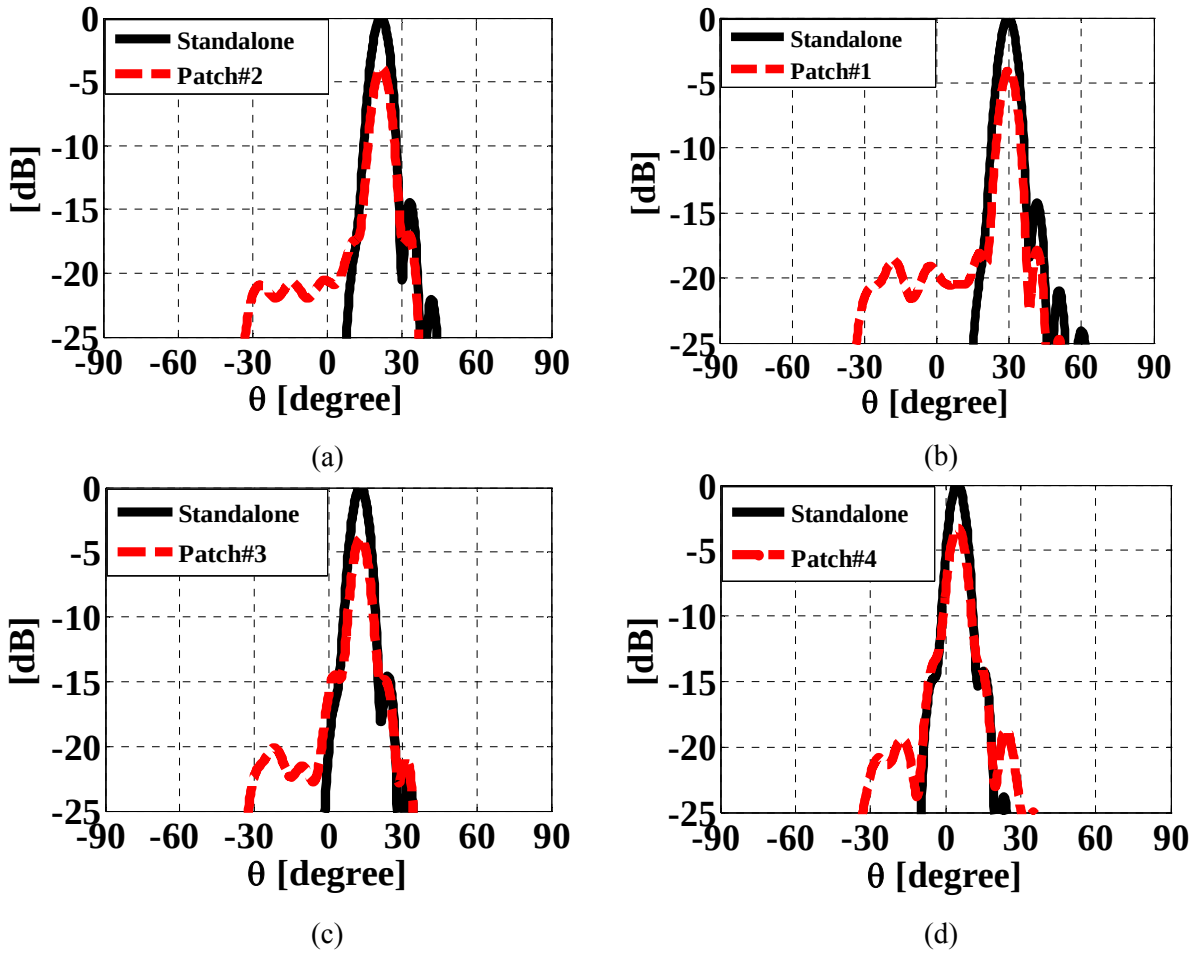

Figure 3.5: Microfluidic FPA pattern comparisons with a standalone patch located behind the lens at the position of a) #1, b) #2, c) #3, and d) #4.

exhibit >3 dB insertion loss due to the additional interconnects, microstrip line sections, and bends. The radiation patterns presented in Figure 3.5 reveals an enlargement in the sidelobe level for the microfluidic based beam scanning array within the $\pm 30^0$ scan range due to the feed network radiation. Specifically, the sidelobe level due to feed network radiation is relatively constant in the scan range and 15 dB below the main beam. In addition to the radiation performance, the array beam scanning time was characterized using mp6 piezoelectric micropumps and mp-x controlling unit acquired from Bartels™ as shown in Figure 3.6(a). Two micropumps are cascaded in series to form a bi-directional pumping unit. These pumps were able to move the liquid metal patch to the

adjacent reservoir in 70msec as depicted in Figure 3.6(b). The switching time can be potentially reduced down to a few msec using mechanically faster pumps.

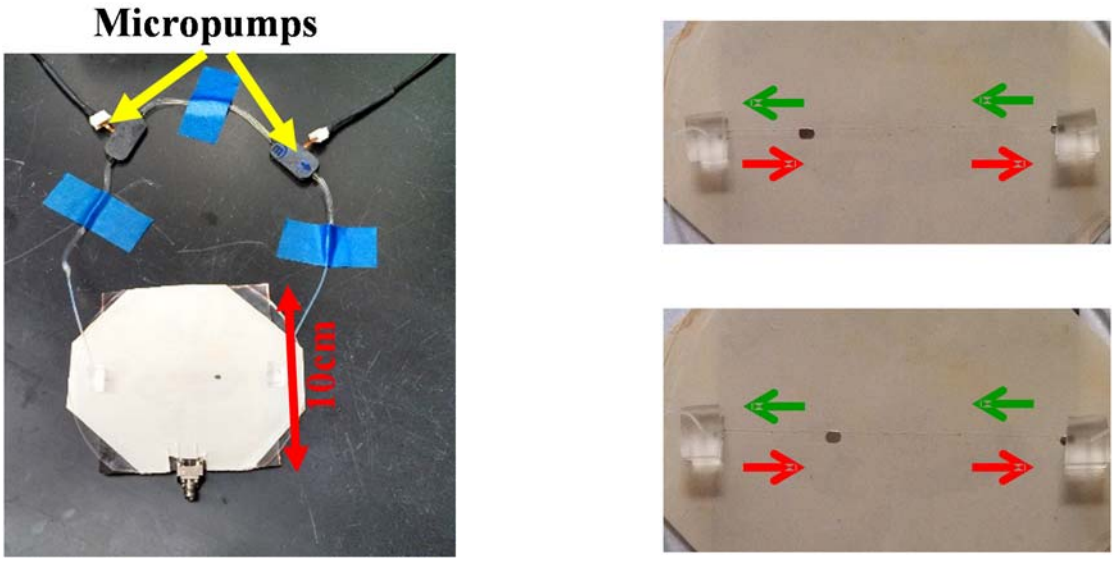

(a) (b)

Figure 3.6: a) Switching speed test setup, and b) snapshots of the liquid metal antenna moving among two adjacent reservoirs.

3.4. Microchannels Fabrication

The microfluidic channels were fabricated using the PDMS micromolding technique. To obtain the mold layer, negative photoresist (SU-8 2075) was spun onto a silicon wafer and then patterned with a UV light source. The PDMS oligomer and crosslinking prepolymer of the PDMS agent from a Sylgard™ 184 kit (Dow Corning) was mixed in a weight ratio of 10:1, poured onto the SU-8 mold, and then cured at room temperature for 24 hours to prevent PDMS shrinking due to heat [75]. Bonding the channels to a 50 μm LCP was accomplished by using APTES (3-Aminopropyltriethoxysilane) functionalized SU-8 as an intermediate layer between the PDMS and LCP layers [76]. SU-8 was spun on 50 μm thick LCP substrate and soft baked subsequently. The baked photoresist was then exposed to UV and post baked again. After developing, the SU-8 was

hard baked. The surface of the SU-8 coated LCP substrate was then activated by oxygen plasma treatment. Later, the substrate was placed in a 1%v/v APTES solution heated to 800 C for 20 mins. Subsequently, the functionalized SU-8 and the fabricated PDMS micro channel mold were exposed to oxygen plasma. The two surfaces were placed in conformal contact for 1 hr. After this process, the two surfaces were irreversibly bonded to each other due to the formation of a strong Si-O-Si covalent bond [77].

3.4. Measured Performance

Figure 3.7(a) depicts the lithographically fabricated array feed network. In order to obtain a robust structure, the machined lens was placed in custom built Styrofoam holder as shown in

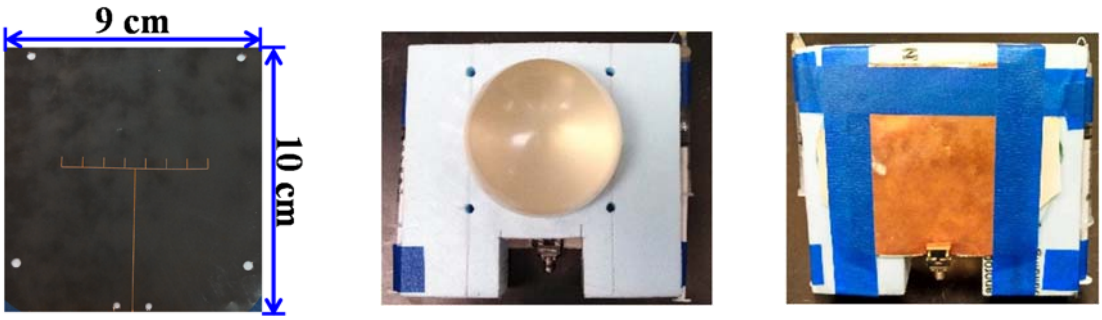

(a) (b) (c)

Figure 3.7: a) Fabricated feed network, b) front view of the measured prototype, and c) back view.

Figure 3.7(b). The feed network and channels were then flushed to its bottom surface using tape as depicted in Figure 3.7(c). For measurement ease within the anechoic chamber, syringes were used to move the liquid metal antenna. This is due to the bulky Bartels controller unit that would hinder the pattern measurements. The array $|S_{11}|$ shown in Figure 3.8(a) was measured using an Agilent N5227A PNA. The array exhibited a matched impedance response at 30 GHz when reservoirs #1 to #4 were individually hosting the liquid metal patch. The beam scanning capability of the array was verified by measuring its realized gain patterns in the $\phi=0^0$ elevation plane. As

shown in Figure 3.8(b), the array scanned the beam as the liquid metal antenna was moved among the reservoirs. Table 3.1 summarizes the expected and measured scan angles and measured maximum gain. As it can be inferred from the table, the measured and expected scan angles are in a very good agreement. The small discrepancy is due to the possible misalignment while installing the array at the lens backside. A maximum realized gain of 24.8 dB was measured when the liquid metal antenna was in reservoir #3, whereas the lowest was 21.5dB when it was in reservoir #1. In average, the array exhibited 5.7dB loss relative to the calculated 29 dB directivity. The measured

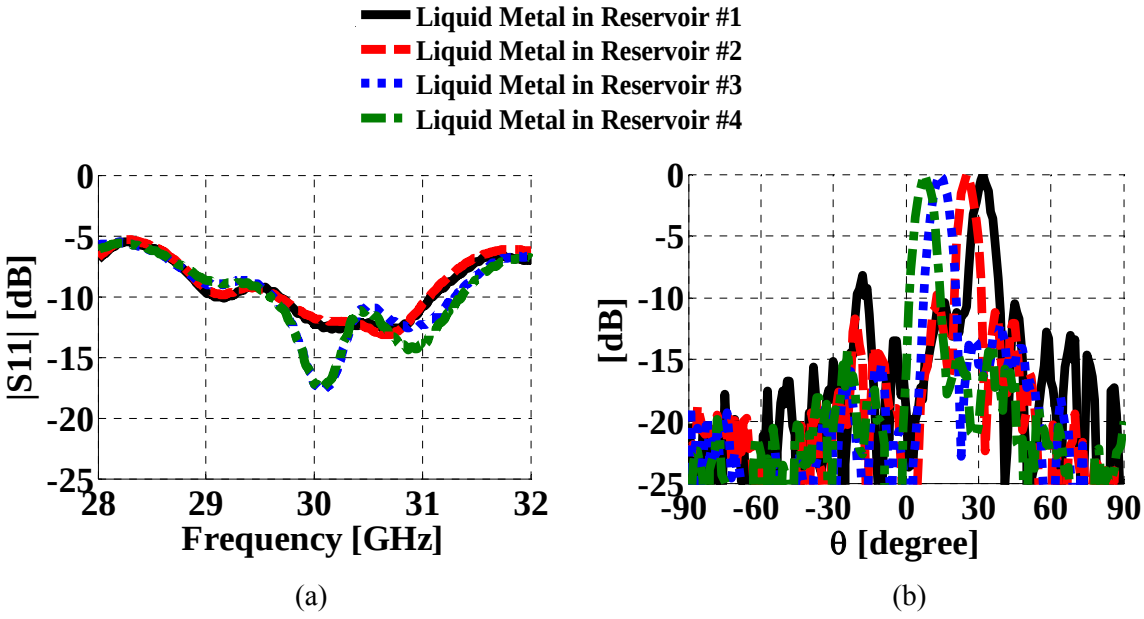

Figure 3.8: Measured performance: a) $|S_{11}|$ and b) normalized gain patterns.

Table 3.1: The array's measured and simulated beam scanning and gain performances

Antenna in Reservoir:	**#1**	**#2**	**#3**	**#4**
Scan Angle (Measured, Calculated)	$(32^0,30^0)$	$(25^0,22^0)$	$(14^0,13^0)$	$(7^0,4^0)$
Measured Gain [dB]	21.5	23.2	24.8	23.9

loss values were comparable to the simulated 3.9 dB feed network loss reported in Section II. The additional 1.8 dB loss was identified to be due to the connector loss and lens-air interface reflection [16].

3.5. Concluding Remarks

A novel microfluidic based 1D FPA capable of providing beam scanning based on microfluidic principles was presented. Specifically, the array included 8 microfluidic reservoirs that are interconnected with microchannels. A liquid metal volume embedded inside dielectric solution was used to construct the antenna element and was moved to different physical reservoir locations to provide beam scanning. The antenna element was a proximity coupled patch antenna. A strategic switch-free feed network was developed to route the input power to the liquid metal filled reservoir without causing impedance mismatches. The impedance matching and realized gain performances of the array were computationally demonstrated and experimentally verified. The array operated with a peak realized gain of 24.8 dB and provided $\pm 30^0$ scan range in the elevation plane using a dielectric extended hemispherical lens. This is comparable to a switch based FPA. Hence, the proposed array is promising for low cost implementation. It should be noted that the presented FPA can be employed with different type of lenses to provide an overall lower profile. New feed network designs should be investigated to reduce the radiation loss and possibly obtain continuous beam scanning. In addition, different types of commercially available micropumps are being investigated for faster beam scanning capabilities.

CHAPTER 4: PASSIVE FEED NETWORK DESIGNS FOR MFPAs AND THEIR PERFORMANCE EVALUATION

4.1. Introduction

The emergent need for large capacity and high data rate communication links demands using highly directive antenna arrays with beam-scanning functionality [78, 79]. These capabilities can be obtained using different technologies such as phased arrays [15, 21, 64, 66, 80-83], focal plane arrays (FPAs) [16, 84, 85] and reflectarray antennas [17, 86-90]. At the mm-wave band, however, phased arrays and FPAs remarkably suffer from high cost and loss due to the extensive hardware integrated in their feed networks. Likewise, reflectarrays require bulky components to perform mechanical beam scanning.

To achieve beam-scanning capability with significant RF and mechanical hardware reduction, our group has recently introduced a 1D microfluidic based focal plane array (MFPA) [91] that was discussed in the previous chapter. Specifically, a high-gain 30GHz beam has been scanned in elevation plane by re-positioning a liquid metal patch antenna element inside a microfluidic channel located at the focal plane of an extended hemispherical dielectric lens. The MFPA employed a resonant corporate microstrip line feed network that was strategically designed to be all-passive. The movement of the patch element along the microfluidic channel was performed sequentially by using a bi-directional micropump unit. Consequently, beam-scanning was accomplished with a compact and cost effective system without resorting to active RF devices.

Microfluidic based reconfigurability has been recently proposed to implement a variety of RF devices to achieve superior performances in terms of high power handling, wideband frequency

tuning range, and low cost. For example, continuously movable liquid metal slugs formed inside microfluidic tubes or channels have been utilized to realize wideband tunable frequency selective surfaces (FSS), bandpass filters [26, 58], and monopole antennas [92]. A movable liquid metal slug formed inside a microfluidic tube has been used as a parasitic reflector to steer the radiation pattern of a loop antenna [59]. Stretchability of the polymers hosting the liquid metal filled microfluidic channels have been used for demonstrating tunable dipole [93] and patch [94] antennas. Stretchability has also been proposed to implement flexible antennas and sensors [25, 95-97].

The MFPA introduced in chapter II [91] is the first-time that the microfluidic based reconfigurability has been used to implement high-gain beam-scanning. However, chapter II has not provided design details of the utilized passive feed network, analyzed its bandwidth/loss performance and addressed the high side lobe level (SLL) issue occurring due to the radiation leakage. This chapter considers the design details and performance evaluation of different passive network layouts that can potentially be utilized to excite MFPAs. Specifically, in Sections II and III, resonant corporate, resonant straight, and non-resonant straight microstrip line feed networks are introduced and their bandwidth/loss performances are investigated using transmission line theory. The MFPA performance when using the introduced feed networks is evaluated in terms of radiation pattern, loss and bandwidth by making use of an in-house ray tracing code [28]. It is shown that the straight networks reduce the SLL by 10 dB relative to the corporate network. The resonant network fed MFPA is shown to exhibit similar bandwidth performance for increasing array size whether the feed network layout is straight or corporate. On the other hand, the non-resonant network offers the bandwidth performance independent of the of the array size. To validate the SLL and bandwidth analysis, in Section IV, an 8 element straight resonant network

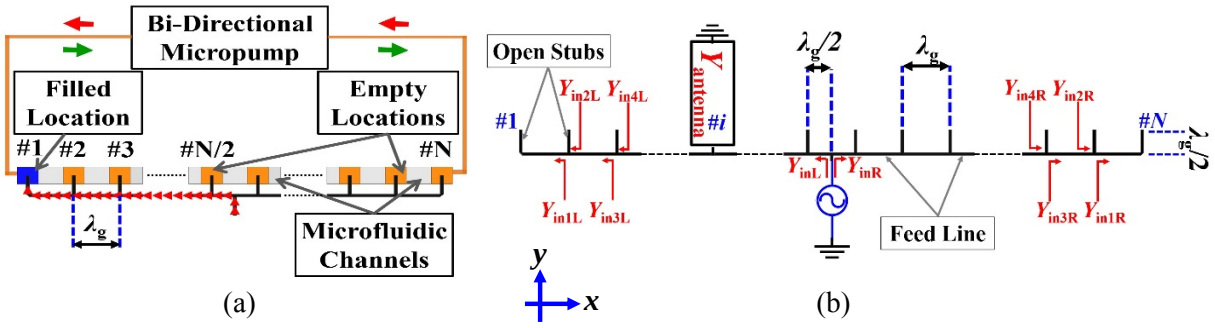

Figure 4.1: a) The generic layout of a 1D MFPA excited with a resonant corporate microstrip line feed network. The array consists of a microfluidic channel located at the focal plane of a microwave lens and hosts N locations to generate N beams. The antenna element is sequentially moved among these locations using a micropump, and b) equivalent circuit of the feed network when the antenna element is in location #*i*.

fed MFPA is fabricated and tested. The measured $\pm 25^0$ field of view (FoV), 23.5 dB realized gain performance and 4% $|S_{11}|$<-10 dB bandwidth agree well with the expectations from theoretical and numerical analysis. Additionally, different than the previous chapter's work that relied on liquid metal, the antenna element of the MFPA is implemented from a metalized plate by carrying out flow characterizations on various microfluidic channel geometries. This metalized plate approach paves the way for reliable and non-toxic liquid-metal-free microfluidic reconfigurable devices with higher efficiency and power handling capabilities.

4.2. Resonant Feed Networks for MFPAs

4.2.1. Corporate Feed Network

The general layout for a 1D MFPA excited with a corporate microstrip line feed network is depicted in Figure 4.1(a). It consists of a microfluidic channel placed at the focal plane of a microwave lens for beam scanning. It is important to mention that although the presented work uses an extended hemispherical dielectric lens [27], different types of lenses such as Fresnel lenses [98] and frequency selective surface based synthesized lenses [99-101] can be utilized by the proposed MFPA layout without loss of generality. As shown in Figure 4.1(a), the microfluidic

channel hosts an even number (N) of locations to generate a total of N beams in elevation plane. The patch antenna element inside the microfluidic channel is sequentially moved among the locations by using a bi-directional micropump unit. At any location, the excitation of the patch antenna is achieved by the microstrip line stubs either by a proximity or aperture coupling mechanism. Each stub is designed to be $\lambda_g/2$ in length where λ_g denotes the guided wavelength at the design frequency f_0. This ensures that all the stubs that are open circuit (OC) terminated without the loading of the antenna element will also exhibit OC conditions at the junctions where they are connected to the main microstrip feed line. In addition, the N antenna locations are designed to be λ_g apart to carry the OC conditions at the stub junctions along the main microstrip line. This feed network layout clearly operates based on the resonance of $\lambda_g/2$ stubs and ideally allows the RF input power to be totally delivered to the antenna by forcing the OC condition at the microstrip line junctions. However, in a practical realization, the unloaded stubs exhibit a finite quality factor (Q_{stub}) that results in power loss and radiation leakage increasing with N. Moreover, the impedance matching bandwidth also becomes dependent on N due to the resonance mechanism.

To evaluate the $|S_{11}|$<-10 dB bandwidth performance, the feed network is analyzed by making use of the transmission line theory. Figure 4.1(b) depicts the equivalent circuit of the feed network when the antenna element is in location #i. The antenna element loaded stub is modeled with the input admittance seen from its end $Y_{antenna}$. If i=1, then input admittance Y_{in1L} is given as [47]:

$$Y_{in1L} = Y_0 \frac{Y_{antenna} + Y_0 \tanh(\alpha\lambda_g + j\beta\lambda_g)}{Y_o + Y_{antenna} \tanh(\alpha\lambda_g + j\beta\lambda_g)}, \tag{4.1}$$

otherwise:

$$Y_{in1L} = Y_0 \frac{Y_{stub} + Y_0 \tanh(\alpha\lambda_g + j\beta\lambda_g)}{Y_o + Y_{stub} \tanh(\alpha\lambda_g + j\beta\lambda_g)}, \tag{4.2}$$

$$Y_{stub} = Y_0 \tanh[0.5(\alpha\lambda_g + j\,\beta\lambda_g)], \tag{4.3}$$

where Y_0, β, and α denote the transmission line's characteristic admittance, propagation constant, and attenuation constant, respectively. The input admittance seen by the source towards the left (i.e. Y_{inL} in Figure 4.1(b)) is evaluated by updating the admittance value at each stub junction according to the below algorithm (assuming the antenna is at one of the locations in the left half of the feed network):

for k= 2: N-1

if $k = 2\times(i\text{-}1)$:

$$Y_{inL(k)} = Y_{inL(k-1)} + Y_{antenna} \tag{4.4}$$

else if modulus (k,2) = 0

$$Y_{inL(k)} = Y_{inL(k-1)} + Y_{stub} \tag{4.5}$$

else if $k = N$-1

$$Y_{inL} = Y_{inL(k)} = Y_0 \frac{Y_{inL(k-1)} + Y_0 \tanh[0.5(\alpha\lambda_g + j\beta\lambda_g)]}{Y_0 + Y_{inL(k-1)} \tanh[0.5(\alpha\lambda_g + j\beta\lambda_g)]} \tag{4.6}$$

else

$$Y_{inL(k)} = Y_0 \frac{Y_{inL(k-1)} + Y_0 \tanh[(\alpha\lambda_g + j\beta\lambda_g)]}{Y_0 + Y_{inL(k-1)} \tanh[(\alpha\lambda_g + j\beta\lambda_g)]}. \tag{4.7}$$

end

end

Since the feed network is symmetric, the above algorithm can also be used to evaluate the input admittance seen by the source towards the right side (i.e. Y_{inR} in Figure 4.1(b)). For this, the subscript L in equations (1) to (7) should be replaced with subscript R. Moreover, equation (4)

should be ignored and only (5)-(7) are used. If the antenna is located on the right hand side of the network (i.e. $i > N/2$), the index i holding the antenna location in the algorithm should be updated as $i = (N+1-i)$ and equation (4) should not be used when evaluating Y_{inL}. Once Y_{inL} and Y_{inR} are evaluated, the S_{11} is calculated as:

$$S_{11} = \frac{Y_0 - Y_{in}}{Y_0 + Y_{in}} = \frac{Y_0 - (Y_{inL} + Y_{inR})}{Y_0 + (Y_{inL} + Y_{inR})}. \quad (4.8)$$

The outlined analysis does not include the discontinuity effects of the transmission line junctions. However, it provides a rigorous estimation for the S_{11} response of a MFPA excited by a corporate feed network as it accounts for the losses and the frequency dependent nature of the antenna admittance. Therefore, as will be shown in the following, the provided analysis conveniently estimates the bandwidth performance for arbitrary N and agrees well with the simulated $|S_{11}|$ responses.

4.2.2. Performance of Corporate Fed MFPA

Throughout this chapter, an MFPA operating behind an extended hemispherical dielectric lens (Rexolite, (ε_r=2.56, tanδ=0.0026)) at 30 GHz is considered for numerical examples and experimental verification [27]. The feed network is based on a microstrip line layout designed on a 200 μm thick RO4003C material (ε_r=3.55, tan(δ)=0.0027) [102]. A 100 μm Liquid Crystal Polymer (LCP) layer (ε_r=2.9, tan(δ)=0.0025) [103] is used to separate the microfluidic channels carrying the proximity coupled patch antenna element from the feed network. The microfluidic channels are formed inside a 2 mm thick Polydimethylsiloxane (PDMS) (ε_r=2.8, tan(δ)=0.02) [104] and sealed by bonding to the LCP layer. Due to the electrically large nature of the dielectric lens, a semi-infinite layer of Rexolite is used to model the presence of the lens [67, 68]. Agilent Advanced Design System (ADS) Momentum and Schematic suites are used for the simulation purposes [105].

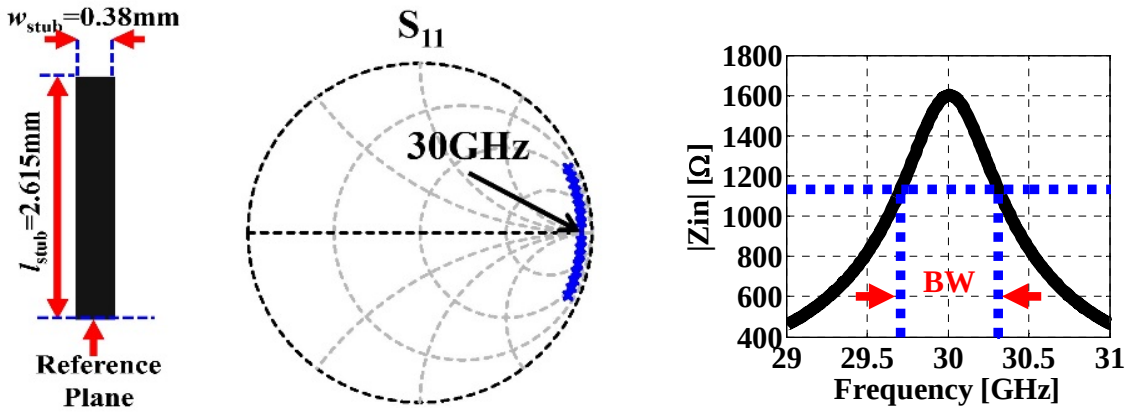

(a) (b) (c)

Figure 4.2: a) a $\lambda_g/2$ resonator, b) simulated S_{11} on the Smith chart, and c) simulated absolute input impedance of the $\lambda_g/2$ resonator.

The synthesis of the corporate feed network begins with the design of a Z_0=50 Ω $\lambda_g/2$ long microstrip line open circuit resonator at f_0=30 GHz. Figure 4.2(a) depicts the resonator that is 2.615 mm long (l_{stub}) and 0.38 mm wide (w_{stub}). In order to determine the stub's width, a transmission line terminated with two 50 Ω ports was simulated. The initial width was calculated assuming only the presence of the RO4003C [47]. Later, the width was reduced until the reflection coefficient of the simulated transmission line was < -40 dB. On the other hand, the stub's length was found by simulating a one port transmission line and varying its length until the resonance condition was obtained. Thereby, β was calculated as $\beta = \pi/l_{stub}$. The simulated S_{11} performance on the Smith chart of the open stub resonator reveals a resonance at 30 GHz as shown in Figure 4.2(b). The bandwidth of the stub is calculated from its extracted absolute input impedance shown in Figure 4.2(c) [47]. Specifically, the bandwidth is 0.6 GHz and results in $Q_{stub} = f_0/BW = 50$[47]. From this, the attenuation constant is calculated as $\alpha = \beta/2Q_{stub}$.

The next step in the synthesis of the feed network is to design the 30 GHz patch antenna element. As shown in Figure 4.3(a), the antenna is excited by the designed $\lambda_g/2$ long microstrip stub using proximity coupling. The antenna exhibits 7 dB gain and 6% $|S_{11}|$<-10 dB bandwidth. To utilize the frequency dependent admittance of the antenna in transmission line theory based

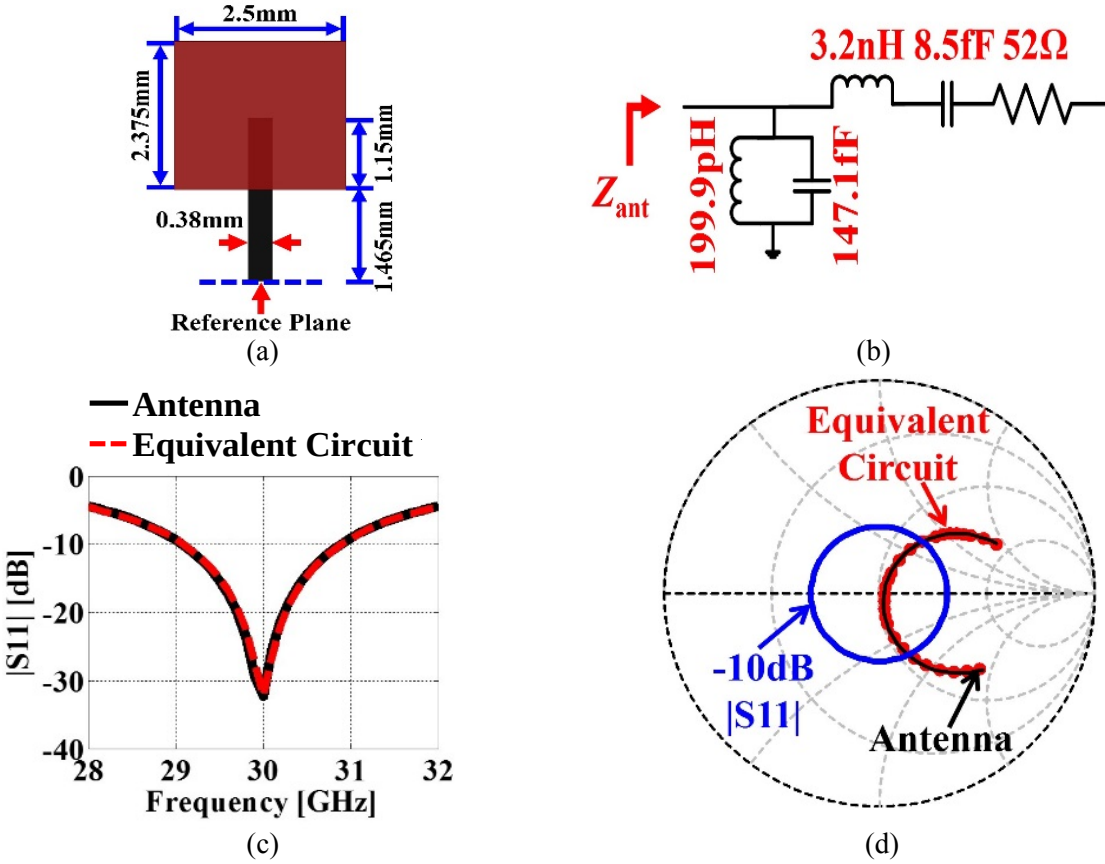

Figure 4.3: a) Layout of the proximity coupled patch antenna. It is designed at 30 GHz. b) extracted equivalent lumped element circuit model of the antenna; c) comparison of the $|S_{11}|$ obtained from full wave and equivalent circuit simulations, and d) frequency dependence of the S_{11} on the Smith chart.

calculations, an equivalent lumped element circuit is extracted [106] as shown in Figure 4.3(b). The S_{11} response of the equivalent lumped element circuit agrees well with that of the antenna as shown in Figure 4.3(c)-(d).

Once the antenna admittance (Y_{ant}), λ_g, α, and β are known, the transmission line theory based algorithm detailed in the previous section can be utilized to estimate the array bandwidth for

a desired *N*. Figure 4.4(a) shows the variation of the array bandwidth with *N* when the antenna is at location #1 and #*N*/2. It is observed that the bandwidth decreases with increasing *N* for either antenna locations. However, the bandwidth is limited by the antenna positioned at location #*N*/2. For instance, the array exhibits 2.7% and 0.7% bandwidths for *N*=8 and *N*=16, respectively. Figure 4.4(b) shows the $|S_{11}|$ for *N*=4, 8 and 16 when the antenna occupies the location #*N*/2. The bandwidth reduction with increasing *N* is evident and coupled with impedance matching

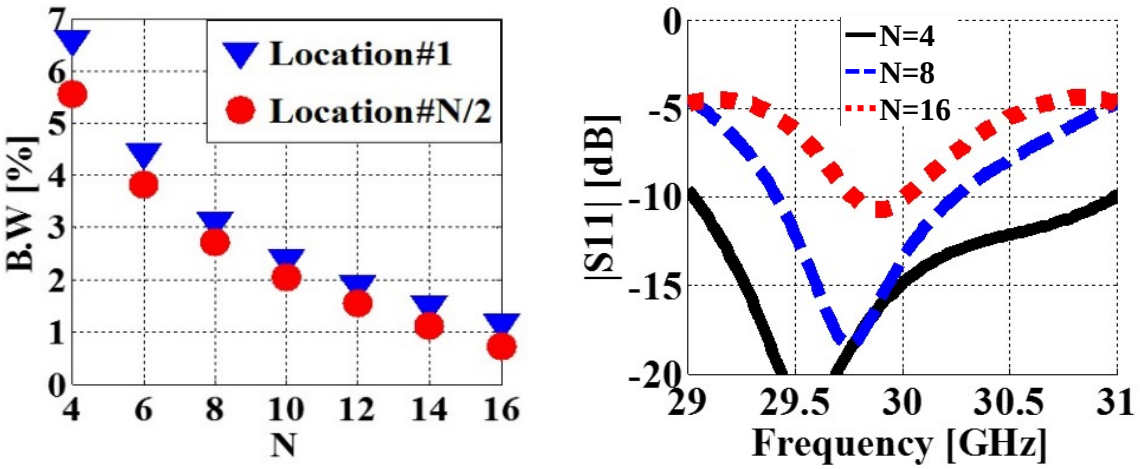

(a) (b)

Figure 4.4: a) The bandwidth performance of the resonant corporate feed network excited MFPA as a function of *N* when the location #1 and #*N*/2. The bandwidth decrease with *N*, and b) the array $|S_{11}|$ for different N values when the antenna is at location #*N*/2.

deterioration due to increasing loading effect of the finite *Q* open stubs. To verify the transmission line theory based results and investigate the radiation performance, an *N*=8 element MFPA was subsequently designed by using ADS Momentum. The synthesis of the feed network started with connecting a λ_g long (i.e. 2×2.615 = 5.23 mm) microstrip line to the open stub resonator (see Figure 4.5(a)). Subsequently, the second stub was added and another λ_g long microstrip line was connected as depicted in Figure 4.5(b). This procedure was repeated twice more to generate the circuits shown in Figure 4.6(c) and (d). Note that different than the others, the circuit shown in

Figure 4.5(d) was connected to a $\lambda_g/2$ long microstrip line. Finally, the circuit in Figure 4.5(e) was formed by combining the circuit in Figure 4.5(d) with its mirrored image with respect to the indicated reference plane. Figure 4.5(f) demonstrates the simulated S_{11} performances of the circuits in Figure 4.5(a) to (e) on the Smith chart without any antenna element loading. Each S_{11} curve intersects with the positive real axis of the S_{11} plane at 30 GHz as expected from the resonant nature

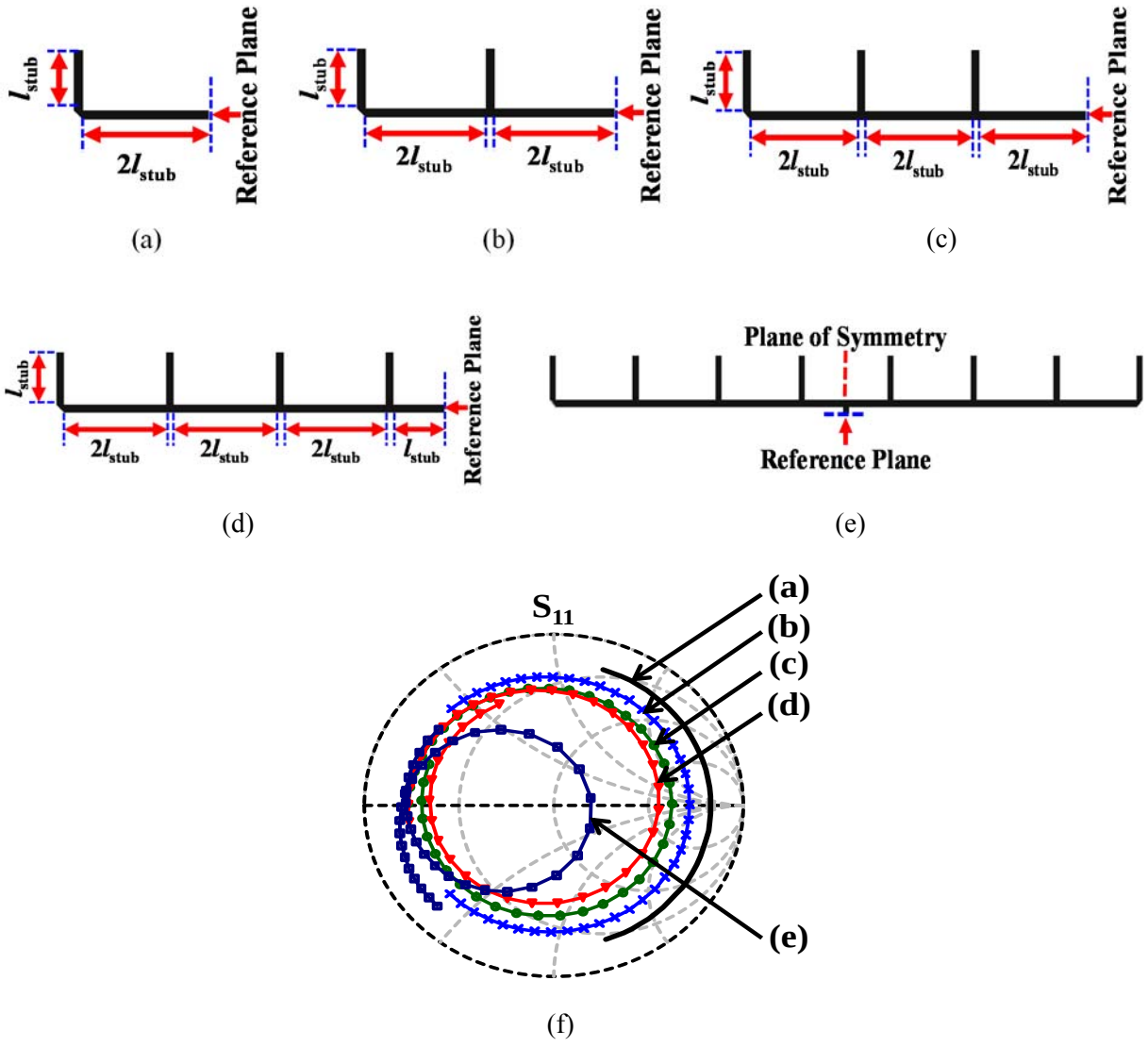

Figure 4.5: Design procedure of a resonant corporate feed network consisting for 8 element MFPA. a) single stub connected to a λ_g microstrip line, b) two stubs, c) three stubs, d) four stubs, e) completed feed network constructed by having the design in (d) mirrored around the symmetry plane, and f) simulated S_{11} curves on the Smith chart. All curves intersect with the positive real axis of the S_{11} plane at 30 GHz.

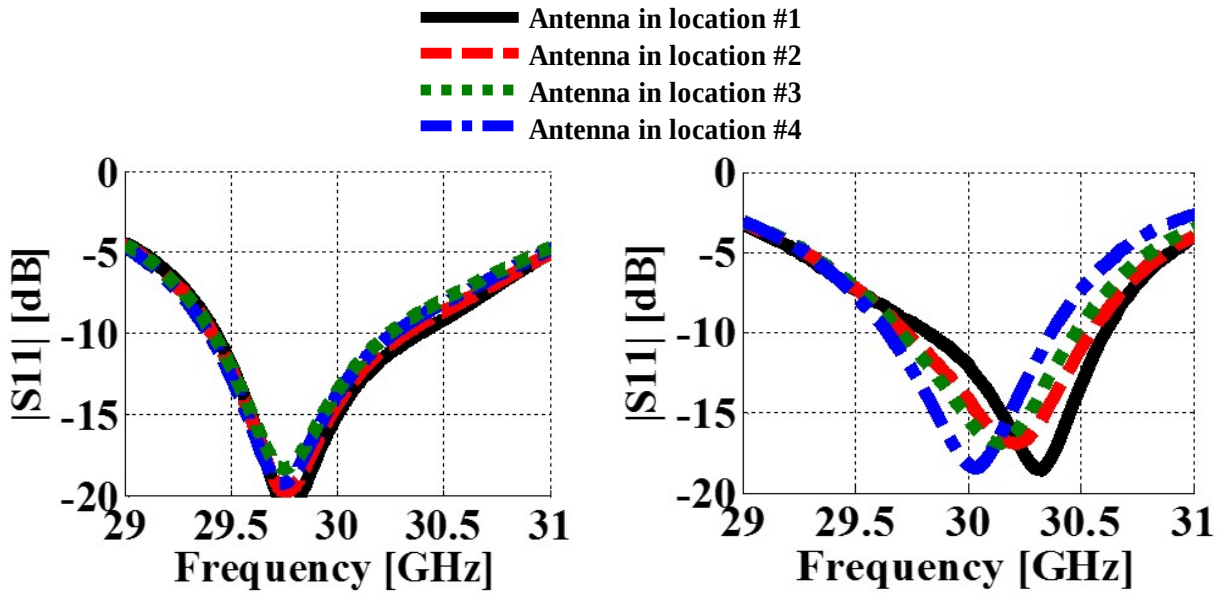

Figure 4.6: The $|S_{11}|$ performance of the 8 element MFPA excited by the resonant corporate feed network. The antenna is moved among locations #1-#4: a) transmission line theory and b) full wave simulation.

of the circuit layout. However, the intersection point gradually moves toward the center of the Smith chart as more stubs are added. This demonstrates that the finite quality factor of the stubs generates a resistive loading mechanism that is associated with attenuation and radiation leakage based losses. Figure 4.6(a) shows the calculated $|S_{11}|$ of the MFPA using the transmission line theory when the antenna is positioned at locations #1, #2, #3, and #4. Due to the symmetry of the feed network, the MFPA performance is investigated only for the cases when the patch antenna element is positioned at these locations. It is observed that the feed network enables a good $|S_{11}|$<-15 dB impedance match at 30GHz regardless of the antenna location. $|S_{11}|$ performances obtained from full wave simulations are shown in see Figure 4.6(b). The transmission line theory analysis and the full wave simulations agree very well on the 2.6% $|S_{11}|$<-10 dB bandwidth. The slight mismatch between the resonance frequencies of the two methods can be attributed to the unaccounted microstrip bends and T-junctions in the transmission line theory analysis.

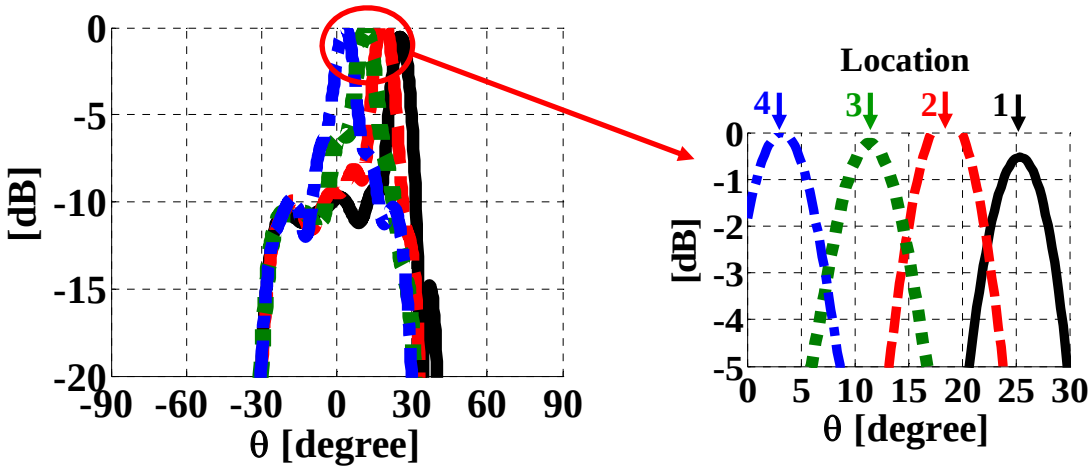

Figure 4.7: The radiation pattern of the 8 element MFPA excited by the resonant corporate feed network. The antenna is moved among locations #1-#4.

The radiation pattern of the MFPA was calculated by numerically integrating the radiation from equivalent currents on the surface of the hemispherical lens. The hemispherical lens had 4 cm radius and 4.32 cm extension length based on the design equations presented in [27]. The equivalent currents were evaluated using ray tracing and the fields radiated into the semi-infinite Rexolite layer (numerically evaluated by the ADS Momentum) were utilized as incident fields at the lens-air interface [28]. Figure 4.7 shows the normalized radiation patterns of the MFPA in the *x-z* elevation plane. Specifically, the beams generated by the patch antenna element at locations #1 to #4 all exhibit 7^0 half power beam width (HPBW) corresponding to 29 dB directivity based on Krauss' approximation [69]. Due to the λ_g separation between the antenna locations, the beams overlap with each other 3 dB below the maximum directivity. Utilization of 8 elements provides a $\pm 25^0$ field of view (FoV). The major drawback of the MFPA is associated with the high level of SLL that is 10 dB below the peak directivity. Similar high SLL was also observed at the *y-z* elevation plane. As seen in Figure 4.7, the SLL is uniformly distributed throughout the $\pm 25^0$ FoV

and therefore implies a radiation leakage associated with the open circuited stubs of the corporate feed network [107].

To evaluate the realized gain, the power delivered to the patch antenna element is calculated by carrying out a full wave simulation of the feed network shown in Figure 4.5(e) with each stub removed and replaced by a 50 Ω port. This results in N+1 ports, where the first port is located at the reference plane, second port at the first open stub position and so on. Next, the simulated circuit is imported to ADS Schematic as a component that exhibits 9 ports. The first port representing the reference plane is connected to a 50 Ω port termination, whereas a second termination exhibiting the complex characteristics impedance of Z_{ant} is connected to a second node representing the antenna location. The remaining nodes are all individually connected to a data box that contains the S_{11} data of the open stub resonator. Under these conditions, the simulated $|S_{21}|^2$ represents the power delivered to the antenna relative to the input power at the reference plane. As shown in Figure 4.8, for the N=8 element corporate fed MFPA, the maximum $|S_{21}|^2$ at 30 GHz is -2.5 dB and about the same for all antenna locations. This loss is quite remarkable at

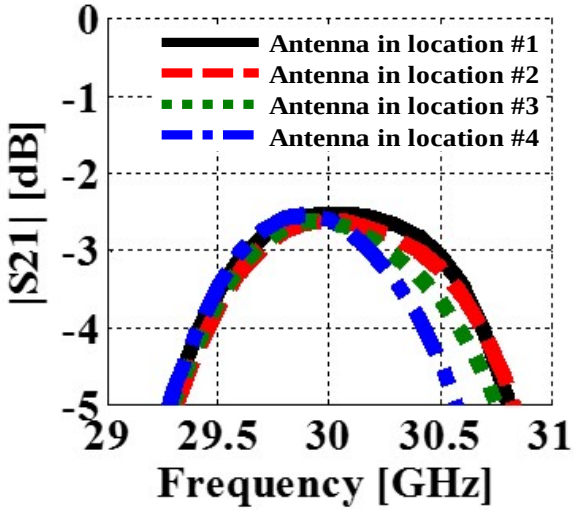

Figure 4.8: Normalized relative power delivered to the antenna element of the MFPA excited by the resonant corporate feed network. The antenna is positioned among location #1-#4.

This loss is quite remarkable as compared to a conventional FPA implementation. A conventional 1D 8 element FPA requires a total of 7 single pole double throw (SP2T) switches in its feed network. An antenna element gets excited after the incident RF power passes through 3 SP2T switches. The readily available commercial Ka band SP2T switches exhibit about 1 dB insertion loss [74, 108]. Therefore, at least 3 dB of the input power is dissipated in the switches even without considering the loss associated with the microstrip lines, their bends, and interconnects. Consequently, in addition to significant RF hardware reduction, the MFPA provides a loss performance comparable with the conventional FPAs.

4.2.3. Straight Feed Network

The previous section described the design and performance of a resonant corporate network fed MFPA. As it was shown, the array pattern exhibited high SLL due to the radiation leakage of the unloaded stubs. Therefore, the key to reduce the SLL is to employ a feed network that would exhibit fewer number of open stub resonators. As shown in Figure 4.9, this can be accomplished

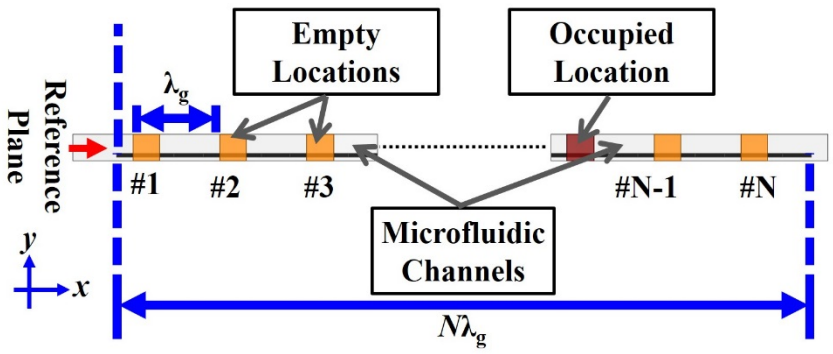

Figure 4.9: Schematic of a MFPA excited by a resonant straight feed network.

by a compact straight microstrip line terminated with an open circuit. In this configuration, the antenna will be loaded with a single straight open stub resonator regardless of its location. Therefore, it is expected that the MFPA will radiate with a relatively lower SLL as compared to

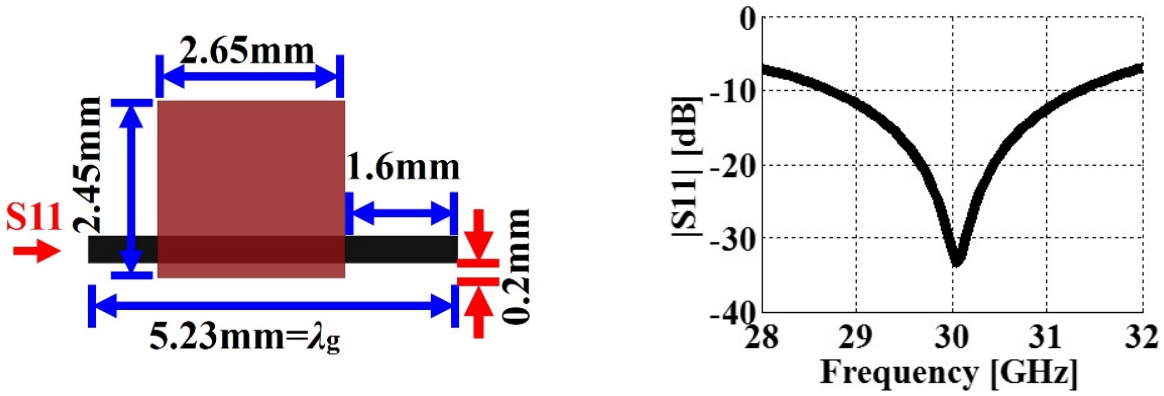

(a) (b)

Figure 4.10: Schematic of the 30 GHz proximity coupled patch antenna designed for the straight feed network, and b) its simulated $|S_{11}|$.

the corporate network fed case. The synthesis of the feed network starts with the antenna design as shown in Figure 4.10(a). The antenna is proximity coupled to a λ_g long microstrip line in order to generate $N\lambda_g$ spaced antenna locations similar to the corporate feed network. The simulated $|S_{11}|$ response reveals 8.67% $|S_{11}| \leq$ -10 dB bandwidth at 30 GHz as shown in Figure 4.10(b). The simulated realized gain is 7 dB into semi-infinite Rexolite. In MFPA realization, the open circuit end of the proximity coupled microstrip line will be cascaded with other λ_g long microstrip lines as shown in Figure 4.9. The number of these λ_g long sections depends on the number of possible beam locations in the feed network (i.e. N) and the relative location of the antenna element (i.e. i). λ_g long microstrip lines ensure that the open-circuit condition at port #2 (see Figure 4.11) is preserved and antenna maintains its impedance matching. The impedance matching also holds when antenna is repositioned over the feed network in increments of λ_g. The bandwidth of the resonant straight microstrip line fed MFPA can be analytically evaluated by first by considering the antenna as a two port network and modeling it in the equivalent circuit shown in Figure 4.11. As seen, when the antenna is at location i, the antenna is cascaded with an $(N\text{-}i)\lambda_g$ open stub

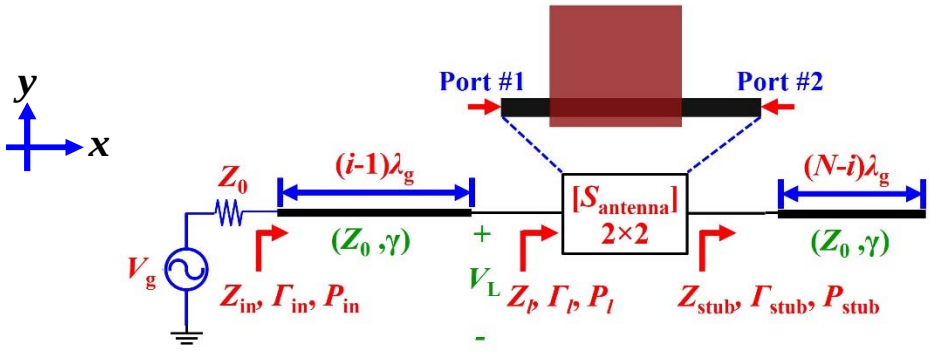

Figure 4.11: The equivalent circuit of the MFPA excited by the straight feed network where the antenna is positioned at location #*i*.

resonators and fed by an $l = (i-1)\lambda_g$ long transmission line. Since the open stub impedance is $Z_{stub} = Z_0 \coth[\gamma(N-i)\lambda_g]$ with $\gamma = \alpha + j\beta$, the input reflection coefficient seen towards the antenna Γ_l becomes [37]:

$$\Gamma_l = S_{11} + \frac{S_{12}S_{21}\Gamma_{stub}}{1 - S_{22}\Gamma_{stub}}, \tag{4.9}$$

where $\Gamma_{stub} = (Z_{stub} - Z_0)/(Z_{stub} + Z_0)$. Then, the load impedance (Z_l) is evaluated as:

$$Z_l = Z_0 \frac{1 + \Gamma_l}{1 - \Gamma_l} \tag{4.10}$$

and the input impedance Z_{in} is calculated as:

$$Z_{in} = Z_0 \frac{Z_L + Z_0 \tanh[(i-1)\lambda_g]}{Z_0 + Z_L \tanh[(i-1)\lambda_g]}. \tag{4.11}$$

Consequently, the S_{11} of the MFPA is determined from (4.11) as $S_{11} = (Z_{in} - Z_0)/(Z_{in} + Z_0)$.

Once Γ_l and Z_{in} are determined, then the delivered power to the load (Z_l) can be calculated as [47]:

$$P_l = \frac{1}{2Z_0}|V^+|^2(1 - |\Gamma_l|^2), \tag{4.12}$$

where V^+ is given by:

$$V^{+} = \frac{Z_{in}}{Z_{in} + Z_0}\left(\frac{1}{e^{\gamma(i-1)\lambda_g} + \Gamma_{in}e^{-\gamma(i-1)\lambda_g}}\right) \tag{4.13}$$

In (4.12), P_l is sum of the dissipated powers in the loading stub (P_{stub}) and antenna ($P_{antenna}$). P_{stub} can be related to P_l using the well-known equations for operational power gain (G_p) of two port networks [109]:

$$G_p = \frac{P_{stub}}{P_l} = \frac{1}{1 - |\Gamma_l|^2}|S_{21}|^2 \frac{1 - |\Gamma_{stub}|^2}{|1 - S_{22}\Gamma_{stub}|^2}. \tag{4.14}$$

Therefore, $P_{antenna}$ becomes:

$$P_{antenna} = P_l - P_{stub} = P_l(1 - G_p). \tag{4.15}$$

The bandwidth of the resonant straight microstrip line fed MFPA can be conveniently investigated with the above transmission line theory based analysis for different N values. It is found that the antenna element exhibits its minimum bandwidth when it occupies the first location (i=1). This is expected as in this case, the antenna is terminated with the longest possible open stub. Therefore, the MFPA bandwidth is determined by the bandwidth of the antenna when it is at location i=1. Figure 4.12(a) depicts the bandwidth performance of the MFPA as a function of N.

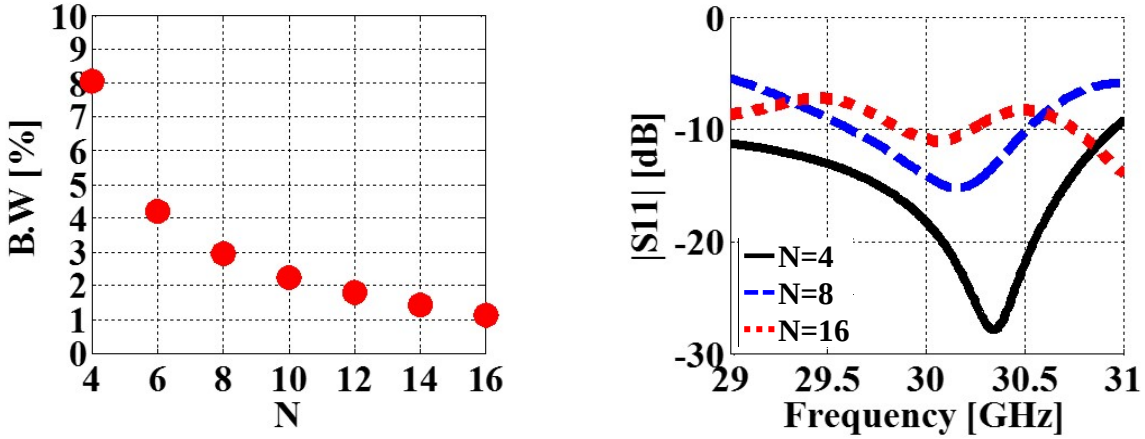

(a) (b)

Figure 4.12: a) The bandwidth of N element MFPA excited by a resonant straight feed network. The bandwidth decreases with N, and b) $|S_{11}|$ performances for different N when the antenna is at location #1.

Similar to the resonant corporate network case, the bandwidth decreases with increasing N. For example, the array exhibits 8% and 3% bandwidths for N=4 and 8, respectively. The corresponding $|S_{11}|$ curves for N=4, 8, and 16 are shown in Figure 4.12(b). A reduction in the array bandwidth is clearly observed as N increases from 4 to 16. Moreover, increasing N degrades the input impedance matching at the design frequency since the open stub becomes physically longer and increases its loading on the antenna.

To verify the transmission line theory analysis and investigate the radiation performance, an N=8 element MFPA was designed. The feed network synthesis starts with forming N-cascade of the λ_g long microstrip line shown in Figure 4.10(a). Next, the straight network is loaded with the patch antenna element that can be microfluidically moved among 8 locations separated by λ_g. The $|S_{11}|$ performance calculated with the transmission line theory as the antenna is moved among these 8 locations is shown in Figure 4.13(a) and (b). A good $|S_{11}|$<-15 dB impedance match is achieved at each antenna location at 30 GHz. The antenna exhibits the minimum bandwidth at location #1. The full wave simulated $|S_{11}|$ performance is shown in Figure 4.13(c) and (d). By comparing the performances, it is seen that a good agreement exists between the transmission line theory analysis and the full wave simulation. The simulated $|S_{11}|$ < -10 dB bandwidth is 2.9% and also agrees well with the expected 3% bandwidth from transmission line theory analysis. Figure 4.14(a) and (b) depict the power delivered to the antenna element relative to the input power P_{in}. The antenna is excited with the maximum power level (-1.39 dB at 30 GHz) when it is positioned at location #1. The relative power delivered to the antenna drops to -3.84 dB at 30 GHz when the antenna is positioned at location #8. The average loss is 2.83 dB and implies a comparable performance to a conventional SP2T switch based FPA implementation. The radiation

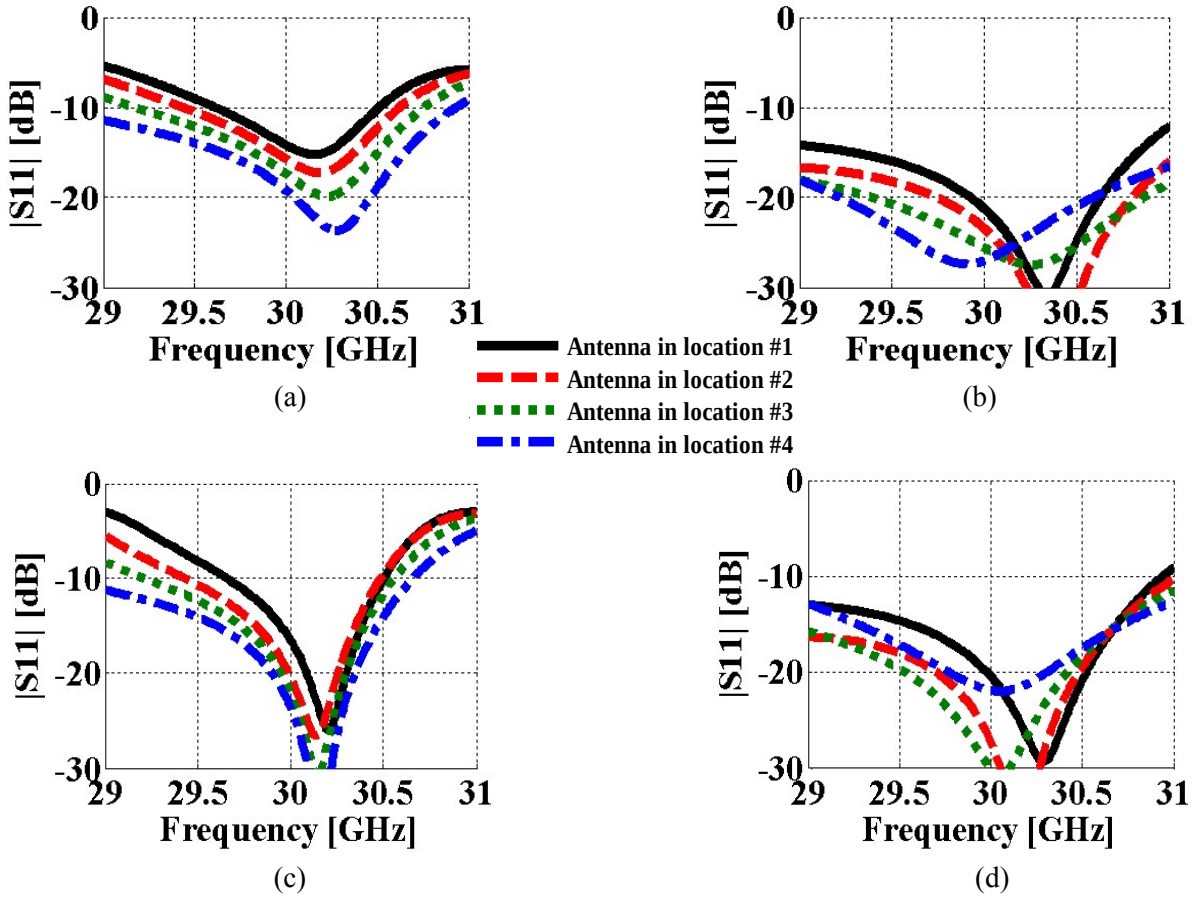

Figure 4.13: $|S_{11}|$ of the 8 element MFPA excited by the resonant straight feed network. (a)-(b) transmission line theory analysis; (c)-(d) full wave simulation. Antenna element is at locations #1-#4 for (a)-(c), and #5-#8 for (b)-(d).

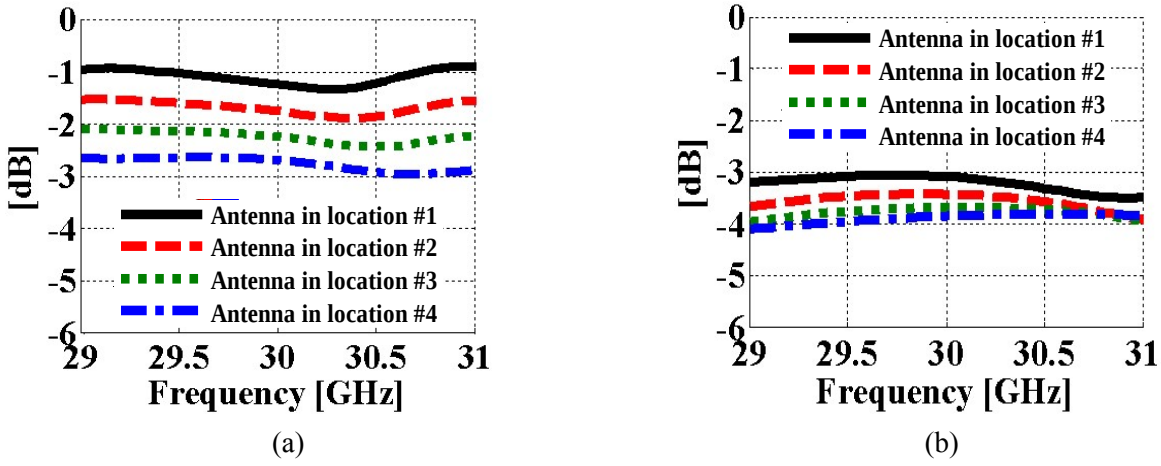

Figure 4.14: Normalized relative power delivered to the antenna element of the MFPA excited by the resonant straight feed network. The antenna is moved among locations: a) #1-#4, and b) #5-#8.

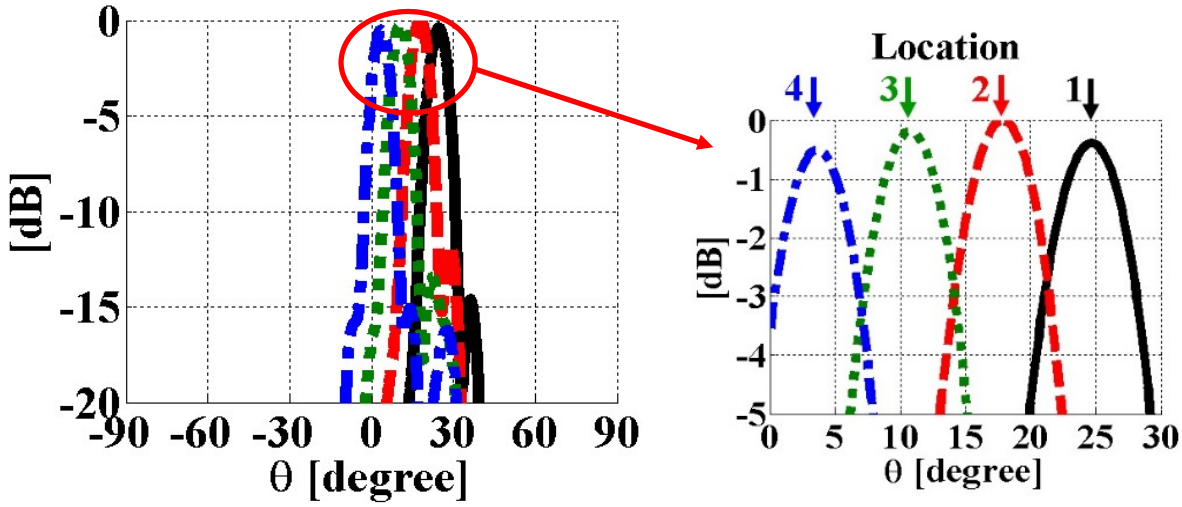

Figure 4.15: The normalized radiation pattern of the MFPA excited by the resonant straight feed network. The SLL is < -20 dB.

patterns of the MFPA at *x-z* elevation plane when the antenna element is moved among locations #1-#4 is shown in Figure 4.15. The array scans the beam over $\pm 25^0$ FoV with 29 dB directivity. Most importantly, the SLL is reduced by more than 10 dB relative to that obtained from the resonant corporate network fed MFPA. Specifically, the resonant based straight line fed MFPA exhibits -20 dB SLL relative to the peak directivity. Similar SLL performance is also achieved in the *y-z* elevation plane.

By resorting to a center fed straight network as shown in Figure 4.16(a), the longest stub length loading the antenna can be further reduced for a given N to achieve bandwidth improvement. The equivalent circuit, shown in Figure 4.16(b), is employed to estimate the array's bandwidth when excited with this center fed configuration. The transmission line analysis is similar to the edge fed configuration and not detailed for brevity. Similar to the edge fed network, the bandwidth of the center fed network decreases with N as shown in Figure 4.17(a). However, a higher bandwidth performance is achieved for the center fed network relative to the edge fed straight and corporate resonant networks. For instance, the bandwidth increases from 3% to 5.33% for N=8.

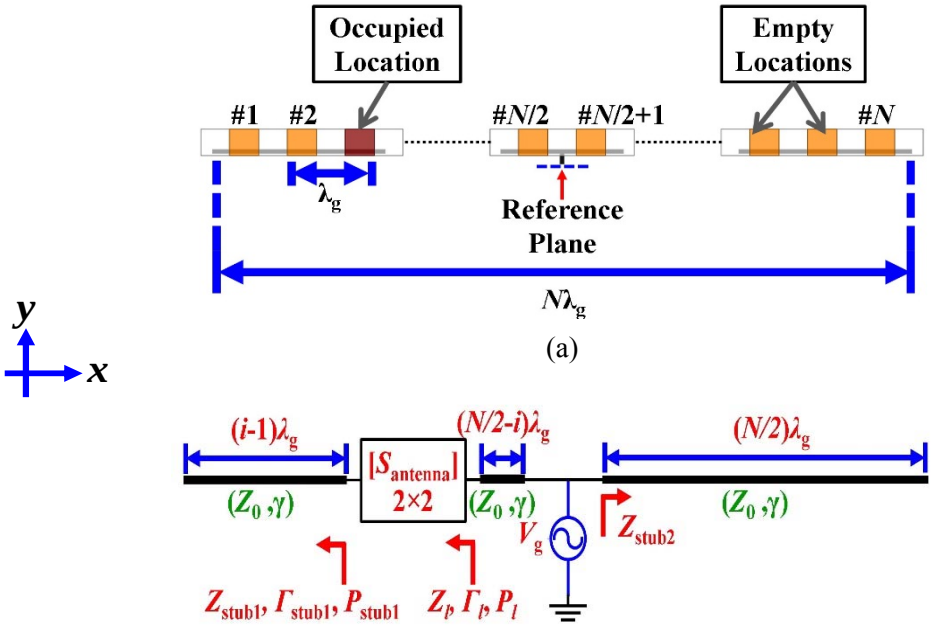

Figure 4.16: a) Schematic of a center fed MFPA excited by a resonant straight feed network, and b) its equivalent circuit.

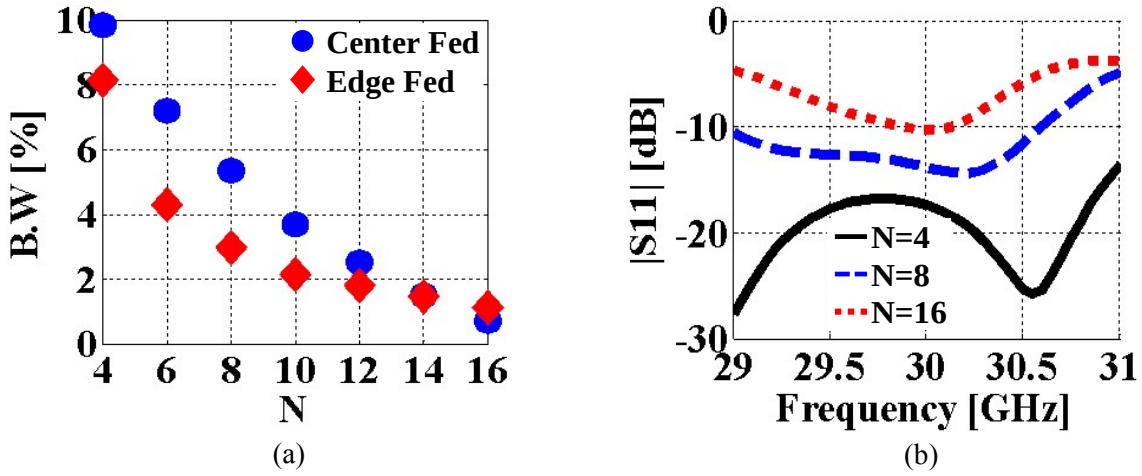

Figure 4.17: a) The bandwidth performance comparison of *N* element MFPA excited by a center and edge fed resonant straight network. The center fed array exhibits relatively higher bandwidth, and b) $|S_{11}|$ performances the center fed array for different *N* when the antenna is at location #*N*/2.

Figure 4.17(b) depicts the $|S_{11}|$ of the center fed array for N = 4, 8 and 16. The shown performances reveal degradation of the impedance matching as N increases. An 8 element MFPA excited by the center fed straight resonant network was designed to verify the transmission line theory analysis. Figure 4.18(a) demonstrates the $|S_{11}|$ when the antenna element is moved among locations #1-#4. The array exhibits $|S_{11}| < -10$ dB at 30 GHz regardless of the antenna location. The bandwidth is at its minimum when the antenna is located at location 4 (i.e., $N/2$). The power delivered to the antenna element relative to the input power is shown in Figure 4.18(b). Specifically, at 30 GHz, the power delivered to the antenna is 1.45 dB below the input power regardless of its location. As compared to the edge fed straight resonant network and corporate resonant network, the center fed straight resonant network performs the best in terms of bandwidth and power loss. The radiation pattern of this MFPA exhibits SLL < -20 dB and similar to that shown in Figure. 4.15.

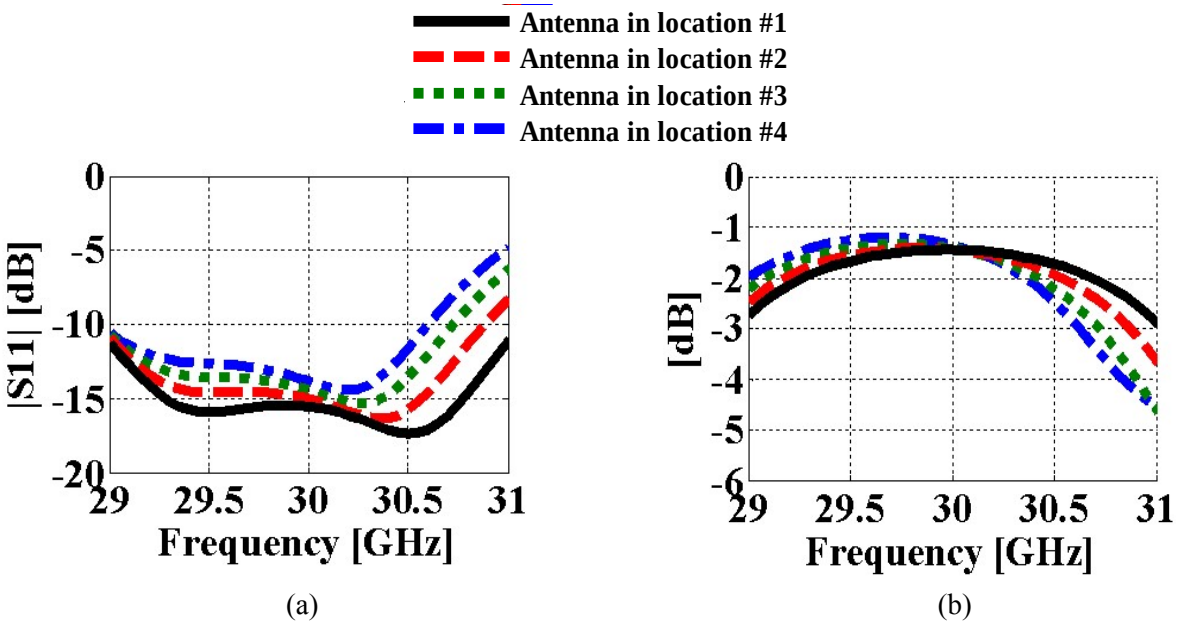

Figure 4.18: The center fed array performance as the antenna is moved among locations #1-#4: a) $|S_{11}|$, and b) antenna's delivered power.

4.2.4. Non-Resonant Feed Network

Although the resonant straight feed networks improve the SLL, they still exhibit limited bandwidth only suitable for narrowband applications. For wideband operations, the bandwidth of the feed network can be significantly improved by resorting to a non-resonant layout as shown in Figure 4.19(a). Similar to the resonant straight feed network, this layout consists of a long straight

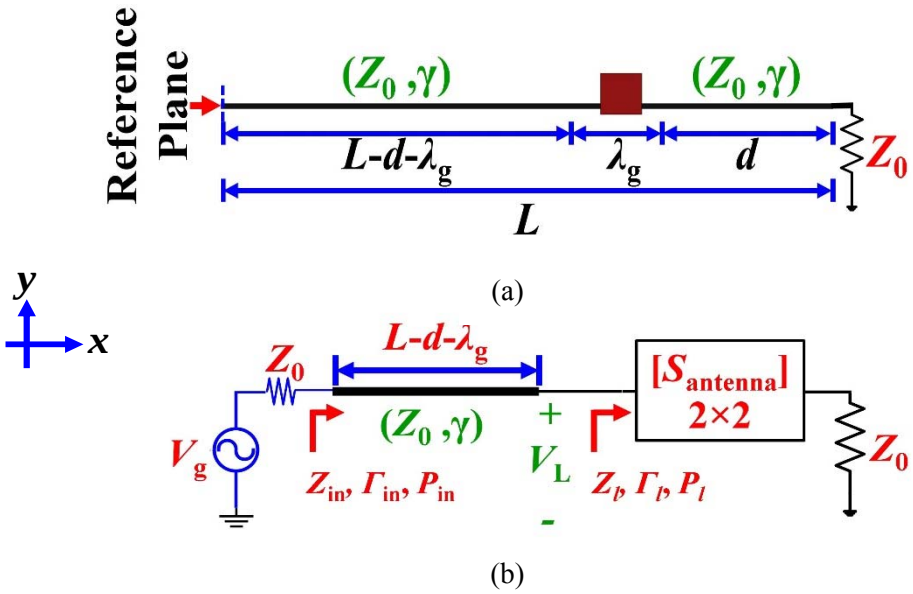

Figure 4.19: a) The non-resonant straight feed network exciting a proximity coupled patch antenna, and b) its equivalent circuit.

microstrip line proximately coupled to a microfluidically repositionable patch antenna. However, different than the resonant network, the line is terminated with Z_0. Therefore, the feed network is non-resonant without bandwidth limitation at the expense of being lossy. Moreover, in this layout, the antenna element can be positioned at any arbitrary location without losing its impedance matching. Hence, the feed network allows for continuous beam-scanning. Nevertheless, in the following performance analysis studies, the antenna will be assumed to be positioned at specific locations separated by λ_g to provide a comparison to the MFPAs excited by resonant feed networks.

The equivalent circuit shown in Figure 4.19(b) for the non-resonant feed network is identical to the straight resonant feed network except the terminating impedance (i.e. open circuit vs. Z_0). Therefore, the $|S_{11}|$ and $P_{antenna}$ can be evaluated using the equations from (4.9) to (4.15) by replacing Z_{stub} with Z_0. The $|S_{11}|$ performances calculated from the transmission line theory analysis are shown in Figure 4.20(a) and (b). Figure 4.20(c) and (d) depicts the $|S_{11}|$ responses obtained from full-wave analysis. It is again observed that the two methods are in very good agreement. Specifically, the MFPA exhibits $|S_{11}| \leq$ -8 dB over the entire simulated frequency range from 29 GHz to 31 GHz. Figure 4.21(a) and (b) depict the $P_{antenna}$ calculated from the transmission line theory analysis. As expected, at the center frequency of the antenna element (i.e. 30 GHz), $P_{antenna}$ achieves its maximum value. Specifically, $P_{antenna}$ is 3.45 dB lower relative to the P_{in} when the antenna is positioned at location #1. As the antenna moves towards location #8, $P_{antenna}$ drops and becomes 5.22 dB lower than P_{in} due to the lossy nature of the straight transmission line. The average loss is 4.35 dB and this is still comparable to the conventional SP2T switched implementation of the same FPA. Figure 4.22 depicts the scanned beams in the *x*-*z* elevation plane as the antenna is moved among locations #1-#4. Similar to the previous design, the array scans the beam with $\pm 25^0$ FoV with a -20 dB SLL.

4.3. Experimental Verification

Performance of an 8 element MFPA excited by the resonant corporate microstrip line feed network has been experimentally demonstrated in the previous chapter. In this chapter, due to its lower SLL performance, we have selected to experimentally verify the performance of the 8 element MFPA designed in Section 4.2.3 to operate with the edge fed resonant straight microstrip line network.

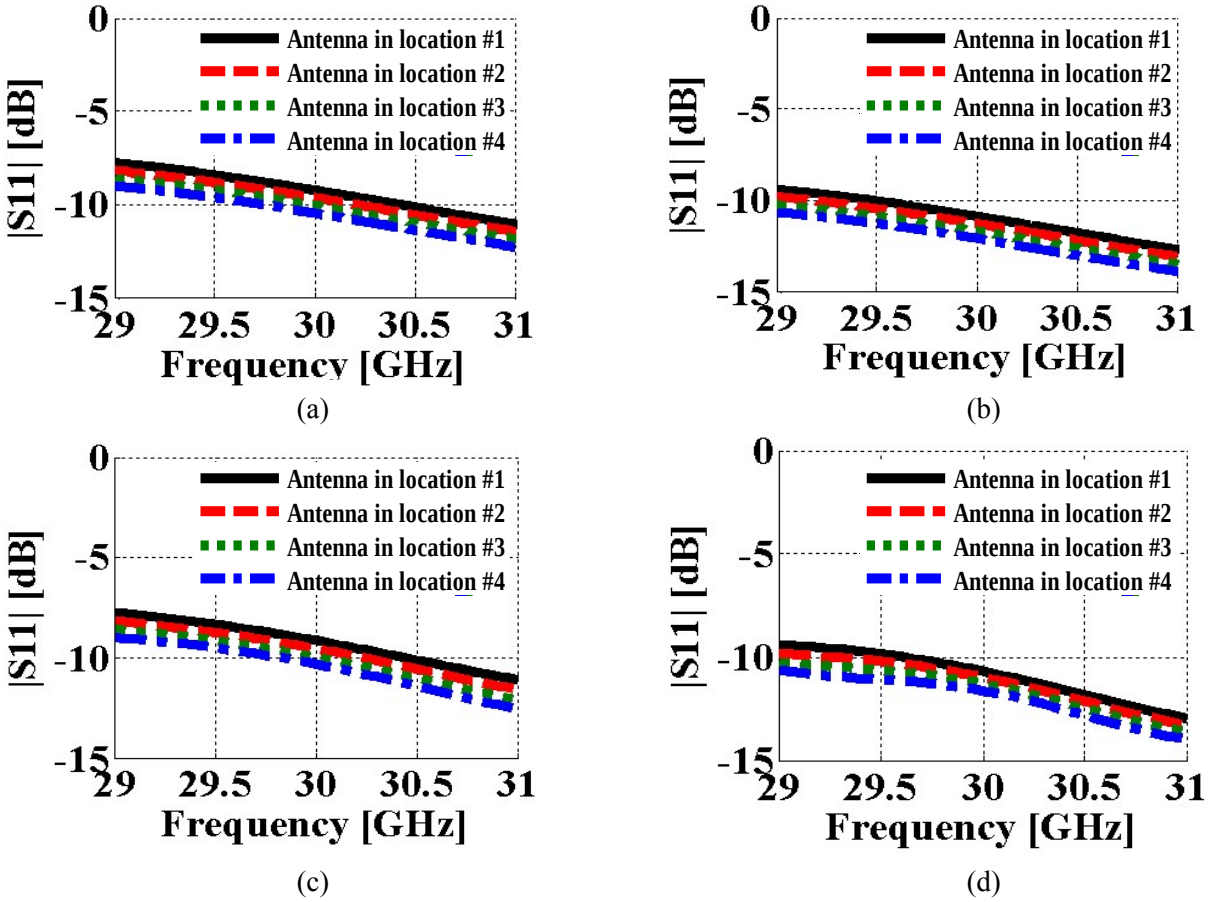

Figure 4.20: $|S_{11}|$ responses of the MFPA excited by the non-resonant straight feed network. (a)-(b) transmission line theory analysis and (c)-(d) full wave simulation. Antenna element is at locations #1-#4 for (a)-(c), and #5-#8 for (b)-(d).

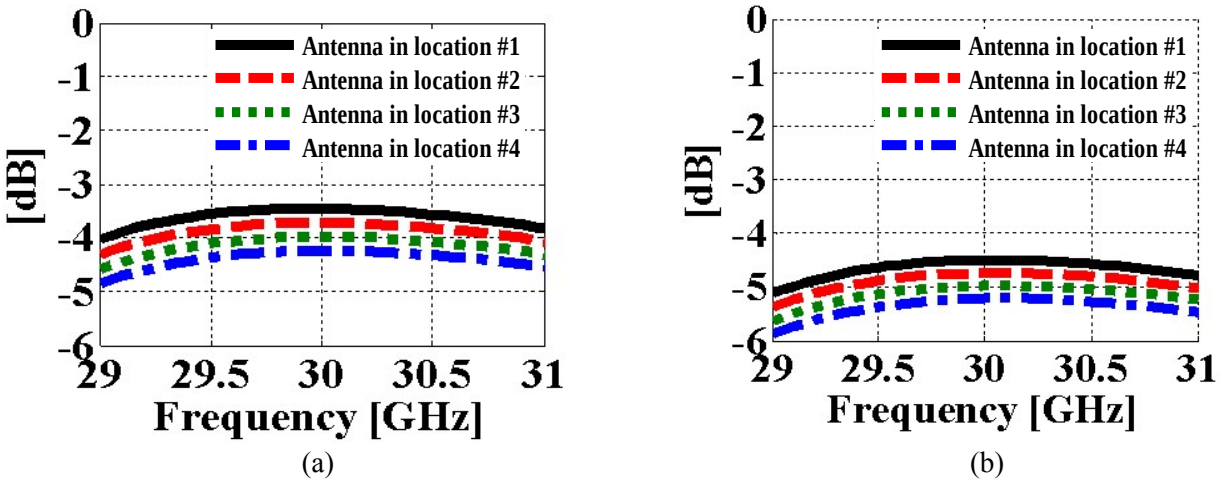

Figure 4.21: Normalized relative power delivered to the antenna element of the MFPA excited by the non-resonant straight feed network. The antenna is moved among locations: a) #1-#4, and b) #5-#8.

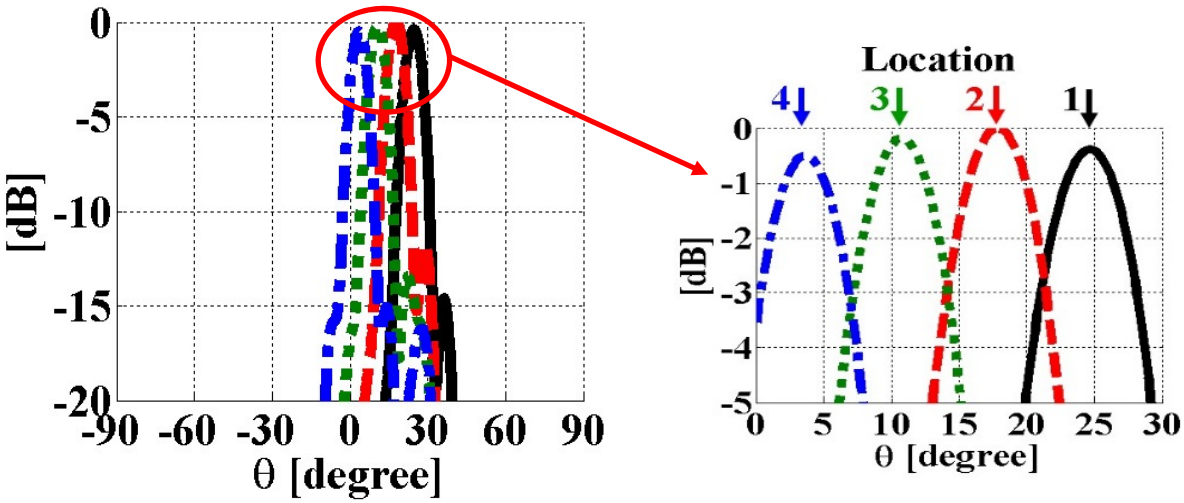

Figure 4.22: The normalized radiation pattern of the MFPA excited by the non-resonant straight feed network. The SLL is < -20 dB.

4.3.1. Fabrication of Microfluidic Channel

The fabrication process consists of soft lithography for forming the microfluidic channel and feed board etching to form the microstrip line. The soft lithography process involves photo-lithographically defining the inverted mold of the channel by using a negative photoresist (SU8-2075) on a Si wafer. Next, PDMS (mixed in the ratio of 10:1 with its curing agent and degassed) is poured on top of the inverted mold and left to cure overnight. Although heating accelerates the curing; room temperature curing is preferred to minimize the contraction of the polymer. The cured PDMS is peeled off from the Si wafer and a metallized RT5880LZ plate having the same dimension as that of the antenna is placed inside the channel. The thickness of the plate is 250 μm and the metallized coating is 17 um. The micro-channel is filled up with low loss Teflon solution that pushes the metallized plate to move it inside the channel.

Experiments were conducted for plates made of different materials before deciding on the RT5880LZ as the metallized plate substrate. The Teflon solution obtained from DuPont is 400S2-100-1. It consists of 1% Teflon powdered resin dissolved in 3M FC-40 solution. FC-40 has a

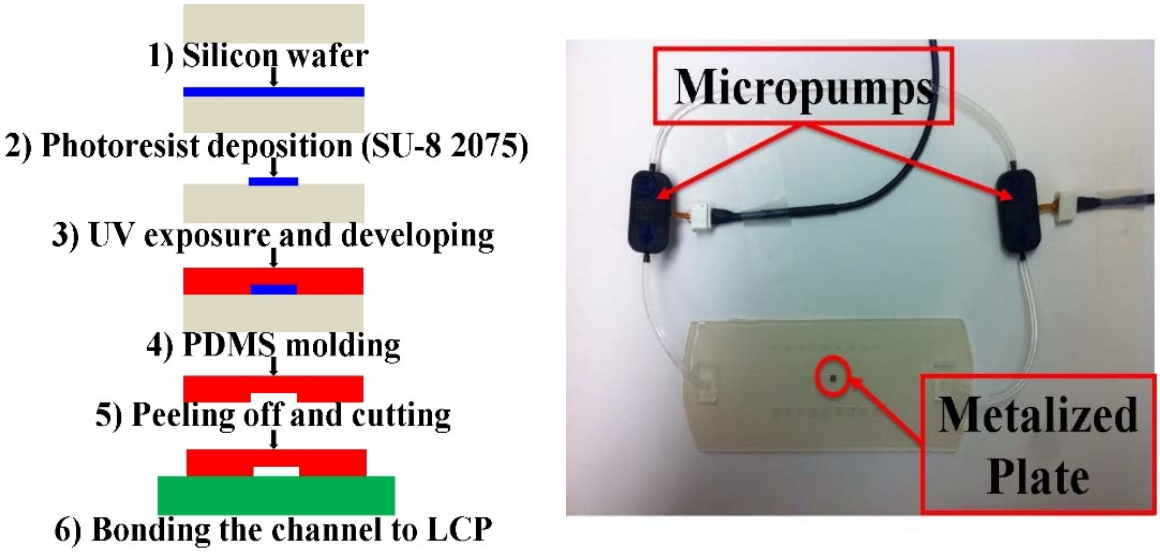

(a) (b)

Figure 4.23: a) Fabrication process of the microfluidic channels, and b) developed closed loop system with the micropumps connected to channels that are filled with a low loss dielectric solution. The micropumps are run using a controlling unit.

density of 1.855g/cm^3. It was observed that the plates made up from higher density materials such as silicon (2.33g/cm^3) and quartz (2.65g/cm^3), could not be moved using the Teflon solution. On the other hand, plates of lower density substrate materials such as PMMA (1.18g/cm^3) and RT5880LZ (1.4g/cm^3) could be moved inside the channel using the Teflon solution. Readily available copper metallized RT5880LZ substrates from Rogers Corp. were selected above the PMMA alternative, as this alleviated the need for in-house metallization. The microfluidic channel is bonded to a 100 um thick LCP layer using the process discussed in [110]. The process flow for fabricating the channel with the metallized plate is illustrated in Figure 4.23(a). The feed board and the microchannel formed by PDMS-LCP are bonded together by using the Afterwards, a closed loop pumping system is developed by connecting the pipes from the syringes to micropumps. The closed loop system is demonstrated in Figure 4.23(b).

4.3.2. Microfluidic Channel Flow Characterization

The successful implementation of a MFPA depends on the ability to move and control the flow of the metallized patch inside the rectangular microfluidic channel. Having selected the material for the metallized plate substrate as RT5880LZ, further experiments were performed in

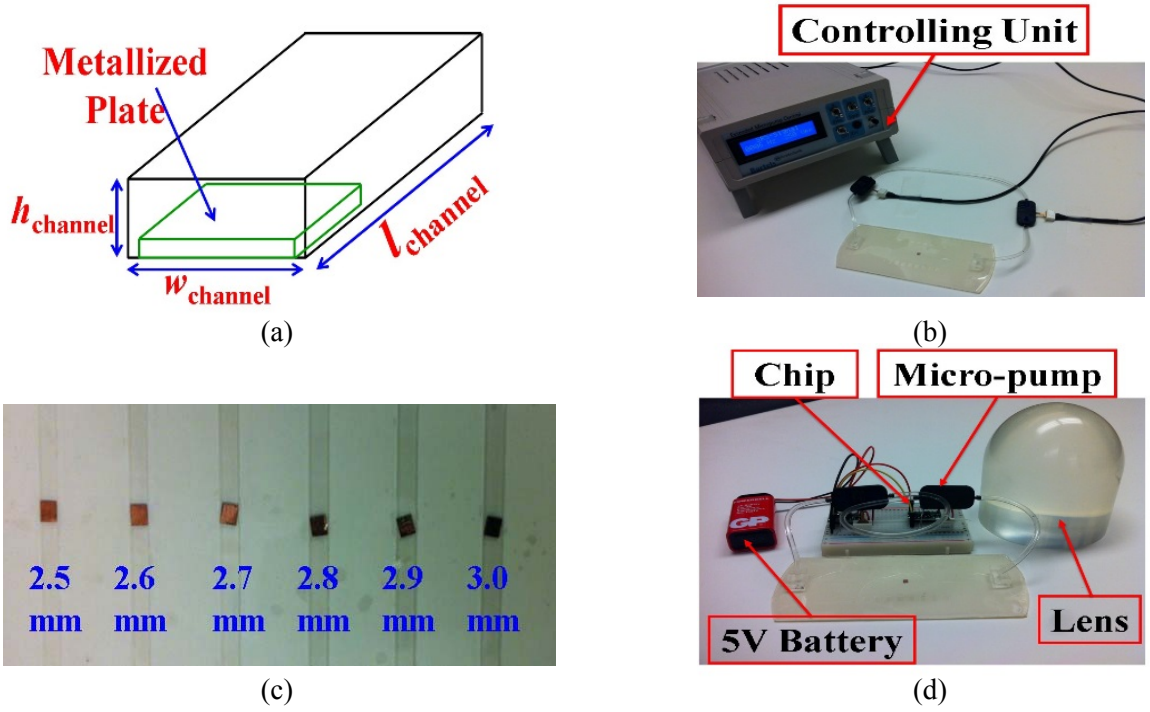

Figure 4.24: a) Schematic of metallized plate in a microfluidic channel. $l_{channel}$ is 100 mm, b) the test setup of the plate's flow in a microfluidic channel, c) microfluidic channels with different widths, and d) the control setup of the plate's flow using a compact circuitry.

microfluidic channels of different widths to determine with which channel dimensions the plate would move freely without getting tilted or rotated. In these experiments, the length of the channel was fixed as $l_{channel}$=100 mm (see Figure 4.24(a)). The flow characterization setup depicted in Figure 4.24(b) consisted of two piezo-pumps from Bartels® connected to the channels and controlled using an mp-x controlling unit [111]. Different channels with widths ranging from 2.5 mm to 3 mm for a fixed channel height of 400 µm were investigated. As shown in Figure 4.24(c),

the channel widths beyond 2.6 mm distorted the plate movement and led to a disoriented flow. The channel width of 2.6 mm was found to be appropriate for reliable flow of the patch antenna. Figure 4.24(d) depicts a compact circuitry for controlling the flow in the microchannels. Specifically, two micropumps are actuated using a chip [111] that is biased with a 5 V battery. The whole circuitry is placed on the top of a breadboard.

The switching speed of the MFPA is determined by how fast the plate can be moved inside the channel. This depends on the flow rate (Q) of Teflon solution that can be generated inside the channel. The flow rate is related to the cross sectional area (A) of the rectangular channel [112] as:

$$Q = \tilde{v} \times w_{channel} \times h_{channel}, \tag{4.16}$$

where $\tilde{v}$ is the mean velocity of Teflon inside the channel. The mean velocity of a liquid with viscosity μ is given by:

$$\tilde{v} = \frac{\Delta P h_{channel}^2}{\mu l_{channel}} \left[\frac{1}{3} - \frac{64 h_{channel}}{\pi^5 w_{channel}} \tanh\left(\frac{\pi w_{channel}}{2 h_{channel}}\right)\right]. \tag{4.17}$$

Substituting (4.17) in (4.16) we get:

$$Q = \frac{\Delta P w_{channel} h_{channel}^3}{\mu l_{channel}} \left[\frac{1}{3} - \frac{64 h_{channel}}{\pi^5 w_{channel}} \tanh\left(\frac{\pi w_{channel}}{2 h_{channel}}\right)\right] = \frac{\Delta P}{R_{fluid}}. \tag{4.18}$$

Equation (4.18) relates the pressure difference (ΔP) needed across the ends of the channel to a steady flow rate of Q. The channel dimensions determine the resistance offered by the fluid (R_{fluid}) to the external stimuli trying to flow the liquid inside the channel. In the measurement setup, Bartels piezo actuated micro-pumps were used as the external stimuli to generate the constant flow inside the channel with dimensions of $l_{channel}$=100 mm, $w_{channel}$=2.6 mm and $h_{channel}$=0.4 mm. R_{fluid} was calculated to be 3.3×10^{10} kg m^{-4} s^{-1}. The pumps were run and the actuation parameters (input voltage amplitude and frequency) were adjusted to get maximum flow rate. The fastest time

recorded that the pump takes to move the plate from 1st location to the 8th one was 108 s which implied a flow rate of 0.96 mm^3 s^{-1}. Substituting these values in (4.18) we get the pressure developed across the ends of the channel as 31.68 Pa. This value is seen as the resistance experienced by the piezo-pump when trying to pump Teflon along with the metallized plate. This opposing pressure is termed as the back-pressure and it affects the flow rate that can be generated by the piezo-pump as:

$$Q = Q_{max}\frac{\Delta P_{max} - \Delta P_{back}}{\Delta P_{max}}, \tag{4.19}$$

where ΔP_{max} is the maximum back pressure that the pump can tolerate (at ΔP_{max}, Q=0), and Q_{max} is the maximum flow rate generated by the pump with no back-pressure. Substituting the expression for ΔP_{back} from (4.18) into (4.19) we derive the actual flow rate of the piezo-pump as:

$$Q = \frac{Q_{max}}{1 + \frac{Q_{max}R_{fluid}}{\Delta P_{max}}}. \tag{4.20}$$

From equation (4.20), it is observed that the maximum flow rate that the pump can generate for a given liquid is the critical factor for determining the switching speed. The piezo-pumps (13.5 s) are slow because of the lower Q_{max} rating of the pump for a viscous liquid like FC-40. Using pumps with a higher Q_{max} rating would increase Q. This was verified by using DC gear pumps (GM1606 [113]). The switching speed between any two adjacent locations was measured to be 0.75 s. The speed could be increased further; however, the high pressure exerted by the pump led to rupturing of the bond between PDMS-LCP. The piezo based pumps offer the advantage of lightweight and low power consumption, but they result in slower motion. The DC gear pumps, however, consume more power 5.5 W (2.75 A @ 2 V), but significantly boost the switching speed of the array. As seen in (4.20), for two pumps with same Q_{max} rating, if R_{fluid} can be reduced the flow rate will increase.

4.3.3. Performance of the MFPA

Figure 4.25(a) depicts the milled feed board, whereas the microfluidic channel is shown in Figure 4.25(b). A custom designed Styrofoam holder was built to hold the structure as depicted in Figure 4.25(c). The feed board and microfluidic channel were pressed together and flushed on the back surface of the lens as shown in Figure 4.25(d). Figure 4.26(a) and (b) depict the measured

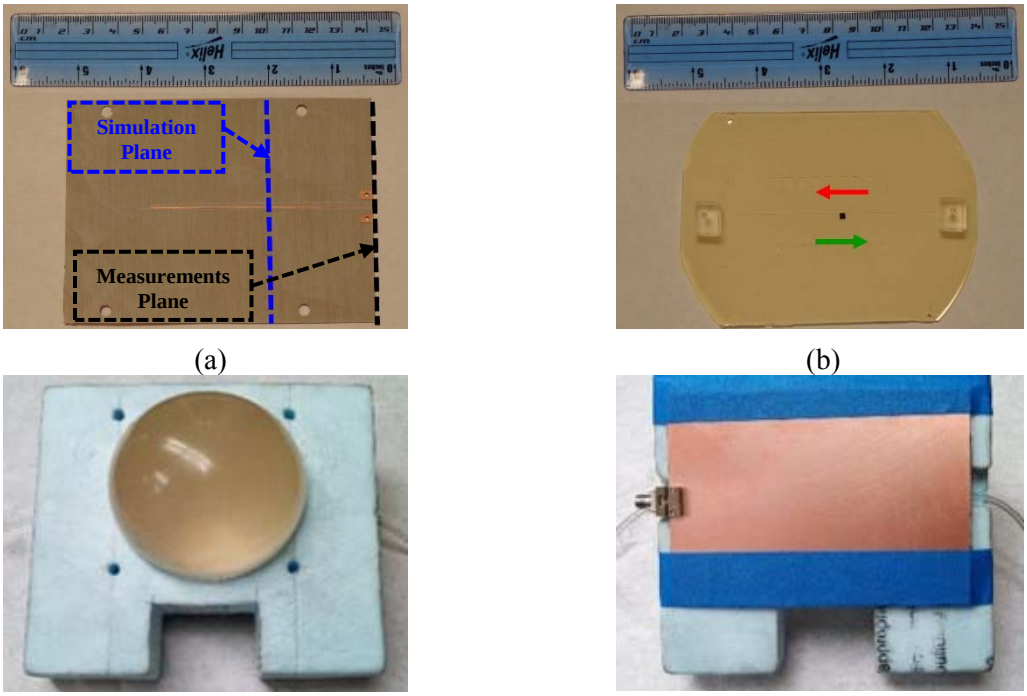

Figure 4.25: a) Etched straight resonant based feed network board. The reference planes are shown, b) fabricated microfluidic channels, c) the extended hemispherical dielectric lens fixed in a custom designed Styrofoam holder, and d) the feed network and channels flushed on the back surface of the lens.

$|S_{11}|$ performance as the antenna element moves from location #1 to #8. As expected, the array exhibits a very good impedance match at 30 GHz. The array bandwidth is limited by the antenna element's performance at location #1. The measured bandwidth is 4% and higher than the 3% expected from the analytical analysis and full wave simulation. This discrepancy is due to the different reference plane location used in the experimental setup. As shown in Figure 4.25(a), the reference plane of the measurement is $8\lambda_g$ further away from that of the simulation to accommodate

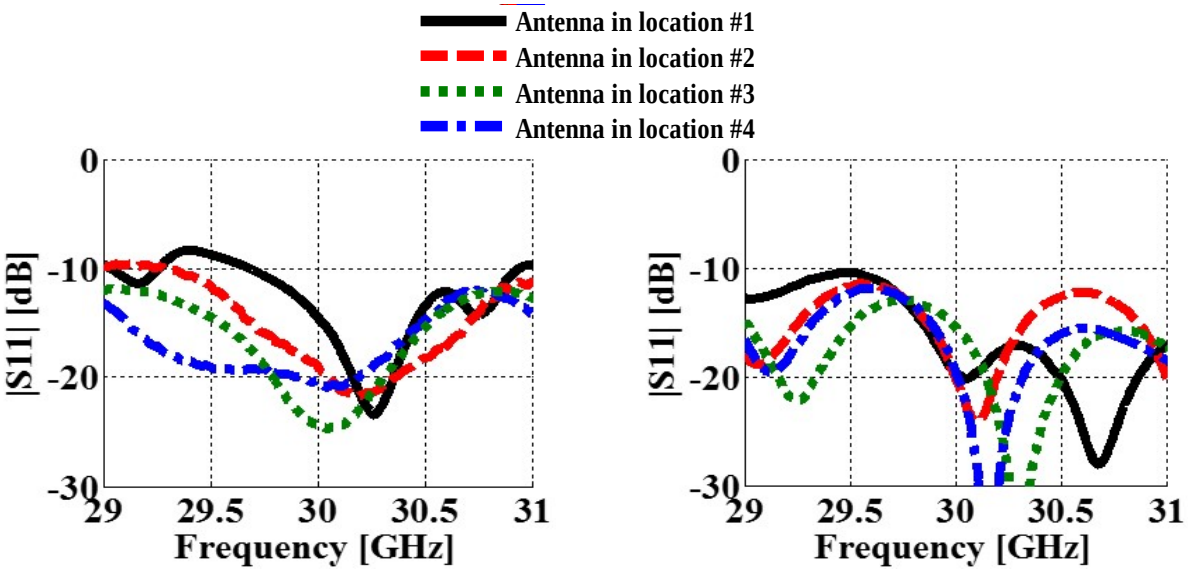

Figure 4.26: Measured $|S_{11}|$ response of the resonant based straight line fed MFPA when the metallized plate is at locations: a) #1-#4, and b) #5-#8.

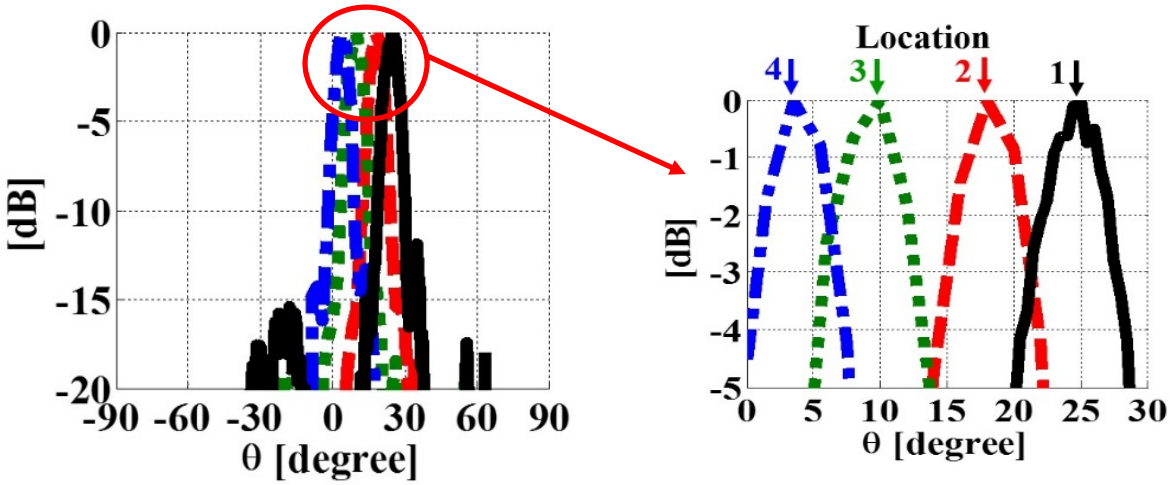

Figure 4.27: The array measured normalized patterns as the metallized plate was moved among locations #1-#4.

an end-launch 2.92 mm connector to feed the array. The re-simulation of the MFPA with the extended reference plane predicts a 3.9% bandwidth that agrees well with the measurement. The increase in bandwidth is associated with the additional loss of the $8\lambda_g$ long microstrip line

extension. The beam-scanning performance was tested by measuring the gain patterns when the antenna element was moving among locations #1-#4. Figure 4.27 shows the measured normalized radiation patterns exhibiting 7^0 HPBW agreeing with the measured and calculated scan angles. Table 4.1 compares and lists the measured gains as well as the simulated and measured scan angles. A very good agreement is observed for the measured and calculated scan angles with a deviation no more than 1^0. The maximum measured gain is 23.5 dB when the antenna is at location #3. This implies 5.5 dB loss as compared to the predicted 29 dB directivity. The feed network contributes to 2.25 dB loss (see Figure 4.14(a)), whereas 1.5 dB loss is from the extended transmission line, 1 dB lens loss, and 0.75 dB is the connector loss.

Table 4.1: The performance of the resonant based straight fed MFPA

Antenna in Reservoir:	**#1**	**#2**	**#3**	**#4**
Scan Angle (Measured, Calculated)	$(24^0,25^0)$	$(18^0,18^0)$	$(10^0,11^0)$	$(3^0,4^0)$
Measured Gain [dB]	22.8	21.5	23.5	22.4

4.4. Concluding Remarks

The designs and performance evaluations of corporate resonant, straight resonant, and straight non-resonant feed networks for microfluidic focal plane arrays (MFPAs) were presented. The transmission line theory based analysis was shown as a convenient and reliable method to design these feed networks for different array sizes (i.e. *N*) and predict the bandwidth and loss performances. It was demonstrated that the resonant corporate and straight feed networks exhibit similar behaviors in terms of bandwidth performance as *N* increases. On the other hand, the straight resonant feed networks enabled a better radiation characteristics with side lobe level (SLL) < -20 dB relative to the peak directivity. Non-resonant feed network was shown to overcome the

bandwidth limitation of the resonant based feed networks with possible continuous beam-scanning capability. Relative to the conventional SP2T switched based implementation of the presented FPAs, the power loss of the presented feed networks are comparable. The SLL performance improvement and the design techniques were experimentally verified through an 8 element extended hemispherical dielectric lens based MFPA prototype. Different than the recent work that relied on liquid metals, the antenna element of this MFPA was implemented from a metalized plate by carrying out flow characterizations on various microfluidic channel geometries. Specifically, the MFPA excited by the straight resonant feed network performed with <-20 dB SLL, 4% $|S_{11}|$<-10 dB bandwidth, 23.5 dB gain, and $\pm 25^0$ FoV. The MFPA offers a low-cost implementation for beam scanning arrays as it does not employ any active RF devices. This metalized plate approach paves the way for reliable liquid-metal-free microfluidic reconfigurable devices with higher efficiency and power handling capabilities. Studies for improving its scan speed and providing 2D beam-scanning capability are underway and will be discussed in future.

CHAPTER 5: FUTURE WORK

The continuous demands for miniaturized antenna arrays for GPS applications add more stringent constraints on antenna designers to provide smaller antenna elements. In addition, more antenna elements are required for such arrays to possibly protect communication links from additional interfering sources and signals. In order to obtain a smaller GPS antenna, the proposed CDL design can be re-designed on a high contrast ceramic ($\varepsilon_r = 25$) material. Using a high ceramic substrate results in a design that exhibits dimensions of $0.80" \times 0.80" \times 0.50"$. Furthermore, changing the arrangement of the loops to a vertical one yields to a stack up design, which obtains the capacitive coupling without using lumped elements. Therefore, the antenna's fabrication process is simplified, and thus, the array's fabrication and implementation becomes faster and simpler. In addition, an array with more compact inter-element separations can be constructed, and a center element can be possibly added to the array configuration for obtaining more nulls in the radiation pattern.

Both of the introduced MFPAs provided very encouraging performances in terms of measured high gain and beam scanning functionalities. Therefore, applying the microfluidic principles in antenna arrays should be further investigated for low cost implementation of 2D beam scanning. As shown in Figure 5.1, the 2D beam scanning capability is obtained by placing the MFPA on a step motor. The scanning in the elevation plane is achieved by moving the metallized plate in the microchannels using a micropump, whereas azimuth scanning is realized by rotating the step motor. As shown in the figure, the array is located at the focal point of a microwave lens. Hence, this research can be also extended to investigate novel design methodologies for microwave

lenses. For instance, a microwave lens with a gradient dielectric function is an interesting one to mitigate the diffraction effect on the arrays' radiation pattern. The prototyping of this suggested lens is possible using the 3D printing technology.

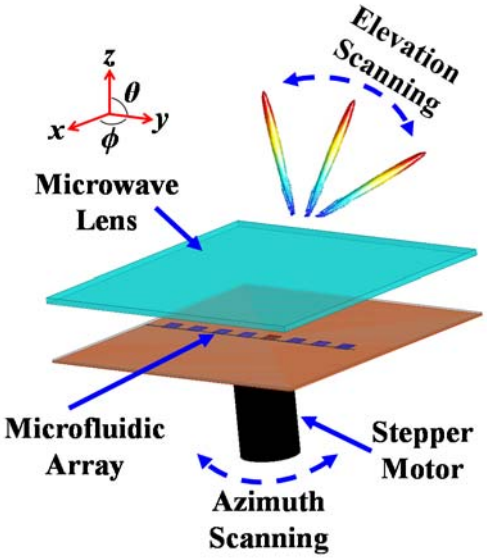

Figure 5.1: Realization of the 2D beam scanning functionality using the microfluidic principles.

Having a system with an improved reliability is also in the paramount importance. Specifically, a transition to hard substrates for implementing the microchannels is expected to improve both of the fabrication's yield and plate's flow in the microchannels. Moreover, using hard substrates would improve the array's power handling capabilities. As it was illustrated, the array's performance is dependent on the plate's location. Thus, it is necessary to construct a control system that tracks the plate's location and adjusts it when necessary. This control systems requires a feedback mechanism that senses the plates' location and provides a microcontroller with the required information. Different sensing mechanism can be employed and the inductive sensing approach is a potential candidate for this desired functionality.

REFERENCES

[1] L. C. Godara, "Applications of antenna arrays to mobile communications. I. Performance improvement, feasibility, and system considerations," *Proceedings of the IEEE,* vol. 85, pp. 1031-1060, 1997.

[2] E. D. Kaplan and C. J. Hegarty, *Understanding GPS: principles and applications*: Artech house, 2005.

[3] "Available Online: GPS Antenna System 1 (GAS-1): http://www.navair.navy.mil/index.cfm?fuseaction=home.display&key=52F74A0F-511F-40E3-81F5-FF16921DD18C."

[4] "Available Online: http://www.ic72.com/pdf_file/d/122907.pdf."

[5] Z. Yijun, C. Chi-Chih, and J. L. Volakis, "Tri-band miniature GPS Array with a single-fed CP antenna element," in *Antennas and Propagation Society International Symposium, 2007 IEEE*, 2007, pp. 3049-3052.

[6] J. A. Kasemodel, C.-C. Chen, I. J. Gupta, and J. L. Volakis, "Miniature continuous coverage antenna array for GNSS receivers," *Antennas and Wireless Propagation Letters, IEEE,* vol. 7, pp. 592-595, 2008.

[7] E. Ngai and D. Blejer, "Mutual coupling analyses for small GPS adaptive arrays," in *Antennas and Propagation Society International Symposium, 2001. IEEE*, 2001, pp. 38-41.

[8] F. Yang and Y. Rahmat-Samii, "Microstrip antennas integrated with electromagnetic band-gap (EBG) structures: A low mutual coupling design for array applications," *Antennas and Propagation, IEEE Transactions on,* vol. 51, pp. 2936-2946, 2003.

[9] K. Sarabandi and Y. J. Song, "Subwavelength radio repeater system utilizing miniaturized antennas and metamaterial channel isolator," *Antennas and Propagation, IEEE Transactions on,* vol. 59, pp. 2683-2690, 2011.

[10] M. M. Bait-Suwailam, M. S. Boybay, and O. M. Ramahi, "Electromagnetic coupling reduction in high-profile monopole antennas using single-negative magnetic metamaterials for MIMO applications," *Antennas and Propagation, IEEE Transactions on,* vol. 58, pp. 2894-2902, 2010.

[11] S. Gupta, G. Mumcu, and P. A. Herzig, "Small coupled double loop antennas for dual band GPS arrays," in *Wireless and Microwave Technology Conference (WAMICON), 2011 IEEE 12th Annual*, 2011, pp. 1-4.

[12] A. M. Niknejad and H. Hashemi, *mm-Wave Silicon Technology*: Springer, 2008.

[13] "Available Online: http://cache.freescale.com/files/microcontrollers/doc/fact_sheet/AUTORADARFS.pdf."

[14] G. Brooker, "Millimetre Wave Radar for Tracking and Imaging applications," in *1st International Conference on Sensing technology, New Zealand*, 2005.

[15] A. Natarajan, S. K. Reynolds, T. Ming-Da, S. T. Nicolson, J. H. C. Zhan, K. Dong Gun, *et al.*, "A Fully-Integrated 16-Element Phased-Array Receiver in SiGe BiCMOS for 60-GHz Communications," *Solid-State Circuits, IEEE Journal of,* vol. 46, pp. 1059-1075, 2011.

[16] N. Ngoc Tinh, R. Sauleau, M. Ettorre, and L. Le Coq, "Focal Array Fed Dielectric Lenses: An Attractive Solution for Beam Reconfiguration at Millimeter Waves," *Antennas and Propagation, IEEE Transactions on,* vol. 59, pp. 2152-2159, 2011.

[17] J. Huang, *Reflectarray antenna*: Wiley Online Library, 2007.

[18] Y. Tiku and G. M. Rebeiz, "A22-24 GHz 4-Element CMOS Phased Array With On-Chip Coupling Characterization," *Solid-State Circuits, IEEE Journal of,* vol. 43, pp. 2134-2143, 2008.

[19] G. M. Rebeiz and K.-J. Koh, "Silicon RFICs for phased arrays," *Microwave Magazine, IEEE,* vol. 10, pp. 96-103, 2009.

[20] K. Kwang-Jin and G. M. Rebeiz, "An X- and Ku-Band 8-Element Phased-Array Receiver in 0.18-um SiGe BiCMOS Technology " *Solid-State Circuits, IEEE Journal of,* vol. 43, pp. 1360-1371, 2008.

[21] D.-W. Kang, J.-G. Kim, B.-W. Min, and G. M. Rebeiz, "Single and four-element-band transmit/receive phased-array silicon RFICs with 5-bit amplitude and phase control," *Microwave Theory and Techniques, IEEE Transactions on,* vol. 57, pp. 3534-3543, 2009.

[22] S. Raman, N. S. Barker, and G. M. Rebeiz, "A W-band dielectric-lens-based integrated monopulse radar receiver," *Microwave Theory and Techniques, IEEE Transactions on,* vol. 46, pp. 2308-2316, 1998.

[23] G. Xiang, H. Hashemi, and A. Hajimiri, "A fully integrated 24-GHz eight-element phased-array receiver in silicon," *Solid-State Circuits, IEEE Journal of,* vol. 39, pp. 2311-2320, 2004.

[24] A. Natarajan, A. Komijani, G. Xiang, A. Babakhani, and A. Hajimiri, "A 77-GHz Phased-Array Transceiver With On-Chip Antennas in Silicon: Transmitter and Local LO-Path Phase Shifting," *Solid-State Circuits, IEEE Journal of,* vol. 41, pp. 2807-2819, 2006.

[25] J. H. So, J. Thelen, A. Qusba, G. J. Hayes, G. Lazzi, and M. D. Dickey, "Reversibly deformable and mechanically tunable fluidic antennas," *Advanced Functional Materials,* vol. 19, pp. 3632-3637, 2009.

[26] L. Meng and N. Behdad, "Fluidically Tunable Frequency Selective/Phase Shifting Surfaces for High-Power Microwave Applications," *Antennas and Propagation, IEEE Transactions on,* vol. 60, pp. 2748-2759, 2012.

[27] D. F. Filipovic, S. S. Gearhart, and G. M. Rebeiz, "Double-slot antennas on extended hemispherical and elliptical silicon dielectric lenses," *Microwave Theory and Techniques, IEEE Transactions on,* vol. 41, pp. 1738-1749, 1993.

[28] G. C. Trichopoulos, G. Mumcu, K. Sertel, H. L. Mosbacker, and P. Smith, "A novel approach for improving off-axis pixel performance of terahertz focal plane arrays," *Microwave Theory and Techniques, IEEE Transactions on,* vol. 58, pp. 2014-2021, 2010.

[29] H. T. Hui, "Reducing the mutual coupling effect in adaptive nulling using a re-defined mutual impedance," *Microwave and Wireless Components Letters, IEEE,* vol. 12, pp. 178-180, 2002.

[30] S.-C. Chen, Y.-S. Wang, and S.-J. Chung, "A decoupling technique for increasing the port isolation between two strongly coupled antennas," *Antennas and Propagation, IEEE Transactions on,* vol. 56, pp. 3650-3658, 2008.

[31] A. J. Bach and H. Rasmussen, "Decoupling and Descattering Networks for Antennas," *IEEE Transactions on Antennas and Propagation,* 1976.

[32] C.-Y. Chiu, C.-H. Cheng, R. D. Murch, and C. R. Rowell, "Reduction of mutual coupling between closely-packed antenna elements," *Antennas and Propagation, IEEE Transactions on,* vol. 55, pp. 1732-1738, 2007.

[33] M. M. Bait-Suwailam, O. F. Siddiqui, and O. M. Ramahi, "Mutual coupling reduction between microstrip patch antennas using slotted-complementary split-ring resonators," *Antennas and Wireless Propagation Letters, IEEE,* vol. 9, pp. 876-878, 2010.

[34] E. Rajo-Iglesias, O. Quevedo-Teruel, and L. Inclan-Sanchez, "Mutual coupling reduction in patch antenna arrays by using a planar EBG structure and a multilayer dielectric substrate," *Antennas and Propagation, IEEE Transactions on,* vol. 56, pp. 1648-1655, 2008.

[35] K. Buell, H. Mosallaei, and K. Sarabandi, "Metamaterial insulator enabled superdirective array," *Antennas and Propagation, IEEE Transactions on,* vol. 55, pp. 1074-1085, 2007.

[36] A. Gheethan and G. Mumcu, "Coupling reduction of coupled double loop GPS antennas using split ring resonators," in *Antennas and Propagation (APSURSI), 2011 IEEE International Symposium on*, 2011, pp. 2613-2616.

[37] Y. Zhou, C.-C. Chen, and J. L. Volakis, "Single-fed circularly polarized antenna element with reduced coupling for GPS arrays," *Antennas and Propagation, IEEE Transactions on,* vol. 56, pp. 1469-1472, 2008.

[38] "Available Online: http://www.ic72.com/pdf_file/d/122906.pdf."

[39] S. Gupta and G. Mumcu, "Dual-Band Miniature Coupled Double Loop GPS Antenna Loaded With Lumped Capacitors and Inductive Pins," *Antennas and Propagation, IEEE Transactions on,* vol. 61, pp. 2904-2910, 2013.

[40] R. Marqués, F. Medina, and R. Rafii-El-Idrissi, "Role of bianisotropy in negative permeability and left-handed metamaterials," *Physical Review B,* vol. 65, p. 144440, 2002.

[41] R. Marqués, F. Mesa, J. Martel, and F. Medina, "Comparative analysis of edge-and broadside-coupled split ring resonators for metamaterial design-theory and experiments," *Antennas and Propagation, IEEE Transactions on,* vol. 51, pp. 2572-2581, 2003.

[42] S. I. Maslovski, P. M. Ikonen, I. Kolmakov, S. A. Tretyakov, and M. Kaunisto, "Artificial magnetic materials based on the new magnetic particle: Metasolenoid," *Progress In Electromagnetics Research,* vol. 54, pp. 61-81, 2005.

[43] D. Ghodgaonkar, V. Varadan, and V. Varadan, "Free-space measurement of complex permittivity and complex permeability of magnetic materials at microwave frequencies," *Instrumentation and Measurement, IEEE Transactions on,* vol. 39, pp. 387-394, 1990.

[44] K. Buell, H. Mosallaei, and K. Sarabandi, "A substrate for small patch antennas providing tunable miniaturization factors," *Microwave Theory and Techniques, IEEE Transactions on,* vol. 54, pp. 135-146, 2006.

[45] Y. Zhou, C.-C. Chen, and J. L. Volakis, "Dual band proximity-fed stacked patch antenna for tri-band GPS applications," *Antennas and Propagation, IEEE Transactions on,* vol. 55, pp. 220-223, 2007.

[46] "ADS® is a trademark of Agilent. Available online: http://www.agilent.com."

[47] D. M. Pozar, *Microwave engineering*: John Wiley & Sons, 2009.

[48] "Available Online: http://www.anaren.com."

[49] I. J. Gupta and A. A. Ksienski, "Effect of mutual coupling on the performance of adaptive arrays," *Antennas and Propagation, IEEE Transactions on,* vol. 31, pp. 785-791, 1983.

[50] E. M. Friel and K. M. Pasala, "Effects of mutual coupling on the performance of STAP antenna arrays," *Aerospace and Electronic Systems, IEEE Transactions on,* vol. 36, pp. 518-527, 2000.

[51] C.-C. Yeh, M.-L. Leou, and D. R. Ucci, "Bearing estimations with mutual coupling present," *Antennas and Propagation, IEEE Transactions on,* vol. 37, pp. 1332-1335, 1989.

[52] B. Friedlander and A. J. Weiss, "Direction finding in the presence of mutual coupling," *Antennas and Propagation, IEEE Transactions on,* vol. 39, pp. 273-284, 1991.

[53] R. S. Adve and T. K. Sarkar, "Compensation for the effects of mutual coupling on direct data domain adaptive algorithms," *IEEE Transactions on Antennas and Propagation,* vol. 48, pp. 86-94, 2000.

[54] M. Wang and Z. Shen, "Nulling of antenna arrays including the mutual coupling effect," in *Vehicular Technology Conference, 2008. VTC Spring 2008. IEEE*, 2008, pp. 247-251.

[55] G. Strang, *Linear Algebra and its Applications*, 3rd edition ed.: Thomson Learning, 1988.

[56] *[MATLAB® is a trademark of Mathworks. Available online:* http://www.mathworks.com/products/matlab/.

[57] M. Li and N. Behdad, "Fluidically tunable frequency selective/phase shifting surfaces for high-power microwave applications," *Antennas and Propagation, IEEE Transactions on,* vol. 60, pp. 2748-2759, 2012.

[58] G. Mumcu, A. Dey, and T. Palomo, "Frequency-Agile Bandpass Filters Using Liquid Metal Tunable Broadside Coupled Split Ring Resonators," *Microwave and Wireless Components Letters, IEEE,* vol. 23, pp. 187-189, 2013.

[59] D. Rodrigo, L. Jofre, and B. A. Cetiner, "Circular Beam-Steering Reconfigurable Antenna With Liquid Metal Parasitics," *Antennas and Propagation, IEEE Transactions on,* vol. 60, pp. 1796-1802, 2012.

[60] M. R. Khan, G. J. Hayes, J.-H. So, G. Lazzi, and M. D. Dickey, "A frequency shifting liquid metal antenna with pressure responsiveness," *Applied Physics Letters,* vol. 99, p. 013501, 2011.

[61] S. Jalali Mazlouman, X. J. Jiang, A. Mahanfar, C. Menon, and R. G. Vaughan, "A reconfigurable patch antenna using liquid metal embedded in a silicone substrate," *Antennas and Propagation, IEEE Transactions on,* vol. 59, pp. 4406-4412, 2011.

[62] G. J. Hayes, J.-H. So, A. Qusba, M. D. Dickey, and G. Lazzi, "Flexible liquid metal alloy (EGaIn) microstrip patch antenna," *Antennas and Propagation, IEEE Transactions on,* vol. 60, pp. 2151-2156, 2012.

[63] Y. Damgaci and B. A. Cetiner, "A frequency reconfigurable antenna based on digital microfluidics," *Lab on a Chip,* vol. 13, pp. 2883-2887, 2013.

[64] K. Kwang-Jin, J. W. May, and G. M. Rebeiz, "A Millimeter-Wave (40-45 GHz) 16-Element Phased-Array Transmitter in 0.18-um SiGe BiCMOS Technology," *Solid-State Circuits, IEEE Journal of,* vol. 44, pp. 1498-1509, 2009.

[65] A. Babakhani, D. Rutledge, and A. Hajimiri, "mm-Wave Phased Arrays in Silicon with Integrated Antennas," in *Proc. Antenna and Propagation Symposium*, 2007.

[66] A. Abbaspour-Tamijani and K. Sarabandi, "An affordable millimeter-wave beam-steerable antenna using interleaved planar subarrays," *Antennas and Propagation, IEEE Transactions on,* vol. 51, pp. 2193-2202, 2003.

[67] P. Otero, G. V. Eleftkeriades, and J. R. Mosig, "Integrated modified rectangular loop slot antenna on substrate lenses for millimeter- and submillimeter-wave frequencies mixer applications," *Antennas and Propagation, IEEE Transactions on,* vol. 46, pp. 1489-1497, 1998.

[68] G. Eleftheriades and G. Rebeiz, "Self and mutual admittance of slot antennas on a dielectric half-space," *International Journal of Infrared and Millimeter Waves,* vol. 14, pp. 1925-1946, 1993/10/01 1993.

[69] C. A. Balanis, *Antenna theory: analysis and design*: John Wiley & Sons, 2012.

[70] L. Mall, "Analysis into Proximity-Coupled Microstrip Antenna on Dielectric Lens."

[71] C. A. Balanis and J. Wiley, *Advanced engineering electromagnetics* vol. 111: Wiley Online Library, 2012.

[72] D. F. Filipovic, G. P. Gauthier, S. Raman, and G. M. Rebeiz, "Off-axis properties of silicon and quartz dielectric lens antennas," *Antennas and Propagation, IEEE Transactions on,* vol. 45, pp. 760-766, 1997.

[73] R. E. Colline, "Foundation for Microwave Engineering," ed: McGraw Hill, New York, 1992.

[74] "Available Online http://www.triquint.com/products/p/TGS4304."

[75] R. Guldiken, M. C. Jo, N. D. Gallant, U. Demirci, and J. Zhe, "Sheathless Size-Based Acoustic Particle Separation," *Sensors,* vol. 12, pp. 905-922, 2012.

[76] T. Fujii, "PDMS-based microfluidic devices for biomedical applications," *Microelectronic Engineering,* vol. 61, pp. 907-914, 2002.

[77] M. Vlachopoulou, A. Tserepi, P. Pavli, P. Argitis, M. Sanopoulou, and K. Misiakos, "A low temperature surface modification assisted method for bonding plastic substrates," *Journal of Micromechanics and Microengineering,* vol. 19, p. 015007, 2009.

[78] F. Ananasso, "20/30 GHz satellite communications: the technology is mature," in *Digital Satellite Communications, 1995., Tenth International Conference on*, 1995, pp. 152-158 vol.1.

[79] K.-C. Huang and D. J. Edwards, *Millimetre Wave Antennas for Gigabit Wireless Communications: A Practical Guide to Design and Analysis in a System Context*: John Wiley & Sons, 2008.

[80] N. Seong, C. Pyo, J. Chae, and C. Kim, "Ka-band satellite active phased array multi-beam antenna," in *Vehicular Technology Conference, 2004. VTC 2004-Spring. 2004 IEEE 59th*, 2004, pp. 2807-2810.

[81] T. Lambard, O. Lafond, M. Himdi, H. Jeuland, S. Bolioli, and L. Le Coq, "Ka-band phased array antenna for high-data-rate SATCOM," *Antennas and Wireless Propagation Letters, IEEE,* vol. 11, pp. 256-259, 2012.

[82] K. Jing-Lin, L. Yi-Fong, H. Ting-Yi, C. Yi-Long, H. Yi-Keng, P. Pen-Jui, *et al.*, "60-GHz Four-Element Phased-Array Transmit/Receive System-in-Package Using Phase Compensation Techniques in 65-nm Flip-Chip CMOS Process," *Microwave Theory and Techniques, IEEE Transactions on,* vol. 60, pp. 743-756, 2012.

[83] K. Choul-Young, K. Dong-Woo, and G. M. Rebeiz, "A 44-46-GHz 16-Element SiGe BiCMOS High-Linearity Transmit/Receive Phased Array," *Microwave Theory and Techniques, IEEE Transactions on,* vol. 60, pp. 730-742, 2012.

[84] K. Sudhakar Rao, G. A. Morin, M. Q. Tang, S. Richard, and C. Kwok Kee, "Development of a 45 GHz multiple-beam antenna for military satellite communications," *Antennas and Propagation, IEEE Transactions on,* vol. 43, pp. 1036-1047, 1995.

[85] K. S. Rao and M. Q. Tang, "Stepped-reflector antenna for dual-band multiple beam Satellite communications payloads," *Antennas and Propagation, IEEE Transactions on,* vol. 54, pp. 801-811, 2006.

[86] D. M. Pozar, S. D. Targonski, and H. D. Syrigos, "Design of millimeter wave microstrip reflectarrays," *Antennas and Propagation, IEEE Transactions on,* vol. 45, pp. 287-296, 1997.

[87] D. M. Pozar and T. A. Metzler, "Analysis of a reflectarray antenna using microstrip patches of variable size," *Electronics Letters,* vol. 29, pp. 657-658, 1993.

[88] R. E. Munson, H. A. Haddad, and J. W. Hanlen, "Microstrip reflectarray for satellite communication and radar cross-section enhancement or reduction," ed: Google Patents, 1987.

[89] M. G. Keller, J. Shaker, A. Petosa, A. Ittipiboon, M. Cuhaci, and Y. M. M. Antar, "A Ka-Band Dielectric Resonator Antenna Reflectarray," in *Microwave Conference, 2000. 30th European*, 2000, pp. 1-4.

[90] D. Berry, R. Malech, and W. Kennedy, "The reflectarray antenna," *Antennas and Propagation, IEEE Transactions on,* vol. 11, pp. 645-651, 1963.

[91] A. A. Gheethan, J. Myeong Chan, R. Guldiken, and G. Mumcu, "Microfluidic Based Ka-Band Beam-Scanning Focal Plane Array," *Antennas and Wireless Propagation Letters, IEEE,* vol. 12, pp. 1638-1641, 2013.

[92] A. Dey, R. Guldiken, and G. Mumcu, "Wideband frequency tunable liquid metal monopole antenna," in *Antennas and Propagation Society International Symposium (APSURSI), 2013 IEEE*, 2013, pp. 392-393.

[93] M. Rashed Khan, G. J. Hayes, S. Ju-Hee, G. Lazzi, and M. D. Dickey, "A frequency shifting liquid metal antenna with pressure responsiveness," *Applied Physics Letters,* vol. 99, pp. 013501-013501-3, 2011.

[94] S. Jalali Mazlouman, J. Xing Jie, A. Mahanfar, C. Menon, and R. G. Vaughan, "A Reconfigurable Patch Antenna Using Liquid Metal Embedded in a Silicone Substrate," *Antennas and Propagation, IEEE Transactions on,* vol. 59, pp. 4406-4412, 2011.

[95] C. Shi, W. Zhigang, P. Hallbjorner, K. Hjort, and A. Rydberg, "Foldable and Stretchable Liquid Metal Planar Inverted Cone Antenna," *Antennas and Propagation, IEEE Transactions on,* vol. 57, pp. 3765-3771, 2009.

[96] A. Qusba, A. K. RamRakhyani, S. Ju-Hee, G. J. Hayes, M. D. Dickey, and G. Lazzi, "On the Design of Microfluidic Implant Coil for Flexible Telemetry System," *Sensors Journal, IEEE,* vol. 14, pp. 1074-1080, 2014.

[97] G. J. Hayes, S. Ju-Hee, A. Qusba, M. D. Dickey, and G. Lazzi, "Flexible Liquid Metal Alloy (EGaIn) Microstrip Patch Antenna," *Antennas and Propagation, IEEE Transactions on,* vol. 60, pp. 2151-2156, 2012.

[98] H. D. Hristov, *Fresnal Zones in Wireless Links, Zone Plate Lenses and Antennas*: Artech House, Inc., 2000.

[99] L. Meng and N. Behdad, "Wideband True-Time-Delay Microwave Lenses Based on Metallo-Dielectric and All-Dielectric Lowpass Frequency Selective Surfaces," *Antennas and Propagation, IEEE Transactions on,* vol. 61, pp. 4109-4119, 2013.

[100] L. Meng, M. A. Al-Joumayly, and N. Behdad, "Broadband True-Time-Delay Microwave Lenses Based on Miniaturized Element Frequency Selective Surfaces," *Antennas and Propagation, IEEE Transactions on,* vol. 61, pp. 1166-1179, 2013.

[101] M. A. Al-Joumayly and N. Behdad, "Wideband Planar Microwave Lenses Using Sub-Wavelength Spatial Phase Shifters," *Antennas and Propagation, IEEE Transactions on,* vol. 59, pp. 4542-4552, 2011.

[102] "Availabe Online at http://www.rogerscorp.com/documents/606/index.aspx."

[103] "Available Online https://www.rogerscorp.com/documents/730/acm/ULTRALAM-3000-LCP-laminate-data-sheet-ULTRALAM-3850.pdf."

[104] N. J. Farcich, J. Salonen, and P. M. Asbeck, "Single-Length Method Used to Determine the Dielectric Constant of Polydimethylsiloxane," *Microwave Theory and Techniques, IEEE Transactions on,* vol. 56, pp. 2963-2971, 2008.

[105] "Available Online http://www.home.agilent.com/en/pc-1297113/advanced-design-system-ads?&cc=US&lc=eng."

[106] J. Anguera, E. Martinez, C. Puente, C. Borja, and J. Soler, "Broad-band dual-frequency microstrip patch antenna with modified Sierpinski fractal geometry," *Antennas and Propagation, IEEE Transactions on,* vol. 52, pp. 66-73, 2004.

[107] N.-C. Kuo, C.-N. Chiu, H.-C. Hsieh, and J.-S. Chen, "Radiation Minimization of Single-Stub Microstrip Impedance Transformers," 2013.

[108] "Available Online https://www.hittite.com/products/view.html/view/HMC971."

[109] G. Gonzalez, *Microwave transistor amplifiers: analysis and design* vol. 2: Prentice hall New Jersey, 1997.

[110] V. Sunkara, D.-K. Park, H. Hwang, R. Chantiwas, S. A. Soper, and Y.-K. Cho, "Simple room temperature bonding of thermoplastics and poly (dimethylsiloxane)," *Lab on a Chip,* vol. 11, pp. 962-965, 2011.

[111] "Available Online http://www.micro-components.com."

[112] M. Bahrami, M. M. Yovanovich, and J. R. Culham, "Pressure Drop of Fully-Developed, Laminar Flow in Microchannels of Arbitrary Cross-Section," *Journal of Fluids Engineering,* vol. 128, pp. 1036-1044, 2006.

[113] "Available Online www.SimplyPumps.com."

APPENDICES

Appendix A: Copyright Notice for Chapter 2

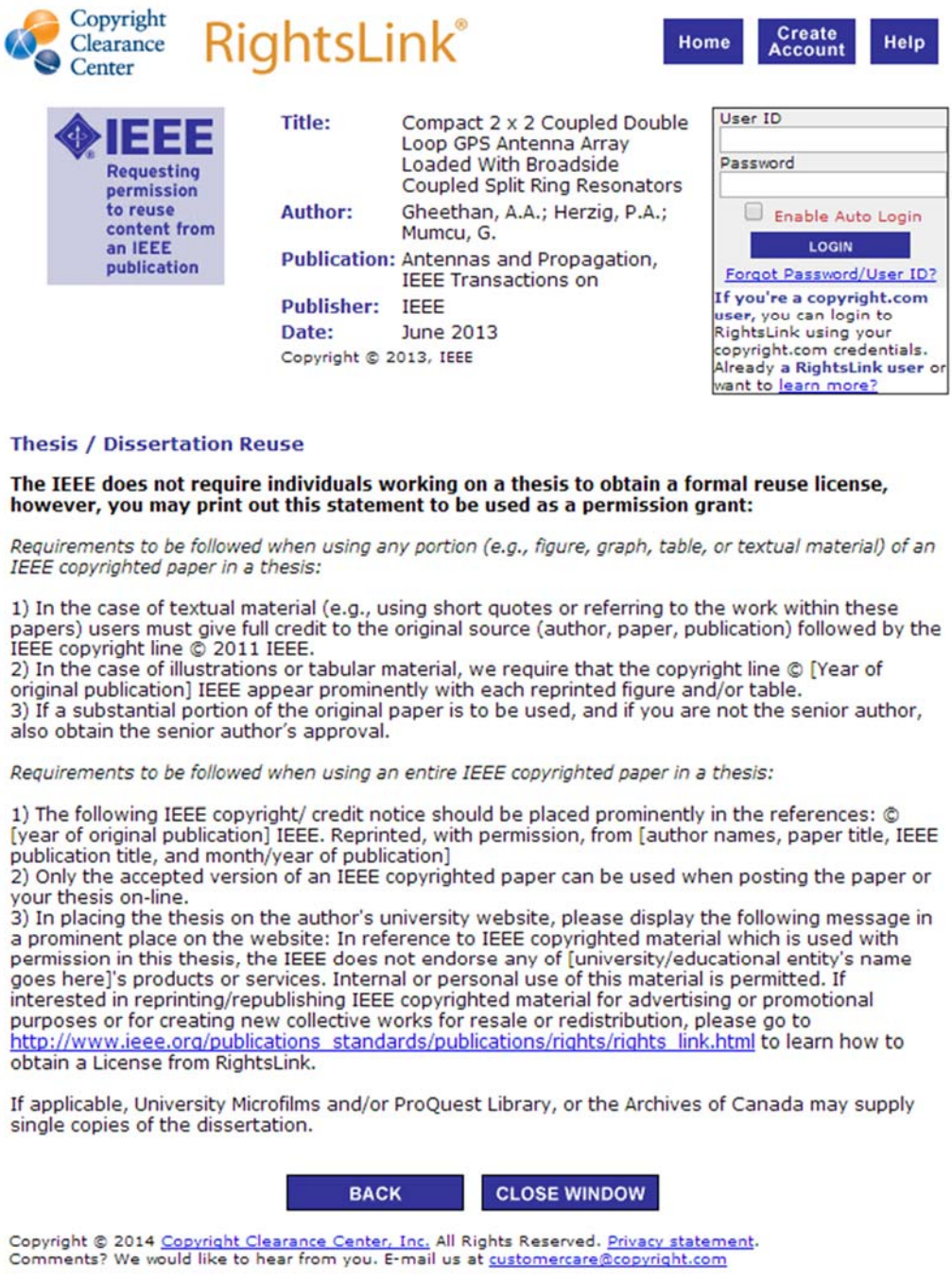

Copyright Clearance Center RightsLink®

Home | Create Account | Help

IEEE Requesting permission to reuse content from an IEEE publication

Title: Compact 2 x 2 Coupled Double Loop GPS Antenna Array Loaded With Broadside Coupled Split Ring Resonators
Author: Gheethan, A.A.; Herzig, P.A.; Mumcu, G.
Publication: Antennas and Propagation, IEEE Transactions on
Publisher: IEEE
Date: June 2013
Copyright © 2013, IEEE

User ID
Password
Enable Auto Login
LOGIN
Forgot Password/User ID?
If you're a copyright.com user, you can login to RightsLink using your copyright.com credentials. Already a RightsLink user or want to learn more?

Thesis / Dissertation Reuse

The IEEE does not require individuals working on a thesis to obtain a formal reuse license, however, you may print out this statement to be used as a permission grant:

Requirements to be followed when using any portion (e.g., figure, graph, table, or textual material) of an IEEE copyrighted paper in a thesis:

1) In the case of textual material (e.g., using short quotes or referring to the work within these papers) users must give full credit to the original source (author, paper, publication) followed by the IEEE copyright line © 2011 IEEE.
2) In the case of illustrations or tabular material, we require that the copyright line © [Year of original publication] IEEE appear prominently with each reprinted figure and/or table.
3) If a substantial portion of the original paper is to be used, and if you are not the senior author, also obtain the senior author's approval.

Requirements to be followed when using an entire IEEE copyrighted paper in a thesis:

1) The following IEEE copyright/ credit notice should be placed prominently in the references: © [year of original publication] IEEE. Reprinted, with permission, from [author names, paper title, IEEE publication title, and month/year of publication]
2) Only the accepted version of an IEEE copyrighted paper can be used when posting the paper or your thesis on-line.
3) In placing the thesis on the author's university website, please display the following message in a prominent place on the website: In reference to IEEE copyrighted material which is used with permission in this thesis, the IEEE does not endorse any of [university/educational entity's name goes here]'s products or services. Internal or personal use of this material is permitted. If interested in reprinting/republishing IEEE copyrighted material for advertising or promotional purposes or for creating new collective works for resale or redistribution, please go to http://www.ieee.org/publications_standards/publications/rights/rights_link.html to learn how to obtain a License from RightsLink.

If applicable, University Microfilms and/or ProQuest Library, or the Archives of Canada may supply single copies of the dissertation.

BACK | CLOSE WINDOW

Appendix B: Copyright Notice for Chapter 3

Thesis / Dissertation Reuse

The IEEE does not require individuals working on a thesis to obtain a formal reuse license, however, you may print out this statement to be used as a permission grant:

Requirements to be followed when using any portion (e.g., figure, graph, table, or textual material) of an IEEE copyrighted paper in a thesis:

1) In the case of textual material (e.g., using short quotes or referring to the work within these papers) users must give full credit to the original source (author, paper, publication) followed by the IEEE copyright line © 2011 IEEE.
2) In the case of illustrations or tabular material, we require that the copyright line © [Year of original publication] IEEE appear prominently with each reprinted figure and/or table.
3) If a substantial portion of the original paper is to be used, and if you are not the senior author, also obtain the senior author's approval.

Requirements to be followed when using an entire IEEE copyrighted paper in a thesis:

1) The following IEEE copyright/ credit notice should be placed prominently in the references: © [year of original publication] IEEE. Reprinted, with permission, from [author names, paper title, IEEE publication title, and month/year of publication]
2) Only the accepted version of an IEEE copyrighted paper can be used when posting the paper or your thesis on-line.
3) In placing the thesis on the author's university website, please display the following message in a prominent place on the website: In reference to IEEE copyrighted material which is used with permission in this thesis, the IEEE does not endorse any of [university/educational entity's name goes here]'s products or services. Internal or personal use of this material is permitted. If interested in reprinting/republishing IEEE copyrighted material for advertising or promotional purposes or for creating new collective works for resale or redistribution, please go to http://www.ieee.org/publications_standards/publications/rights/rights_link.html to learn how to obtain a License from RightsLink.

If applicable, University Microfilms and/or ProQuest Library, or the Archives of Canada may supply single copies of the dissertation.

BACK CLOSE WINDOW

ABOUT THE AUTHOR

Ahmad Gheethan received the B.Sc. degree from Jordan University of Science and Technology (JUST), Jordan, and the M.Sc. degree from South Dakota School of Mines and Technology (SDSM&T), Rapid City, SD, in 2007 and 2009, respectively, all in electrical engineering. In 2010, he joined the center for wireless and microwave Information (WAMI) at the University of South Florida, Tampa, FL, as a graduate research assistant. He was at Motorola Solutions in Summer/2012 as an RF/wireless engineer intern where he worked on designing a reconfigurable antenna system for the LTE applications. His current research is focused on the metamaterials and their applications to antenna arrays, microfluidic based antenna arrays and beam scanning antenna arrays. Mr. Gheethan was the recipient of the Student Paper Award (Honorable Mention) at the 2009 and 2014 IEEE APS International Symposiums, IEEE APS Research Doctoral Award, and the 1st place in the Texas Instruments sensing design challenge.